

Electronic Thesis and Dissertation Repository

12-15-2016 12:00 AM

In Mold Flow of Long Fibers in Compression Molding Process

Gleb Meirson, *The University of Western Ontario*

Supervisor: Dr. Andrew Hrymak, *The University of Western Ontario*

A thesis submitted in partial fulfillment of the requirements for the Doctor of Philosophy degree
in Chemical and Biochemical Engineering

© Gleb Meirson 2016

Follow this and additional works at: <https://ir.lib.uwo.ca/etd>



Part of the [Polymer Science Commons](#), and the [Structural Materials Commons](#)

Recommended Citation

Meirson, Gleb, "In Mold Flow of Long Fibers in Compression Molding Process" (2016). *Electronic Thesis and Dissertation Repository*. 4377.

<https://ir.lib.uwo.ca/etd/4377>

This Dissertation/Thesis is brought to you for free and open access by Scholarship@Western. It has been accepted for inclusion in Electronic Thesis and Dissertation Repository by an authorized administrator of Scholarship@Western. For more information, please contact wlsadmin@uwo.ca.

Abstract

Long Fiber Thermoplastics (LFT) are promising new materials with high physical properties and low density. These high properties are obtained by embedding very long fibers (~ 100 mm) into a thermoplastic matrix. Such a high fiber length dictates the use of a compression molding process for manufacturing as the length of discontinuous fibers in injection molding is limited by pellet length.

LFT composites are of great interest for the automotive industry. These materials are already used in some interior and exterior car parts such as bumpers, seat structures, door module etc. This research is inspired by the desire to manufacture load carrying parts for vehicles such as wheel rims which would dramatically reduce vehicle weight and subsequently save fuel. This, however, requires a much better understanding of long fiber orientation and distribution during compression molding.

Current orientation models were developed for short fibers ($< 1mm$). Initially these models were extended to cases that were considered long fibers (several millimetres). Recently these models are being extended even for the LFT-D case fibers which can reach up to 80 mm. Since several of the governing assumptions for short fiber models are not suitable for long fibers, the models can not provide accurate results for long fibers. Due to this limitation long fibers require independent treatments.

This thesis presents a new model which is specifically designed for long flexible fibers. This model is confirmed by comparing results obtained for simple shear flow to results found in the literature. The model was implemented in a rheometric squeeze flow, which is defined as flow between two approaching to each other parallel plates, and provided results previously not seen in the literature. Interactions were implemented into the model and tested for rheometric squeeze flow and simple shear flow cases. In addition to providing insight into fiber orientation and deformation in rheometric squeeze flow, which was not previously studied in the literature, the proposed model shows more predictive results than previously found in the literature.

Keywords: Long fibers, Composite materials, Automotive industry, Fiber orientation, Compression molding, Injection molding.

Acknowledgements

I would like to thank Ontario Trillium Scholarship, Ontario Research Fund and General Motors Canada for funding this project.

I express my sincere gratitude to my supervisor Dr. Andrew Hrymak, for his constant guidance and encouragement. During the past four and a half years he became my supervisor, mentor and friend. I would also like to thank my committee members Dr. David Jeffrey and Dr. Ajay Ray for their time and advice.

I am very grateful for the support of CBE administrative staff, my group mates, office mates and my friends on the department and especially my dear friend Stanislav Ivanov for their support.

I would like to acknowledge the Western SHARCNET team and especially Ge Baolai for helping me to run my simulations on their system.

Last but not least, I would like to thank my amazing family. My parents who sacrificed their desires so that their children could have a better life, my brother whom I can always count for a wise advice and my beautiful wife who was always there for me in the past four and a half years, supported me and helped me when I needed it the most.

Without you all this thesis would not be possible, my sincere thanks to you all. You will forever be in my heart.

Contents

Abstract	i
Acknowledgements	ii
List of Figures	vi
List of Tables	xi
List of Appendices	xii
1 Introduction	1
1.1 Composites History	1
1.2 Long Fiber Thermoplastic Composites	1
1.3 Orientation Models	4
1.3.1 Single Short Rigid Fiber	4
1.3.2 Short Rigid Fiber Suspensions	9
1.4 Flexible Fibers	15
1.4.1 Orientation Models - Flexible Fiber	15
1.5 Interactions	16
1.5.1 Interaction Between Spheres	17
1.5.2 Interactions Between Fibers	18
1.6 Rheology	19
1.6.1 Homogeneous Systems	19
1.6.2 Fiber Filled Systems	21
1.7 Squeeze Flow	22
1.8 Objectives	25

2	Long Fiber Model Development	26
2.1	General Approach	26
2.2	Rigid Cylinder	27
2.2.1	Infinite Axis Ratio Cylinder	27
2.2.2	Finite Axis Ratio Cylinder	32
2.3	Flexible Fiber	35
2.3.1	Elongation	36
2.3.2	Bending	38
2.4	Interactions	43
2.5	Tolerance	44
2.6	Summary	46
3	Simple Shear	48
3.1	Rotational Friction Coefficients	48
3.2	Rigid Cylinder	50
3.3	Flexible Fiber	53
3.4	Calculation time	58
4	Squeeze Flow	60
4.1	Rigid Fiber	64
4.2	Flexible Fiber	67
	System A	67
	System B	77
5	Interactions	85
5.1	Rigid Cylinders	85
5.2	Flexible Fibers	89
5.2.1	Simple Shear Flow	89
5.2.2	Squeeze Flow	89
6	Conclusions	94
6.1	Simple Shear Flow	94

6.2 Rheometric Squeeze Flow	95
6.3 Interactions	95
6.4 Future Work	96
Bibliography	98
A Squeeze Flow Fiber Orientation	111
Curriculum Vitae	117

List of Figures

1.1	LFT-D brick.	2
1.2	Fibers after a burn test from LFT-D charge.	2
1.3	Composite properties as a function of fiber length [5-7].	3
1.4	Representation of fiber on axes	5
1.5	Graphical θ representation.	6
1.6	Ellipsoid's reaction to simple shear flow with shear rate $\dot{\gamma} = 4s^{-1}$. Upper case is for ellipsoid of infinite axis ratio and the bottom case is for axis ratio of 5.	7
1.7	Two dimensional orientation tensor representation.	11
1.8	Different groups of fiber deformations in simple shear flow [63]; a)axial spin, b)flexible spin, c)springy rotation, d)snake turn, e)S-turn.	14
1.9	Lubrication forces.	18
1.10	Squeeze flow system.	24
2.1	Graphic model representation;a) Cylinder is represented through projections divided into spheres for hydrodynamic torque and force calculation. b) Cylinder is represented through a collection of spheres for interactions calculations.	27
2.2	Comparison between Jeffery's model and current model for the case of constant friction coefficient in interval $[\pi/2,0]$	30
2.3	Superposition of forces on the cylinder.	32
2.4	a. Representation of a cylinder through a collection of spheres on the cylinder projections. b. Representation of cylinder's cross section with two spheres.	33

2.5	Cross section projections change during orientation.	34
2.6	Schematic representation of rigid segments connected through elastic springs.	36
2.7	Elongation diagram.	37
2.8	Bending diagram.	39
2.9	Schematic representation of bending torque with imaginary force F_{bp}	40
2.10	Schematic representation of elastic collision force.	44
2.11	Cycle times of rigid fiber of axis ratio of 40 solved for two different tolerances.	45
3.1	Comparison between simulation and Jeffery's model solution for the following conditions: $\frac{l}{d} = \infty, \dot{\gamma} = 4\frac{1}{s}, l = 0.001$	50
3.2	Comparison between simulation and Jeffery's model solution for the following conditions: $\frac{l}{d} = 5$ (4.3 equivalent), $\dot{\gamma} = 4\frac{1}{s}, l = 0.001m$	51
3.3	Friction coefficients as a function of shear rate.	51
3.4	Comparison between simulation and experimental [34] periods of rotation of a rigid fiber as a function of aspect ratio.	52
3.5	Flexible fiber transition states through rotation in a simple shear flow $\dot{\gamma} = 4\frac{1}{s}$. The flow is from left to right.	54
3.6	Graphical representation of bending parameter.	55
3.7	$\Delta\theta$ calculations for the $E = 10^9 Pa$ case from Figure 3.5.	55
3.8	$\Delta\theta$ calculations for the $E = 10^{10} Pa$ case from Figure 3.5.	56
3.9	Comparison between theoretical [31] and simulated values for critical Young modulus values for buckling.	57
3.10	12 mm fiber made out of rigid parts with axis ratio of 4,5 and 6 with Young's modulus of $10^8 Pa$ at shear rate of $4s^{-1}$	57
3.11	12 mm fiber made out of rigid parts with axis ratio of 4,5 and 6 with Young's modulus of $10^9 Pa$ at shear rate of $4s^{-1}$	58
4.1	Upper plate velocity as a function of time.	62
4.2	Upper plate location as a function of time.	63
4.3	Solution of a squeeze flow system (for system A).	63

4.4	Solution of Jeffery’s model for a fiber of different axis ratio, λ , under squeeze flow. Fiber initial coordinates are $(x_o, y_o) = (0.8, 0.8)$	65
4.5	Solution of Jeffery’s model for a fiber at different initial coordinates for $\lambda = 1$	65
4.6	Comparison between simulation and Jeffery’s model solution for: $\frac{l}{d} = \infty$, $l = 1mm$	66
4.7	Comparison between simulation and Jeffery’s model solution for: $\frac{l}{d} = 5$, $l = 1mm$	66
4.8	Path of fiber’s center mass from Figures 4.9-4.20.	68
4.9	Fiber orientation and deformation in squeeze flow for three values of Young’s modulus $A.10^9Pa, B.10^8Pa$ and $C.10^7Pa$ for fiber placed at the initial position of $(x/c, y/a_0) = (0.8, 0.8)$ using coordinates of Figure 1.10. The fiber is presented at times: 0, 2.37, 5.54, 8.13 and 8.8 s.	69
4.10	Fiber orientation and deformation in squeeze flow for three values of Young’s modulus $A.10^9Pa, B.10^8Pa$ and $C.10^7Pa$ for fiber placed at the initial position of $(x/c, y/a_0) = (0.8, 0.4)$ using coordinates of Figure 1.10. The fiber is presented at times: 0, 2.37, 5.54, 8.13 and 8.8 s.	70
4.11	Shear rate in system A at time $t = 0$	72
4.12	Shear rate in system A at time $t = 5$	73
4.13	Shear rate in system A at time $t = 9$	73
4.14	Fiber orientation and deformation in squeeze flow for three values of Young’s modulus $A.10^9Pa, B.10^8Pa$ and $C.10^7Pa$ for fiber placed at the initial position of $(x/c, y/a_0) = (0.8, 0)$ using coordinates of Figure 1.10. The fiber is presented at times: 0, 2.37, 5.54, 8.13 and 8.8 s.	74
4.15	Fiber orientation and deformation in squeeze flow for three values of Young’s modulus $A.10^9Pa, B.10^8Pa$ and $C.10^7Pa$ for fiber that was placed at the initial position of $(x/c, y/a_0) = (0.8, 0.003)$ using coordinates of Figure 1.10. The fiber is presented at times: 0, 2.37, 5.54, 8.13 and 8.8 s. . .	75

4.16	Fiber orientation and deformation in squeeze flow for Young's modulus of $10^7 Pa$. The fiber is placed with center mass at $(x/c, y/a_0) = (0.8, 0.8)$ at three different initial orientations: $A. -0.2\pi, B. -0.3\pi, C. -0.4\pi$. The fiber is presented at times: 0, 2.37, 5.54, 8.13, 8.8 and 9.2 s.	76
4.17	Fiber orientation and deformation in squeeze flow for three values of Young's modulus $A.10^9 Pa, B.10^8 Pa$ and $C.10^7 Pa$ for fiber placed at the initial position of $(x/c, y/a_0) = (0.8, 0.8)$. The fiber is presented at times: 0, 2.37, 5.54, 8.13 and 8.8 s.	78
4.18	Fiber orientation and deformation in squeeze flow for three values of Young's modulus $A.10^9 Pa, B.10^8 Pa$ and $C.10^7 Pa$ for fiber placed at the initial position of $(x/c, y/a_0) = (0.8, 0.4)$. The fiber is presented at times: 0, 2.37, 5.54, 8.13 and 8.8 s.	79
4.19	Fiber orientation and deformation in squeeze flow for three values of Young's modulus $A.10^9 Pa, B.10^8 Pa$ and $C.10^7 Pa$ for fiber placed at the initial position of $(x/c, y/a_0) = (0.8, 0)$. The fiber is presented at times: 0, 2.37, 5.54, 8.13 and 8.8 s.	81
4.20	Fiber orientation and deformation in squeeze flow for three values of Young's modulus $A.10^9 Pa, B.10^8 Pa$ and $C.10^7 Pa$ for fiber placed at the initial position of $(x/c, y/a_0) = (0.8, 0.03)$. The fiber is presented at times: 0, 2.37, 5.54, 8.13 and 8.8 s.	82
4.21	Fiber orientation and deformation in squeeze flow for three Young's modulus $10^7 Pa$ placed at initial position $(x/c, y/a) = (0.8, 0.8)$ in system A, with flow parameter $R = 0.1$. The fiber is shown at time: 0, 1.13, 2.75, 4.07, 4.34 s.	83
5.1	Interactions between rigid cylinders at shear rate of $\dot{\gamma} = 4\frac{1}{s}$	87
5.2	Normalised rotation time with dependence to ratio of length of cylinders to initial distance between cylinders centers of mass.	88
5.3	Interactions between $8mm$ flexible fibers placed in initial distance of $4mm$ in a simple shear flow ($4s^{-1}$) at viscosity of $1000 Pa \cdot s$	90

5.4	Interactions between two flexible fibers in squeeze flow where the fibers start perpendicular position to each other.	92
5.5	Interactions between two flexible fibers in squeeze flow where the fibers start at an angle of $5/6\pi$ angle to each other.	93
A.1	Rheology results of petroleum jelly at $22^{\circ}C$	112
A.2	Fiber Young's modulus measurement.	112
A.3	Visualization experiment, resulting fiber shape at 3.3s.	114
A.4	Long flexible fiber simulation in power law fluid, experimental viscosity. .	115
A.5	Long flexible fiber simulation in power law fluid, literature viscosity. . .	116

List of Tables

2.1	Physical properties in the system	47
2.2	Calculated properties in the system	47
2.3	Model parameters in the system	47
3.1	Friction coefficient parameters for several cylinder dimensions.	50
3.2	Number of simulation steps and simulation time for various fibers simulations (initial position of fiber's center of mass was at $[0.8, 0.8]$	59
4.1	System's A and B parameters.	61

List of Appendices

Appendix A Squeeze Flow Fiber Orientation	111
---	-----

Chapter 1

Introduction

1.1 Composites History

A composite is defined as a: *"thing made up of several parts or elements"* [1]. The reason behind creating composites is making a material whose combined physical properties are superior to the physical properties of its components.

Composites were known to mankind for thousands of years. The first recorded case of composite use was around 3200 B.C. in Mesopotamia when they combined wood stripes at different angles to create a material with better properties. Structures found in Egypt and Mesopotamia dated 1500 B.C were built of mud bricks, which contained straw for reinforcement [2].

Using composites presents a great opportunity to reduce structure weight while at the same time not compromising reliability. For example, plastic reinforced by 50% volume of high modulus continuous graphite fibers has five times greater modulus of elasticity and tensile strength per weight than steel [3].

1.2 Long Fiber Thermoplastic Composites

Thermoplastic composites saw a great increase in production in the 1960s, due to the development of carbon fibers, which significantly increased the stiffness of the composite compared to traditionally used glass fibers [4]. Later it was found that an increase in fiber

length provides enhanced properties to the resulting compound [5–10]. That discovery opened the door for a new process: Long Fiber Thermoplastic (LFT).

LFT process was commercialized in the mid to late 90s [11]. The fibers were embedded into the polymer, which was then cut to produce pellets of needed length. These pellets were then injected or compressed into a mold. As a result, the fibers embedded in the final product were longer than previous composites produced, but still relatively short



Figure 1.1: LFT-D brick.



Figure 1.2: Fibers after a burn test from LFT-D charge.

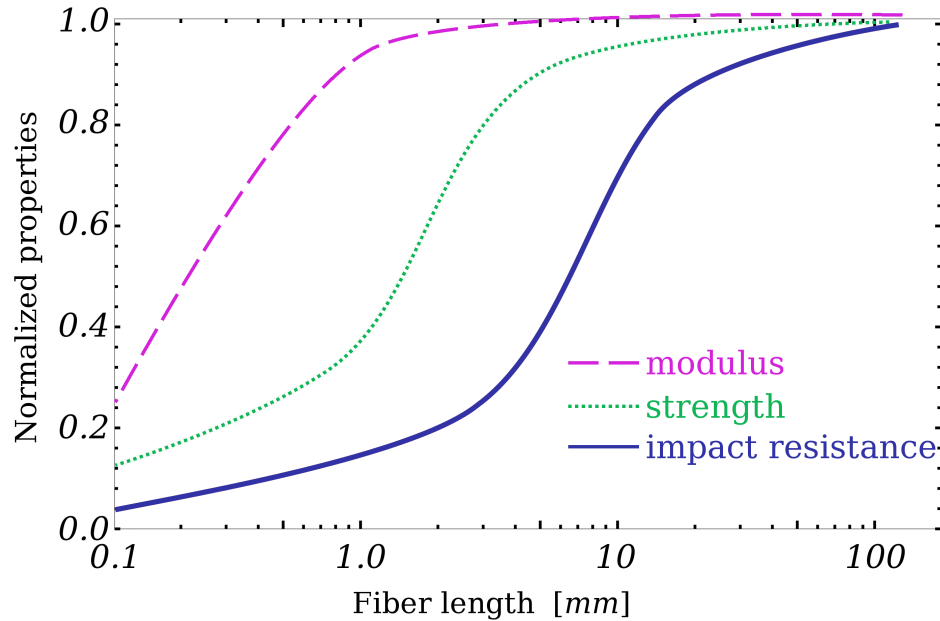


Figure 1.3: Composite properties as a function of fiber length [5-7].

due to limitations on the pellet size. Fibers longer than 1 mm are considered long [12] by injection molding standards. Recently a new process Long Fiber Thermoplastic-Direct (LFT-D) started to gain momentum. LFT-D process consists of two continuously operated twin screw extruders and a press. The first extruder mixes the polymer with additives (antioxidants, color etc.) and feeds the melt into the second extruder, which pulls and mixes continuous fibers, that may be broken during the mixing process, with the melt. The second extruder has a rectangular die which produces a brick shaped compound (Figure 1.1) of polymer and long fibers (up to 80 mm) as seen in Figure 1.2. The sample was obtained by a burn test which was made by burning part of the brick thus removing the polymeric matrix and exposing the fibers. This brick is then placed into a press and pressed into the final product. The main advantages of this new process are due to improved composite properties by increasing the fiber length, and improving manufacturing logistics [13]. The improvement in composite properties versus fiber length could be observed in Figure 1.3. Fiber orientation is a highly influential factor on composite properties. Composites are particularly strong in the direction in which the fibers are aligned. It has also been found that increasing waviness of fibers in the composite reduces its Young's modulus [14]. Thus bending and flexing of a fiber could

affect both the material micro-structure and properties [15]. Hence it is highly important to study the dynamics of fiber orientation in composite manufacturing process. Current fiber orientation models which will be described in the next sections of this chapter are designed for short fibers and hence can not accurately predict long fiber orientation. Due to that it is required to develop a new model which is specifically designed for long fibers.

1.3 Orientation Models

1.3.1 Single Short Rigid Fiber

Jeffery [16] analytically solved the equations of motion for short ellipsoid particle in low Reynolds number flow, thus predicting its orientation under the influence of a flow field [16], and predicts an ellipsoid's response to Stokes drag [17]. Jeffery's model is limited by a number of assumptions [16]:

- i. The particle is of ellipsoid shape.
- ii. The flow is considered non-inertial, which implies a low Reynolds (Re) number ($Re \ll 1$).
- iii. Particle dimensions are small compared to dimensions of the system.
- iv. The center mass of the fiber is at rest with respect to the flow, i.e. the particle is moving with the velocity of the flow.
- v. The particle is rigid.
- vi. The model is developed for a particle placed in a Newtonian fluid.

Jeffery [16] derived his model for a general flow, then simplified it for a simple shear flow case, and obtained the following equation for a three dimensional ellipsoid under the influence of a simple shear flow:

$$\frac{d\varphi}{dt} = \frac{\dot{\gamma}}{(A.R^2 + 1)} (A.R^2 \cos^2 \varphi + \sin^2 \varphi),$$

(1.1)

$$\frac{d\beta}{dt} = \frac{\dot{\gamma}(A.R^2 - 1)}{4(A.R^2 + 1)} \sin(2\beta) \sin(2\varphi), \quad (1.2)$$

where β and φ (Figure 1.4) are angles between the ellipsoid and the axes (as shown in Figure 1.4), $A.R$ is the axis ratio defined as length divided by diameter, $\dot{\gamma}$ is the local shear rate which in a simple shear flow could be defined as a derivative of velocity in the direction in which the velocity is changing. It could be seen that for the case where the axis ratio is equal to infinity, meaning the ellipsoid is infinitely long or infinitely thin, the ellipsoid will orient itself with the flow while for the case of a finite axis ratio, the ellipsoid will rotate. For the case of a simple shear flow (eqs. (1.1)-(1.2)) Jeffery's model could be analytically solved and the solution for angles (β, φ) and period of rotation T are presented in eqs.(1.3)-(1.5) [16]:

$$\tan(\varphi) = A.R \cdot \tan\left(\frac{2\pi t}{T}\right) \quad (1.3)$$

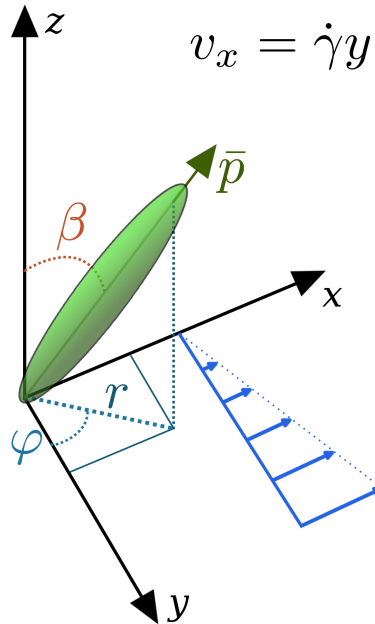


Figure 1.4: Representation of fiber on axes

$$\tan(\beta) = \frac{C \cdot A.R}{(A.R^2 \cos^2(\varphi) + \sin^2(\varphi))^{0.5}} \quad (1.4)$$

$$T = \left(\frac{2\pi}{\dot{\gamma}} \right) \left(A.R + \frac{1}{A.R} \right) \quad (1.5)$$

Sometimes it is enough to solve the two dimensional case; for example, a simple shear case where the ellipsoid is lying in the $x - y$ plane (essentially 2-D case). For these simplified cases, Jeffery's model in its general form could be presented through eq. (1.6) [18]:

$$\begin{aligned} \frac{d\theta}{dt} = & \left(\frac{A.R^2}{A.R^2 + 1} \right) \left(-\sin(\theta) \cos(\theta) \frac{\partial v_x}{\partial x} - \sin^2(\theta) \frac{\partial v_x}{\partial y} + \cos^2(\theta) \frac{\partial v_y}{\partial x} + \sin(\theta) \cos(\theta) \frac{\partial v_y}{\partial y} \right) \\ & - \left(\frac{1}{A.R^2 + 1} \right) \left(-\sin(\theta) \cos(\theta) \frac{\partial v_x}{\partial x} + \cos^2(\theta) \frac{\partial v_x}{\partial y} - \sin^2(\theta) \frac{\partial v_y}{\partial x} + \sin(\theta) \cos(\theta) \frac{\partial v_y}{\partial y} \right) \end{aligned} \quad (1.6)$$

Angle θ is represented in Figure 1.5 and the solutions of this equation for ellipsoids with axis ratio of infinity and five (5) placed in a simple shear flow field with shear rate of $4s^{-1}$ are presented in Figure 1.6 in both cases ellipsoid is initially oriented in the y direction:

In the mid-80s an orientation vector form of Jeffery's model started to appear in the scientific literature [19, 20].

Three dimensional ellipsoidal particle orientation could be described through the orientation vector $p = [p_x, p_y, p_z]$ (shown in Figure 1.4). The general vector form of Jeffery's

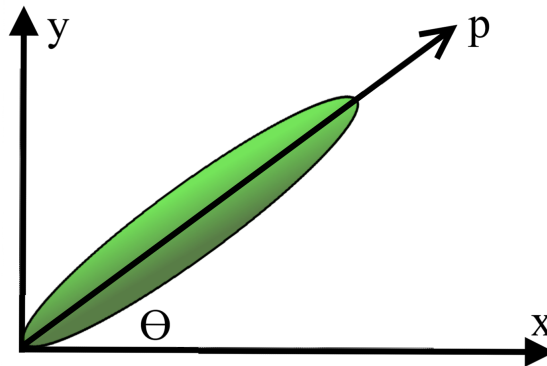


Figure 1.5: Graphical θ representation.

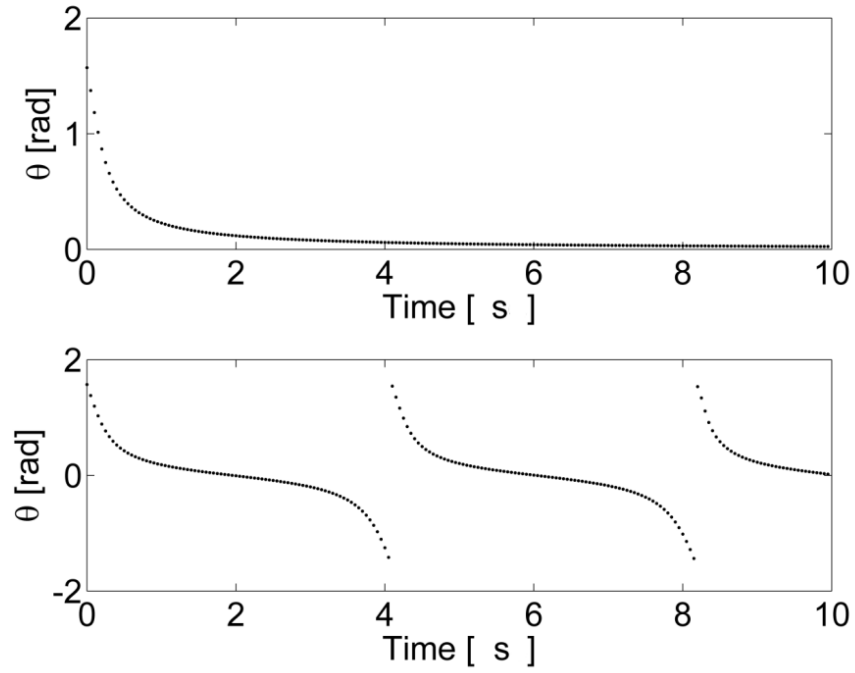


Figure 1.6: Ellipsoid's reaction to simple shear flow with shear rate $\dot{\gamma} = 4s^{-1}$. Upper case is for ellipsoid of infinite axis ratio and the bottom case is for axis ratio of 5.

model could be expressed through eq. (1.7) [21]:

$$\frac{dp}{dt} = \sigma \cdot p + \lambda (D \cdot p - (p^T \cdot D \cdot p) p), \quad (1.7)$$

where σ is a vorticity tensor, D is the deformation tensor and λ is a function of axis ratio $A.R.$

$$\sigma = 0.5 (L - L^T) \quad (1.8)$$

$$D = 0.5 (L + L^T) \quad (1.9)$$

$$L = \begin{pmatrix} \frac{dv_x}{dx} & \frac{dv_y}{dx} & \frac{dv_z}{dx} \\ \frac{dv_x}{dy} & \frac{dv_y}{dy} & \frac{dv_z}{dy} \\ \frac{dv_x}{dz} & \frac{dv_y}{dz} & \frac{dv_z}{dz} \end{pmatrix} \quad (1.10)$$

$$\lambda = \frac{A.R^2 - 1}{A.R^2 + 1} \quad (1.11)$$

Multiple experimental works confirmed Jeffery's results [22–27]. It was found that Jeffery's model could be applied not only for ellipsoids, but also to cylinders, as long as equivalent axis ratio $A.R_e$ is used to describe the geometry of the cylinder. Equivalent axis ratio of a cylinder $A.R_e$ is smaller than its real axis ratio $A.R$ and it is essentially the axis ratio of a corresponding ellipsoid that will exhibit the same response to a flow field as the cylinder with the corresponding axis ratio $A.R$. Thus Jeffery's model could be used to simulate rod-like fiber behaviour under the influence of a flow field [23,24,28–30]. Experimental data for these measurements is found in several works [23,25,31–34]. Cox [35] developed an analytical expression for forces acting on a slender body by the fluid and compared the results for a cylinder and ellipsoid.

$$F_1 = \frac{2\pi\mu lU}{\ln(2l/d) + O_I}, \quad (1.12)$$

$$O_I = \frac{-1}{2} + \frac{1}{4} \int_{-1}^{+1} \ln \left(\frac{1-s^2}{\Lambda^2} \right) ds, \quad (1.13)$$

where μ is viscosity of the fluid, l is particle's length, d is particle's diameter, U is fluid velocity, s is dimensionless distance between the center and the ends of the particle and Λ is a dimensionless function of cross-sectional radius of an arbitrary geometric at any point along its major axis. Thus for a cylinder, $\Lambda = 1$, while for an ellipsoid $\Lambda = (1-s^2)^{0.5}$ where s is a dimensionless coordinate on the major axis defined as $-1 < s < 1$. For a cylinder, $O_I = -1.5 + \ln 2$ while for the ellipsoid $O_I = -0.5$.

Cox [36] noticed that for the ratio of cases of $\theta = \frac{\pi}{2}$ and $\theta = 0$, the expression (1.14) for equivalent axis ratio will be generated:

$$\frac{\omega_{\theta=0}}{\omega_{\theta=\pi/2}} = A.R_e^2, \quad (1.14)$$

where $\omega_{\theta=0}$ is radial velocity of rod in a position of $\theta = 0$ and $\omega_{\theta=\pi/2}$ is radial velocity of rod in a position of $\theta = \frac{\pi}{2}$, for the case of an ellipsoid $A.R_e = A.R$.

Hence by measuring the radial velocity of a cylinder at a vertical and horizontal position, one could calculate its equivalent axis ratio. Since it is not very convenient to look at

radial velocity, Cox took it one step further and assumed that since radial velocity is proportional to torque it could be said that:

$$A.R_e = \sqrt{\frac{\omega_{\theta=0}}{\omega_{\theta=\pi/2}}} = \sqrt{\frac{P_{\theta=0}}{P_{\theta=\pi/2}}} \quad (1.15)$$

where $P_{\theta=0}$ is torque acting on a rod oriented in the direction of $\theta = 0$ and $P_{\theta=\pi/2}$ is the torque acting on a rod oriented in the direction of $\theta = \frac{\pi}{2}$. Cox then uses the derivation of forces acting on a slender body [35] to calculate $P_{\theta=0}$ and derives the expression of $P_{\theta=\pi/2}$ [36]. By dividing these two expressions, Cox [36] found an expression for equivalent axis ratio:

$$\frac{A.R_e}{A.R} = \left(\frac{8\pi}{3L}\right)^{0.5} \ln(A.R)^{-0.5}, \quad (1.16)$$

where L is a constant fitted to be 5.45 from the experimental data of cylinder axis ratio compared to equivalent axis ratio [25].

Harris and Pittman [37] fitted a model to match the experimental results. Eq. (1.17) provides a good fit in the range of $50 < A.R < 450$ (error is within $\pm 5\%$)

$$A.R_e = 1.14A.R^{0.844} \quad (1.17)$$

Zhang et. al. [38] developed a finite element method (FEM) to simulate the movement of a single fiber in a general flow field and compared it to Jeffery's model solution as well as computationally finding equivalent axis ratio for several axis ratio cylinders.

Although Jeffery's model was developed in 1922 and has many limiting assumptions it is still widely used [21, 39, 40]

1.3.2 Short Rigid Fiber Suspensions

Rod like fiber suspension behaviour and properties are highly dependent on fiber concentration and was widely investigated [41–44]. It is common to divide the volume fraction, c , into regions of dilute, semi concentrated and concentrated based on rod geometry:

- i. Dilute: $c < \left(\frac{d}{l}\right)^2$ -the distance between two neighboring fibers is greater than l .

- ii. Semi-concentrated: $(\frac{d}{l})^2 < c < \frac{d}{l}$ -the distance between the neighboring fibers is less than l but greater than d .
- iii. Concentrated: $\frac{d}{l} < c$ -the distance between the neighbouring fibers is less than d .

Where d is the fiber diameter and l is the fiber length. As the distance between the fibers becomes less than l , they can no longer rotate freely and start to interact with each other thus contradicting Jeffery's assumptions. These interactions have to be accounted for in order to accurately predict the orientation.

In order to account for interactions, Folgar and Tucker [18] added a rotational diffusion term to Jeffery's model and assumed infinite aspect ratio A.R thus creating the following model:

$$\frac{d\theta}{dt} = -\sin(\theta)\cos(\theta)\frac{\partial v_x}{\partial x} - \sin^2(\theta)\frac{\partial v_x}{\partial y} + \cos^2(\theta)\frac{\partial v_y}{\partial x} + \sin(\theta)\cos(\theta)\frac{\partial v_y}{\partial y} - \frac{C_I\dot{\gamma}}{\psi_\theta}\frac{\partial\psi_\theta}{\partial\theta}, \quad (1.18)$$

where v_x is the fluid velocity in the direction of x , v_y is the fluid velocity in the y direction, C_I is the interaction coefficient, ψ_θ is the density distribution function of fiber orientation and $\dot{\gamma}$ is scalar value of a shear rate. Advani and Tucker [45] defined a second order orientation tensor a through the orientation distribution density function:

$$a = \int p \otimes p \psi(p) dp \quad (1.19)$$

The trace of a second order orientation tensor is always one, which sometimes makes it sufficient to track only one of the tensor diagonal values. A two dimensional orientation tensor meaning is shown in Figure 1.7. The Folgar-Tucker model in its orientation tensor form is given as:

$$\frac{da}{dt} = (\sigma \cdot a - a \cdot \sigma) + \lambda(D \cdot a + a \cdot D - 2a_4 : D) + 2qC_I\dot{\gamma}\left(\frac{I}{q} - a\right), \quad (1.20)$$

where a_4 is 4th order orientation tensor, I is identity matrix and q is the problem dimension such that for the two dimensional case $q = 2$. Fourth order orientation tensor a_4 is complicated to calculate and thus it should be approximated through the second

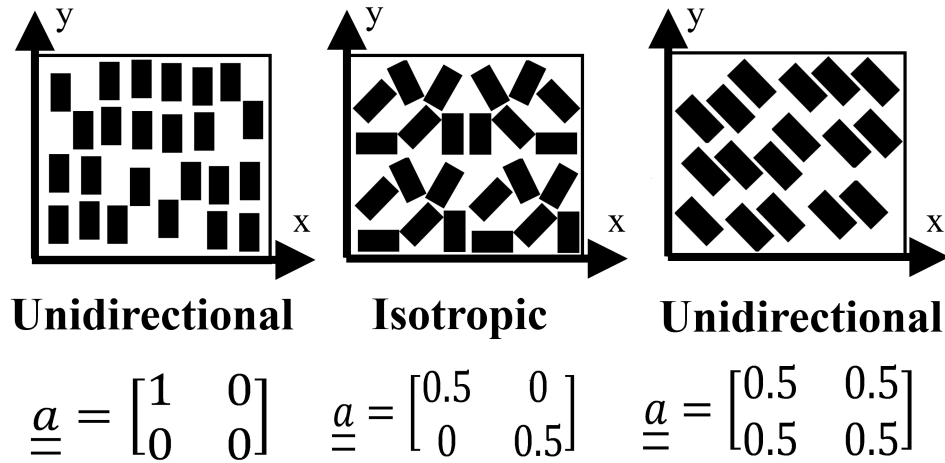


Figure 1.7: Two dimensional orientation tensor representation.

order orientation tensor a , the simplest of these approximations is called the “quadratic approximation” [46, 47]:

$$a \otimes a = a_4 \quad (1.21)$$

Other more complicated approximations can be found in the literature [46, 48, 49]. Advani and Tucker [45] solved the Folgar-Tucker model eq. (1.20) for different a_4 approximations.

Bay [50] proposed a correlation for the interaction parameter C_I as a function of fiber volume fraction c and ellipsoid axis ratio $A.R$:

$$C_I = 0.0184 \cdot e^{-0.714 \cdot c \cdot A.R} \quad (1.22)$$

Phan-Thien et al. [51] suggested another correlation for C_I :

$$C_I = M (1 - e^{-B \cdot c \cdot A.R}), \quad (1.23)$$

where M and B are constants, which were found by comparison to experimental data to be 0.03 and 0.224 respectively.

Ferec et al. [52] modified the Folgar-Tucker model by replacing the constant interactions coefficient C_I with a function that depends on the fiber orientation probability

function.

The Folgar-Tucker model is widely used for injection molding simulation of short fiber composites [53–55].

It was found that systems simulated by the Folgar-Tucker model orient with the flow faster than what could be seen from experimental results. Huynh [56] found that experimentally tested injection molded parts were at an orientation level, which required five to ten times less shear rate than what the Folgar-Tucker model would predict to require in order to achieve similar orientation level for the same flow time. Huynh added a parameter H to the Folgar-Tucker model in order to slow the orientation predicted by Folgar-Tucker:

$$\frac{da}{dt} = H \left((\sigma \cdot a - a \cdot \sigma) + \lambda (D \cdot a + a \cdot D - 2a_4 : D) + 2qC_I \dot{\gamma} \left(\frac{I}{q} - a \right) \right), \quad (1.24)$$

$1/H$ is the strain reduction factor and is defined between infinity and 1, where the $H = 1$ corresponds to the Folgar-Tucker model.

Sepehr et al. [57–59] tried to predict the stress in the compression experiment using the orientation calculated by the Folgar-Tucker model, and like Huynh [56] they found that the calculated stress diverges from the experimental value. In order to achieve a match between computational and experimental results they had to use a reduced shear rate in Folgar-Tucker model calculations.

Although Huynh's [56] SFR (Strain Factor Reduction) model gives good results in simple flows, it fails in a general case flow since the results depend on the coordinate system [60]. A more general model (RSC – Reduced Strain Closure) was developed by Wang et. al. [61]. In this model, the growth rate of eigenvalues of the orientation tensor is modified by an empirical factor k while the rotation rate eigenvectors remain unchanged.

$$\frac{da}{dt} = (\sigma \cdot a - a \cdot \sigma) + \lambda (D \cdot a + a \cdot D - 2[a_4 + (1 - k)(L_4 - M_4 : a_4)] : D) + 2qC_I \dot{\gamma} \left(\frac{I}{q} - a \right), \quad (1.25)$$

where L_4 and M_4 – the fourth order tensors are calculated from eigenvalues λ_i and

eigenvectors e_i calculated from the orientation tensor a :

$$L_4 = \sum_{i=1}^3 \lambda_i e_i e_i e_i e_i \quad (1.26)$$

$$M_4 = \sum_{i=1}^3 e_i e_i e_i e_i \quad (1.27)$$

k - empirical constant ≤ 1 , For $k = 1$ RSC is the Folgar-Tucker model.

The RSC model gives a good prediction for short fiber composites (0.2–0.4mm fibers); however, it fails for longer fibers. Anisotropic Rotary Diffusion (ARD) model [62] was developed for long fiber injection molding (10 – 13mm fibers) prediction.

$$\begin{aligned} \frac{da}{dt} = & (\sigma \cdot a - a \cdot \sigma) + \lambda (D \cdot a + a \cdot D - 2[a_4 + (1 - k)(L_4 - M_4 : a_4)] : D) \\ & + 2k (\text{tr} C) a - 5 (Ca + aC) + 10 (a_4 + (1 - k)(L - M : a_4)) : C \end{aligned} \quad (1.28)$$

C - Rotary diffusion tensor

$$C = b_1 I + b_2 a + b_3 a^2 + b_4 \frac{D}{\dot{\gamma}} + b_5 \frac{D^2}{\dot{\gamma}^2}, \quad (1.29)$$

where b_i are empirical constants that have to be fitted experimentally.

ARD provides similar results to RSC for short fiber and better prediction for long fibers. Although the long fiber referred to in regards with ARD are still much shorter than fibers in the LFT-D process.

Although the fibers described in this section are much shorter than the fibers that are targeted for this research, the results obtained by the methods described above are still important. Long fibers could be broken down in to smaller components whose average orientation would influence the rheology.

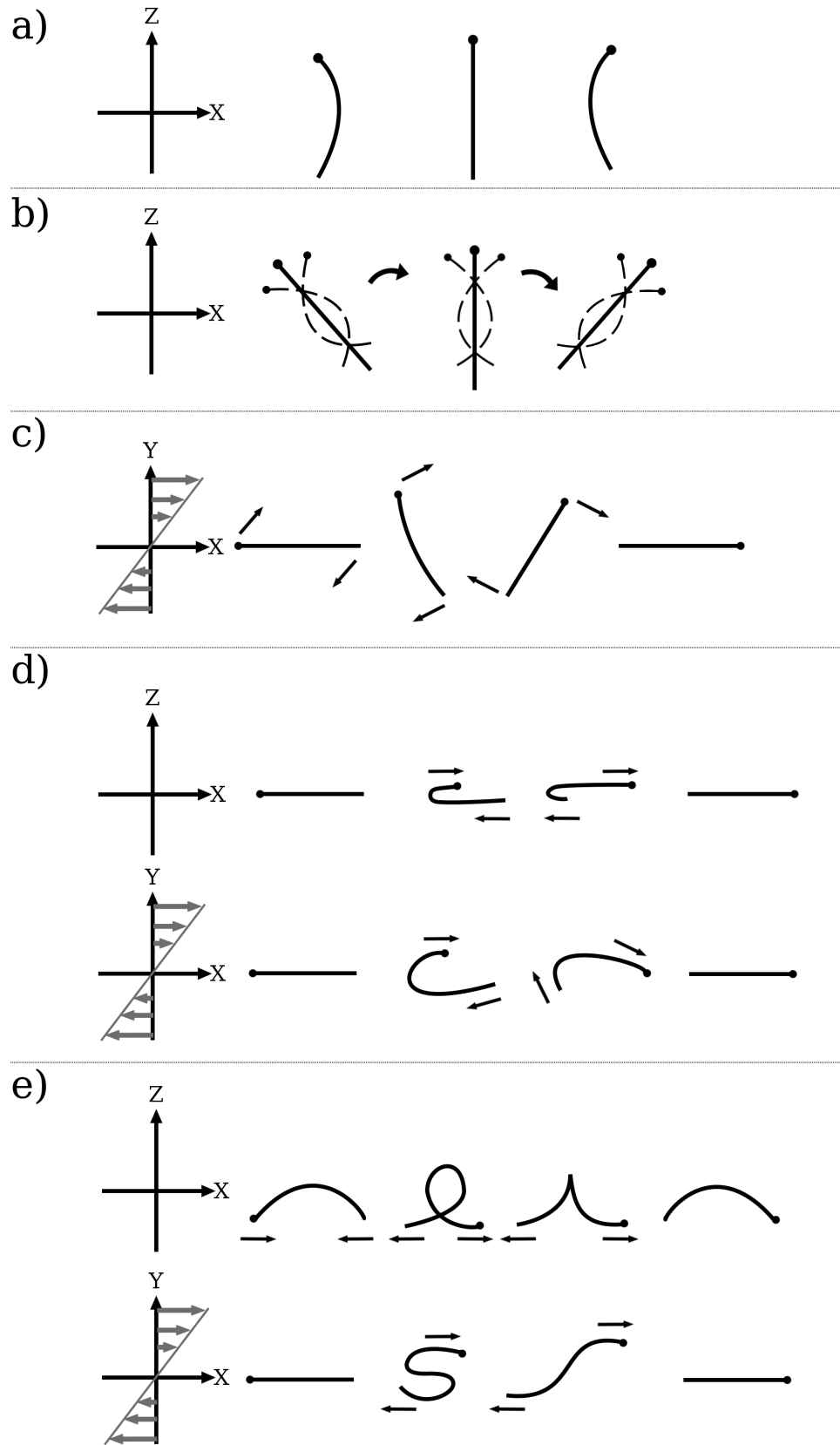


Figure 1.8: Different groups of fiber deformations in simple shear flow [63]; a)axial spin, b)flexible spin, c)springy rotation, d)snake turn, e)S-turn.

1.4 Flexible Fibers

As previously mentioned fiber length in LFT-D material can reach up to 80 mm, which violate the assumption of short rigid fibers used in Jeffery’s model [16], hence models that use Jeffery’s model as their base shouldn’t be used to simulate this process. Long fibers will exhibit bending during the flow. It is important to predict fiber bending in the composite since the fiber’s shape affects composite properties [14].

Forgacs and Mason [31, 32] and Arlov et. al. [63] experimentally investigated flexible fiber dynamics under the influence of simple shear flow. They classified the results into three groups:

- i. Fiber is performing an axial spin during which it bends into an arch and straightens (Figure 1.8a).
- ii. Fiber is performing a “flexible spin rotation” which is basically the bending described in group i superimposed on a spherical elliptical orbit (Figure 1.8b).
- iii. Third group behaviour is preferred by flexible fibers and it could be further subdivided into three more groups:
 1. “Springy” rotation, in this group the fiber initially is aligned with x axis after which the fiber starts to bend like a leaf spring. Eventually the fiber straightens and aligns again with x axis (Figure 1.8c).
 2. “Snake Turn”, this group behaviour is similar to group ”springy” rotation but with bigger bending due to higher flexibility (Figure 1.8d).
 3. “S-turn”, this behaviour is observed for highly symmetrical fiber. Initially the fiber is aligned with x axis and subsequently bends into “S” shape while rotating. Eventually the fiber is straightens and aligns again with x axis (Figure 1.8e).

1.4.1 Orientation Models - Flexible Fiber

There are several models in the literature that describe the behaviour of a flexible fiber in a flow field, the first of which was made by Hinch [64]. Hinch simplified the problem by

neglecting the fiber's width and assuming infinite elasticity (infinite Young's modulus), thus preventing the fiber from rotating in simple shear flow and stretching.

Yamamoto and Matsuoka [65] created a model referred to in the literature as the "bead-chain" model. In this model, fibers are represented as a collection of beads connected to each other through elastic springs. Each bead experiences hydrodynamic force and torque as well as interactions with its neighbours, which include: bending torque, twisting torque, elastic force and friction force. This model was used by Joung et. al. [66] to predict the dependence of viscosity of a Newtonian flexible fiber suspension with orientation.

Skjetne et. al. [67] created an alternative model where spheres were connected through rigid hinges, which insured the continuity of the fiber without the need of iterations on locations of the spheres. Although Skjetne et. al. [67] found a way to reduce the calculation time required by Yamamoto and Matsuoka [65] it was still significant due to the need for an enormous number of spheres for long fiber representation.

Ross and Klingenberg [68] proposed a similar model to Skjetne et. al. [67] with the difference that they connected prolate spheroids through rigid hinges, which reduces the number of elements needed to be calculated. The downside of this approach is that it requires the use of complicated rotational friction coefficients for ellipsoids [69].

Strautins and Latz [70] developed a semi-flexible model for dilute solutions. In this model a fiber can bend in one place creating two equal size rods connected in the middle. The model equations calculate the moments of orientation for these rod segments. Ortman et. al. [71] modified this model by adding an interaction term to the equations in a similar way to that of Folgar and Tucker [18] who modified Jeffery's model [16] in order to account for interactions and to be fit to use for concentrated suspensions.

1.5 Interactions

Simulation of a single fiber behavior presents an interesting physical problem, but it is not very practical. Composite materials consist of many fibers and thus interactions between them must be accounted for. Mason and Manley contributed to early interaction

theory [24, 72, 73] .

1.5.1 Interaction Between Spheres

Two spheres in a simple shear flow would collide and form a “doublet” particle. This particle would then rotate until the aggregate is broken into the two initial spheres [72]. For the case of collision of spheres with different diameters [73] similar results are obtained for spheres with diameter ratio of two or less, while for a larger diameter ratio the relations between two spheres is more complex, which is attributed to the the difference in sedimentation velocity due to the difference between sphere and fluid density. Mason and Manley [72, 73] found that after collision and the “doublet” rotation, the spheres separate at the mirror image point to the point of impact, which suggests that the system has a “memory”. This is possible only if the system has both repulsive and attraction forces.

The attraction force between the spheres could include a lubrication force. Yamamoto and Matsuoka [74] assumed that lubrication forces come into effect when the distance between the edges of two spheres is less than the radius of the spheres, Ferec et. al. [52] activated lubrication forces when the distance was less than the particle’s diameter. Kim and Karilla [69] expressed lubrication forces for two spheres of the same radius through eq. (1.30)

$$F_{lub} = - \left(\frac{3\pi\mu r}{\zeta} + \frac{27\pi\mu r}{20} \log \left(\frac{1}{\zeta} \right) \right) n_{ij} \cdot (u_i - u_j) n_{ij}, \quad (1.30)$$

where r is sphere’s radius, ζ is dimensionless distance between the edges of the spheres, n_{ij} is unity vector between two spheres, u_i and u_j is spheres velocity.

Ladd [75] simplified the expression by neglecting the logarithmic term in the equation as it is much smaller than the other term due to the fact that lubrication forces are active only in close proximity of both objects to each other.

$$F_{lub} = - \left(\frac{3\pi\mu r}{\zeta} \right) n_{ij} \cdot (u_i - u_j) n_{ij} \quad (1.31)$$

Eq. (1.31) suggests that the spheres will be attracted to each other when they are

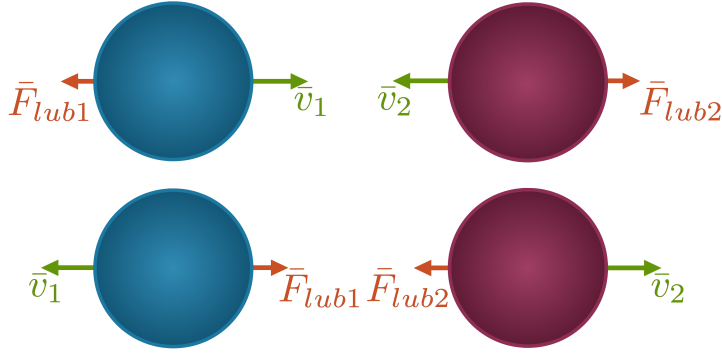


Figure 1.9: Lubrication forces.

moving away from each other while when the spheres are moving toward each other the force will become repulsive, shown in Figure 1.9. At the point of contact ($\zeta = 0$) expression in eq. (1.31) becomes singular thus lubrication force denies the possibility of contact.

1.5.2 Interactions Between Fibers

While interactions between equal diameter spheres cause always a symmetric response due to spheres symmetry in fibers this is not the case, as the contact point is rarely symmetric on both fibers. In addition the contact point is very small compared to the size of the fiber.

Yamamoto and Matsuoka [74] implemented lubrication force into their “bead-chain” model [65] in order to simulate interactions between rigid fibers. Joung et. al. [66] used the Yamamoto and Matsuoka [74] model to simulate interactions between flexible fibers.

In a simple shear flow interacting rigid fibers would approach one another and get associated for a time, followed by separation and rotation in orbits different from before the interactions [24]. Mason and Manley [24] showed that the period of rotation T is influenced by interactions.

Russel et. al. [76] showed that lubrication forces are strong between spheres, but are weak between fibers, which can lead to mechanical contacts between them. Sandararajakumar and Koch [77] assumed direct contacts between fibers and used them as main interaction mechanism neglecting lubrication force in their 3D simulation but used it in

case of 2D. Harlen et. al. [78] used the Sandararajakumar and Koch model [77] while also implementing friction forces between fibers.

Schmid et. al. [79] integrated repulsion forces which prevented fiber overlap and friction forces into the Ross and Klingenberg flexible fiber model [68] to simulate interaction between flexible fibers. Klingenberg used repulsive force between fibers to prevent them from overlapping [79] this force is presented in eq. (1.32)

$$F = -f(-20\zeta)n_{ij}, \quad (1.32)$$

where ζ is the distance between two cylinders at the point of interaction normalized to the radius of the cylinders, n_{ij} is unity vector which points from cylinder i to rod j at the interaction point and it is perpendicular to both cylinder surfaces, $f = 120\pi\mu lr\dot{\gamma}$ is empirically found with l equal to cylinder's length, r cylinder's diameter, μ is fluid's viscosity and $\dot{\gamma}$ is the shear rate.

Lee and Springer [80] used collisions to simulate interactions between rigid ellipsoids, and they assumed that collisions affect only the radial velocity of the fiber while leaving the linear velocity unchanged.

1.6 Rheology

1.6.1 Homogeneous Systems

Rheology is translated from Greek as "study of flow". Stress measures the internal body resistance to applied force. This resistance is the result of intermolecular forces. Shear stress is measured in Pascal (Pa) units, but it is different from pressure in the sense that pressure is force acting perpendicular to the surface, while shear stress measures the force which acts in parallel to the surface. Imagine two rectangular plates of area A at a distance Y from each other with fluid between the two. The upper plate is moved by force F at a velocity of U and the bottom plate is stationary. Assuming a no slip condition on both plates will result in zero velocity of fluid touching the bottom plate and velocity of U for the fluid touching the upper plate. Newton defined the force F

as [81]:

$$F = \mu \cdot A(du/dy) \quad (1.33)$$

μ is proportionality constant also called viscosity which is constant for Newtonian fluid and could be simply defined as:

$$\mu = \frac{\tau}{\dot{\gamma}} \quad (1.34)$$

where τ is the shear stress and $\dot{\gamma}$ is the shear rate. Examples for Newtonian fluids are: water, air, kerosene etc. In a power-law fluid [82], viscosity is not constant, and depends on shear rate:

$$\mu = K\dot{\gamma}^{n-1} \quad (1.35)$$

From eq (1.35) for the case $n = 1$ the material will have a constant viscosity or in other words will behave like Newtonian fluid. In the case of $n < 1$ material will be called *shear thinning* material meaning that its viscosity will decrease with shear rate. While for the case $n > 1$ the material will be called *shear thickening* material meaning that its viscosity will increase with shear rate. Examples for power-law fluids are: polymer melts, polymer solutions, petroleum jelly etc.

A more complex model is Herschel-Bulkley. The general Herschel-Bulkley equation is given by:

$$\tau = \tau_0 + K\dot{\gamma}^n \quad (1.36)$$

where τ is the shear stress, $\dot{\gamma}$ is the shear rate, τ_0 is the yield stress, K the consistency index, and n is the flow index. For $\tau < \tau_0$, Herschel-Bulkley fluid behaves as a solid. From eq (1.36), the general Herschel-Bulkley equation is reduced to the Newtonian case where $\tau_0 = 0$ and $n = 1$. Viscosity of Herschel-Bulkley fluid could be expressed through eq. (1.37):

$$\mu = \begin{cases} \mu_0, & \text{if } |\dot{\gamma}| \leq \dot{\gamma}_0 \\ K|\dot{\gamma}|^{n-1} + \tau_0|\dot{\gamma}|^{-1}, & \text{if } |\dot{\gamma}| \geq \dot{\gamma}_0 \end{cases} \quad (1.37)$$

Examples for Herschel-Bulkley fluids are: margarine, mayonnaise, ketchup, etc. [83] In order to predict material flow properties in processing it is essential to know the rheology of the system.

1.6.2 Fiber Filled Systems

A common model used in the literature for dependence of rheology on fiber concentration and orientation is given by [84, 85]

$$\tau = 2\mu_m [D + f(A.R, c) D : a_4], \quad (1.38)$$

where:

$$f(A.R, c) = \frac{A.R^2 c (2 - (c/G))}{4 (\ln(2A.R) - 1.5) (1 - (c/G))^2}, \quad (1.39)$$

$$G = 0.53 - 0.13A.R, \quad (1.40)$$

$$5 < A.R < 50 \quad (1.41)$$

where τ is stress, μ_m is matrix viscosity, D is the deformation tensor, a_4 is the fourth order orientation tensor, c is fiber volume fraction and $A.R$ is the axis ratio (length/diameter). More extended explanation of this model can be found in Ortman et. al. [71].

Hence rheological properties of the system are dependent on fiber orientation. Several experimental techniques have been developed to study the rheology of thermoplastic fiber composites. Capillary [86] and rotational [87] rheometers could be used to study short fiber filled systems while for the long fiber systems sliding plate rheometer [71] and the squeeze flow rheometer [88, 89] are used.

In the sliding plate rheometer, the plate slides at a constant rate while measuring the resistance of the material which is the shear stress. In the squeeze plate rheometer, the material is squeezed at a constant rate while measuring the force applied on the material,

which could be recalculated into stress.

It is hence needed to estimate fiber orientation in the material in order to calculate material rheological properties. As the focus of this work is in compression molding, the following section will examine squeeze flow.

1.7 Squeeze Flow

Squeeze flow modeling in the literature was done for various types of fluids: Newtonian [90–94], Herschel-Bulkley [95, 96] and power-law [97–99]. These models neglect inertial forces thus assuming quasi steady state flow resulting in all time derivatives equal to zero. In addition, they assume that the samples are very thin making the velocity of flow in the direction of squeezing (vertical) orders of magnitude lower than the horizontal direction and thus negligible. The resulting model becomes a one dimensional Hele-Shaw solution for thin gaps.

Squeeze flow can also be subdivided into two limiting cases. In the first case a no slip condition is applied at the interface with the wall. In this case, the velocity profile will be parabolic for a Newtonian fluid [90, 92, 94]. The second limiting case is a perfect slip condition in which the velocity profile will be of a plug flow type [95] Mavridis et. al. [94] and Lawal and Kalyon [95] simulated and compared solutions with different slip coefficient value β , which was used to define slip velocity v_s [100] as:

$$v_s = \beta\tau_\omega, \quad (1.42)$$

where β is the slip coefficient, τ_ω is the tangential stress at the wall and v_s is the slip velocity.

Barone [93] developed mathematical and experimental methods to investigate a friction mechanism at the mold-charge interface. Zhang [97] proposed a squeeze flow model for thin films and then confirmed it with experiments. Lee et.al. [99] found that squeezing thin film of a power law fluid resembles the behavior of a Newtonian fluid. Hence the solution of a thin Newtonian case is of interest even for thermoplastic, power-law, materials application.

Rheometric two dimensional squeeze flow of an incompressible Newtonian fluid can be expressed through the following equations:

$$\frac{\partial u}{\partial t} + u \frac{\partial u}{\partial x} + v \frac{\partial u}{\partial y} = \frac{-1}{\rho} \frac{\partial p}{\partial x} + \nu \left(\frac{\partial^2 u}{\partial x^2} + \frac{\partial^2 u}{\partial y^2} \right), \quad (1.43)$$

$$\frac{\partial v}{\partial t} + u \frac{\partial v}{\partial x} + v \frac{\partial v}{\partial y} = \frac{-1}{\rho} \frac{\partial p}{\partial y} + \nu \left(\frac{\partial^2 v}{\partial x^2} + \frac{\partial^2 v}{\partial y^2} \right), \quad (1.44)$$

$$\frac{\partial u}{\partial x} + \frac{\partial v}{\partial y} = 0, \quad (1.45)$$

Thorpe [101] accounted for inertia effects and provided a solution for a two dimensional squeeze flow problem. Gupta and Gupta [102] have shown that there is a similarity solution of two dimensional squeeze flow problem for Newtonian isothermal case with boundary conditions eq. (1.46) if the distance between the plates is in the form of eq. (1.47):

$$u(x, 1, t) = 0; v(x, 1, t) = v_w, v(x, 0, t) = 0; \frac{\partial u}{\partial y}(x, 0, t) = 0, \quad (1.46)$$

$$a(t) = (a_o^2 + Mt)^{0.5}, \quad (1.47)$$

where a_o is the initial half distance between the plates and $M = -2\nu R$ where ν is the kinematic viscosity and R is a constant equal to av_w/ν .

Velocity values as a function of time could be obtained by calculating the derivative of eq. (1.47) with respect to time, the resulting expression is given in eq. (1.48).

$$V_w = 0.5M (a_o^2 + Mt)^{-0.5} \quad (1.48)$$

The two dimensional squeeze flow system can be divided into four quadrants, and due to symmetry only one quarter has to be solved in order to obtain the solution of the system, as shown in Figure 1.10. The axes on Figure 1.10 appear in dimensionless form where the horizontal center line is located at $y = 0$, the center of the horizontal line is at

$x = 1$ and the top plate is located at $y = 1$. The solution to the two dimensional squeeze flow problem (solution of the upper left quarter in Figure 1.10) is given by eqs. (1.49)-(1.50)

$$v_x = \frac{c-x}{a(t)} v_w(t) f'(R) \left(\frac{y}{a(t)} \right), \quad (1.49)$$

$$v_y = v_w(t) f(R) \left(\frac{y}{a(t)} \right), \quad (1.50)$$

where c is the distance between the center and the edge of the system in the x direction, $f(R)$ is given by Gupta and Gupta [102].

$$f = f_0(a) + R f_1(a) + R^2 f_2(a) \quad (1.51)$$

where:

$$f_0(a) = \frac{3a}{2} - \frac{a^3}{2} \quad (1.52)$$

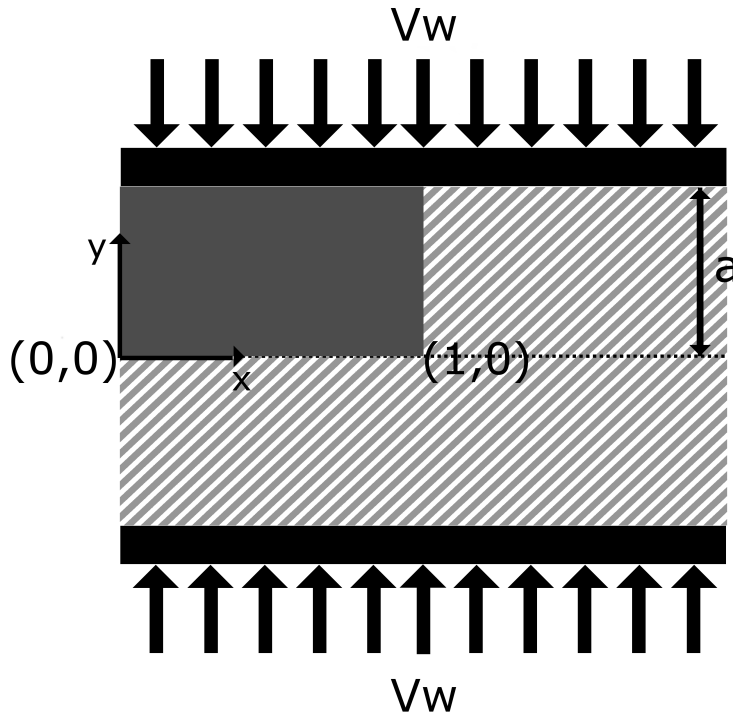


Figure 1.10: Squeeze flow system.

$$f_1(a) = \frac{a^5}{10} - \frac{a^7}{280} - \frac{53a^3}{280} + \frac{13a}{140} \quad (1.53)$$

$$f_2(a) = E_3a + \frac{E_1a^3}{6} + \frac{53a^5}{1400} - \frac{579a^7}{58800} + \frac{a^9}{2016} + \frac{a^{11}}{92400} \quad (1.54)$$

with $E_1 = -0.2892701$ and $E_3 = 0.0196946$.

1.8 Objectives

The single rigid fiber model described in Chapter 1 [16] and subsequently the models for multiple fibers [18], [56], [61], [62], [71] are all inherently designed for short fibers due to torque calculation in the center mass of the fiber. The same approach is used in the described flexible fiber model [68]. Other models described in Chapter 1 [65], [67], [38] could be applied for long fibers but they would require a massive amount of calculations. In addition all of the described models were only tested in the literature on a simple shear flow case and it is unclear how well they would perform under the influence of a more complex flow. Hence the objectives of this thesis work are as follows:

- i. Develop computationally cheap method for torque calculation on long fibers.
- ii. Develop a model for long rigid fibers orientation under the influence of a flow field.
- iii. Using the developed model for long rigid fibers develop a model for long flexible fibers.
- iv. Integrate interactions between fibers into developed long flexible fiber model.
- v. Validate the model using existing literature data for simple shear flow.
- vi. Generate results for response of long flexible fiber to a squeeze flow field and validate some of the results experimentally.

Chapter 2

Long Fiber Model Development

2.1 General Approach

In Chapter 1 models representing flexible fibers through connected rigid spheres or prolate spheroids were described [64], [65], [67] [68]. The difference between the model proposed in this thesis and models found in the literature is the use of cylinders as rigid segments in addition to development of a new method for torque calculation in order to account for the extreme length of the fibers.

In the proposed model long flexible fibers are represented as a collection of rigid short cylinders which interact with each other at the connection point as shown in Figure 2.1. In order to calculate the hydrodynamic torque on each rigid segment, its projection length on the $(x - y)$ axes are calculated and divided into spheres with hydrodynamic torque calculated on each sphere. This approach is in contrast with the general practice in the literature to calculate the vorticity [64], [65], [67], [68] in the middle of a segment geometry and deduct its radial velocity from it. For long fibers, vorticity could change significantly, and not always symmetrically along the fiber, thus the approach used in this thesis is more suitable for long fibers. In addition, rotational friction coefficients for cylinders were derived for this model. In case of crossover between various rigid segments, the cylinders that interact with each other are represented as a collection of spheres and elastic collisions are calculated

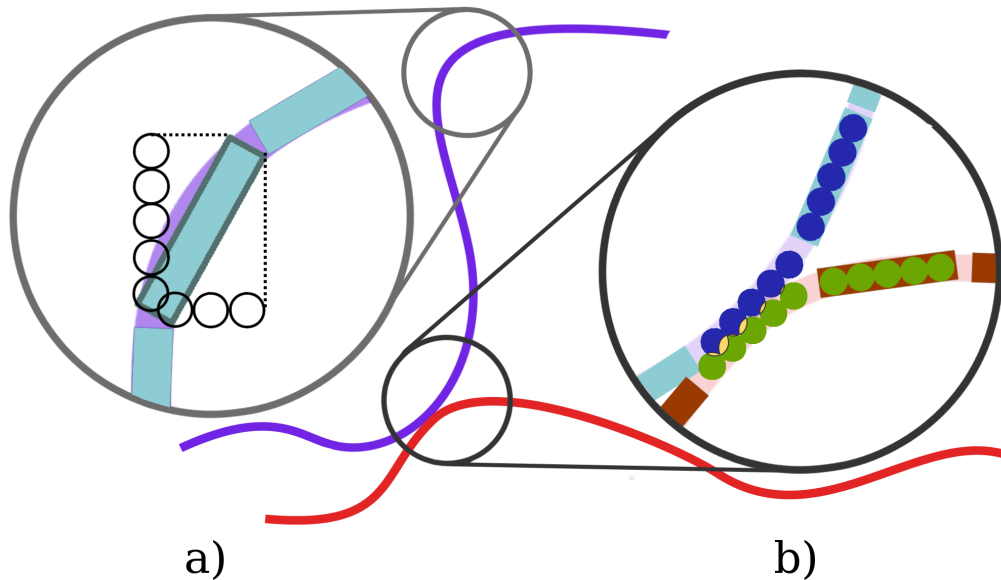


Figure 2.1: Graphic model representation; a) Cylinder is represented through projections divided into spheres for hydrodynamic torque and force calculation. b) Cylinder is represented through a collection of spheres for interactions calculations.

between them.

Computationally the model is divided into two parts where in the first part the equations for rigid cylinders movement will be solved. In the second part, interactions between adjacent rigid cylinders will be solved. Equations for interactions are included for the cases where rigid segments overlap each other. Model derivation is explained in the following sections.

2.2 Rigid Cylinder

2.2.1 Infinite Axis Ratio Cylinder

In order to solve the movement of the rigid cylinder it is necessary to solve both linear and rotational movement equations. Similar assumptions to Jeffery [16] regarding the linear movement, namely that the rigid cylinder's center mass is at rest with respect to the fluid, were used in this model. In other words, the linear velocity of the cylinder is the same as the velocity of the fluid in the center of mass of the

cylinder. This assumption will be discussed later on and what it implies will be shown.

In order to calculate the rotation of a rigid cylinder in the direction of its minor axis around its center of mass, the torque balance equation [103], [104] is solved:

$$a \frac{d\omega}{dt} = P - k\omega, \quad (2.1)$$

where a is moment of inertia, ω is rotational velocity, k is rotational friction coefficient and P is the torque acting on the cylinder. This problem is separated into two parts, where the first part is calculating the hydrodynamic torque P acting on the cylinder and the second part is calculating the rotational friction coefficient k . In order to calculate the torque acting on the cylinder, the cylinder's projections were calculated on the x and y axes. These projections were divided into spheres (Figure 2.4) to calculate the force acting on a sphere using Stokes law:

$$F = 6\pi\mu r (V_f - V_s), \quad (2.2)$$

where μ is fluid viscosity, r is sphere radius, V_f is the velocity of the fluid and V_s is the velocity of the sphere. Velocity of the sphere is given by linear and radial velocity of the cylinder:

$$V_s = V_c + \omega \times l_s, \quad (2.3)$$

where V_c is linear velocity of the cylinder, ω radial velocity of the cylinder and l_s is the vector connecting the center of the cylinder to the sphere. Since radial velocity adds to and reduces the velocity of the spheres above and below the center mass of the cylinder by the same amount, and it is desired to calculate the overall force contribution, it is possible to look at the linear velocity of the spheres simply as the linear velocity of the cylinder's center of mass. Note that the spheres representing the projection on the y axis are not generating any force due to the velocity compo-

ment from y direction and vice versa. Torque contribution from each sphere is then calculated, by vector multiplication of vector connecting the center of the projection with the center of the contributing sphere:

$$P = l_s \times F, \quad (2.4)$$

where P is torque, F is force and l_s is the vector connecting center mass of the cylinder to the corresponding sphere. All of the contributions are then summarized to provide integrated value for the hydrodynamic force and torque acting on the cylinder because of the summation radial velocity could be disregarded during the drag force calculation since it will cancel each out from both sides of the cylinder (different sign of linear velocity on both sides). As the fiber will rotate the values of projections on the axes will change. The projections are always broken into constant number of spheres B which was set to 100 (it was found that 10 spheres produce just as good results but it might not be sufficient for a higher value of shear rate).

Equations for both force and torque are needed to describe the motion of a single rigid cylinder movement. It could be assumed that the linear velocity of the cylinder is the velocity of the fluid in the center of mass. Thus for now let's concentrate on eq. (2.1) for torque balance. In order to solve eq. (2.1), an expression for friction coefficient k is required. To the best of our knowledge an expression for k for a cylinder is not available in the literature. There is, however, a well-known friction coefficient calculation method for an ellipsoid shaped particle [52,69] which is widely used in the literature.

In order to find an expression for k , Jeffery's model eq. (1.7) was applied for an infinite axis ratio fiber (in this case an ellipsoid and a cylinder should give the same result) under the influence of simple planar shear flow:

$$v_x = \dot{\gamma}y, \quad (2.5)$$

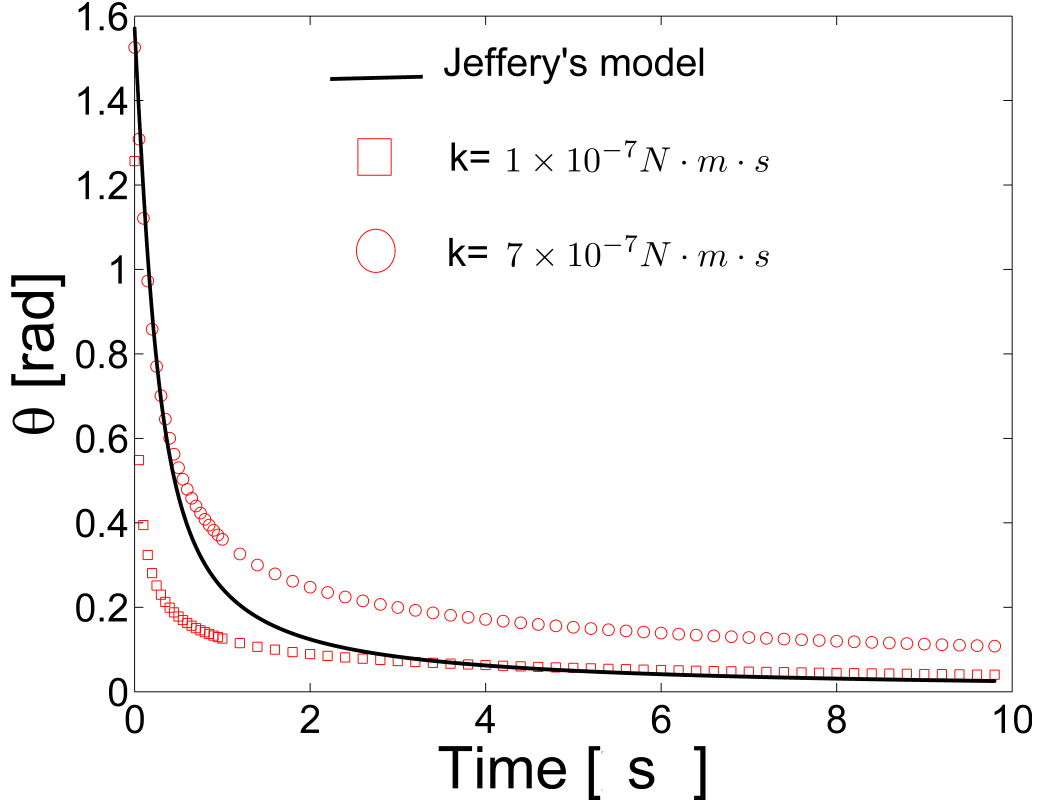


Figure 2.2: Comparison between Jeffery's model and current model for the case of constant friction coefficient in interval $[\pi/2, 0]$.

$$v_y = 0, \quad (2.6)$$

where $\dot{\gamma}$ is shear rate, v_x is the x component of velocity, v_y is the y component of velocity.

Figure 2.2 presents the solution of the model and its comparison to Jeffery's model for two cases of constant friction coefficient: $k = 10^{-7} \text{ N}\cdot\text{m}\cdot\text{s}$ (lower solution in Figure 2.2) and $k = 7\cdot 10^{-7} \text{ N}\cdot\text{m}\cdot\text{s}$. It is apparent from the results that the case $k = 7\cdot 10^{-7} \text{ N}\cdot\text{m}\cdot\text{s}$ fits better for the upper part of Jeffery's model solution while the case $k = 10^{-7} \text{ N}\cdot\text{m}\cdot\text{s}$ fits better for the lower part. Hence it could be seen that larger friction coefficient provides better fit for higher angles while lower friction coefficient provides better fit for the lower angles. Two conclusions could be made out of this experiment, the first is that friction coefficient should not be constant with respect to a cylinder's orientation and the second is that it should decrease with orientation

in the interval $[\pi/2, 0]$.

Several functions that decrease in the interval were attempted. The expression $K \sin(\theta)$ gave the best result in term of fitting to Jeffery's model. The physical interpretation behind it, is that as the projection of the fiber onto the y axis diminishes so diminishes the resistance to the flow perpendicular to the projection. Hence by analogy if the flow would be:

$$v_x = 0, \quad (2.7)$$

$$v_y = \dot{\gamma}x, \quad (2.8)$$

where $\dot{\gamma}$ is shear rate, v_x is the x component of the velocity, v_y is y component of the velocity. By analogy it is clear that the friction coefficient for the velocity described in eqs. (2.7)-(2.8) would be $K \cos(\theta)$, hence it is clear that friction coefficient depends on a flow direction. Therefore in order to solve a fiber orientation for a general two dimensional case in the Cartesian coordinate system, two equations are needed:

$$a \frac{d\omega_x}{dt} = P_x - K \sin(\theta_x) \omega_x, \quad (2.9)$$

$$a \frac{d\omega_y}{dt} = P_y - K \cos(\theta_y) \omega_y, \quad (2.10)$$

where a is the moment of inertia, ω_x is the angular velocity generated by forces from x direction, ω_y is the angular velocity generated by forces from y direction, P_x is the torque generated by forces from x direction, P_y is torque generated by forces from y direction, θ_x is the orientation caused by forces from x direction, θ_y is the orientation caused by forces from y direction. Eqs. (2.9)-(2.10) could also be presented in tensor form:

$$a \frac{d\omega}{dt} = \underline{P} - \underline{k}\omega, \quad (2.11)$$

where \underline{k} is given by:

$$\underline{k} = \begin{pmatrix} K_1 \sin(\theta) & 0 \\ 0 & K_1 \cos(\theta) \end{pmatrix} \quad (2.12)$$

θ_i and ω_i do not have any physical meaning, but their sum is the orientation angle and radial velocity respectively:

$$\theta = \sum \theta_i \quad (2.13)$$

$$\omega = \sum \omega_i \quad (2.14)$$

The justification behind decomposing cylinders rotation to rotation due to influence from x and y directions comes from the principle of superposition which is shown in Figure 2.3.

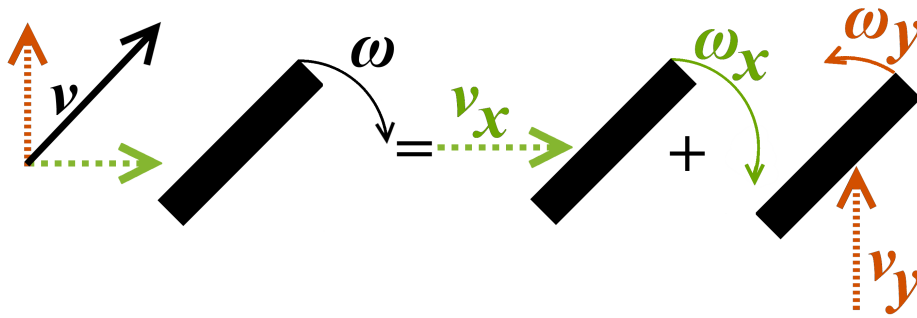


Figure 2.3: Superposition of forces on the cylinder.

2.2.2 Finite Axis Ratio Cylinder

An infinite axis ratio cylinder will orient itself with the direction of the flow for the simple shear flow case. Finite axis ratio cylinder, however, will continuously rotate due to the torque on the cross section of the cylinder. In the model the hydrodynamic torque is calculated on the cross-section of the cylinder (a disc). The

disc which represents the cross sectional area will be represented through two spheres connected at the center of the disc (Figure 2.4b). A projection of these spheres is calculated on the axes, these projections represent diameter of projected spheres which are influenced by the x and y components of the flow field. Stokes drag is calculated on each of the projected spheres and a torque that is generated by each projected sphere is calculated through vector multiplication of this force by the lever which is generated between the center mass of each projected sphere and the center of the disc which is described in eqs. (2.15)-(2.16)

$$F_{dn}^j = 6\pi r\mu(V^j - V_0^j), \quad (2.15)$$

$$p_{dn}^j = l_{dn}^i \times F_{dn}^j, \quad (2.16)$$

where F_{dn}^j is the force acting from direction j on cross section sphere n , r is the radius of the sphere on the cross section projection, V^j is the j component of fluid velocity at center mass of the sphere on the cross section, V_0^j is the j component of linear velocity of the cylinder, p_{dn}^j is the torque acting on sphere n on the cross

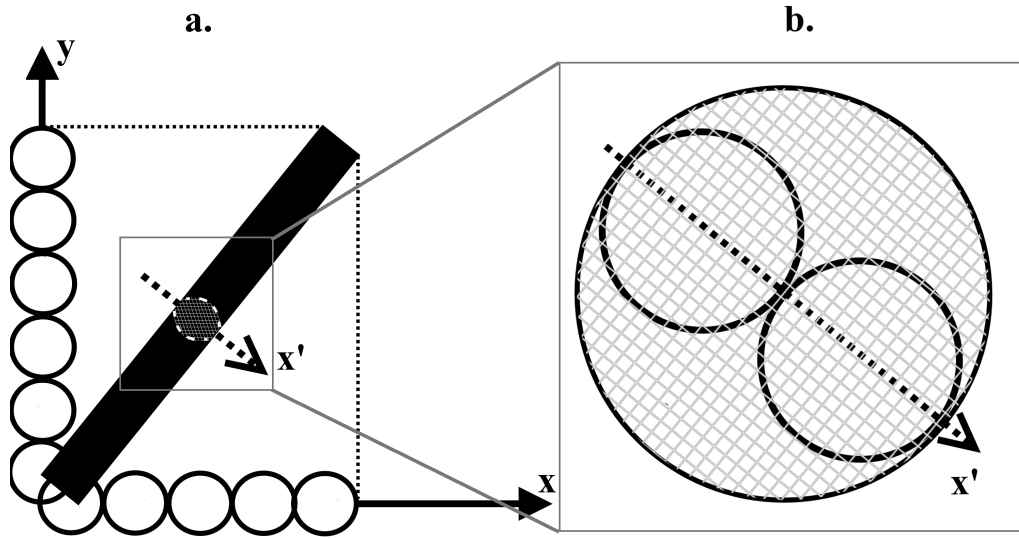


Figure 2.4: a. Representation of a cylinder through a collection of spheres on the cylinder projections. b. Representation of cylinder's cross section with two spheres.

section from j direction, l_{dn}^i is the vector connecting the center of the cross section and the center of sphere n , index i, j refers to direction from which the force or torque contribution comes and bottom index n refers for the sphere for which the contribution is calculated.

This procedure is done for both spheres and then summarized into total torque produced by the cross section:

$$P_d^j = p_{d1}^j + p_{d2}^j \quad (2.17)$$

Note that as the orientation of the fiber is changing l_{dn}^i and r will change as well, for example when the fiber is at vertical position (cross-section is horizontal position) l_{dn}^x and r_x will be equal to the radius of the spheres while l_{dn}^y and r_y will equal zero, shown in Figure 2.5. Since the cross-section area of two spheres is two times smaller than original disc, the calculated torque is multiplied by a factor of two.

Friction for the cross section must also be accounted for, hence eq. (2.12) for the case of finite axis ratio cylinder:

$$k = \begin{pmatrix} K_1 \sin(\theta) + K_2 \cos(\theta) & 0 \\ 0 & K_1 \cos(\theta) + K_2 \sin(\theta) \end{pmatrix} \quad (2.18)$$

where K_1 is a constant responsible of representing the resistance to the flow by the length of the cylinder and K_2 is a constant responsible of representing the resistance

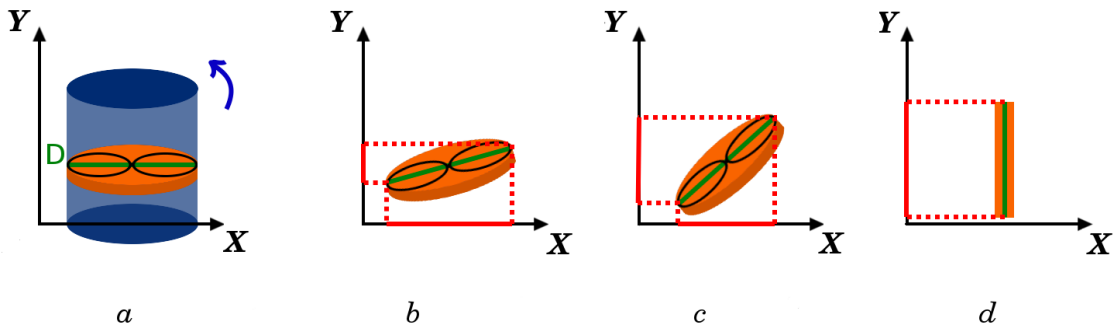


Figure 2.5: Cross section projections change during orientation.

to the flow by the cross section of the cylinder.

It is possible to make a similar assumption to Jeffery [16] and assume non-inertial flow which could be assumed for very low Reynold's number ($\ll 1$) [105] thus eliminating the derivatives in eq. (2.11) reducing it to:

$$0 = \underline{P} - \underline{k\omega} \quad (2.19)$$

Results obtained under this assumption are identical to results obtained by solving eq. (2.11) which proves that this assumption is valid. Note that infinite aspect ratio cylinder will orient itself with the flow under the influence of a simple shear flow. It will not be able to cross the axis in which the shear flow is happening or in other words it will not be able to rotate like a finite axis ratio cylinder.

2.3 Flexible Fiber

In order to obtain flexibility several rigid cylinders are connected together. Since equations of motion are calculated for every rigid cylinder, and in order to keep the overall fiber continuous several interactions between rigid fibers must be incorporated into the equations. The first interaction between adjacent rigid cylinders is elongation [65]. Elongation interaction comes into effect when the ends of two adjacent cylinders are about to separate and prevents it. As an analogy we can assume that the two cylinders are connected through an elastic spring and hence the force on each cylinder is the spring constant multiplied by the distance between the ends of the cylinders (Figure 2.6). In reality, glass and carbon fibers are non-expandable, but mathematically in order to connect rigid segments, the mechanism shown in Figure 2.6 is used. Another interaction between rigid segments is bending. This interaction comes into effect when the angle between two neighboring segments is different from the equilibrium angle (rigid rod) which is set as π .

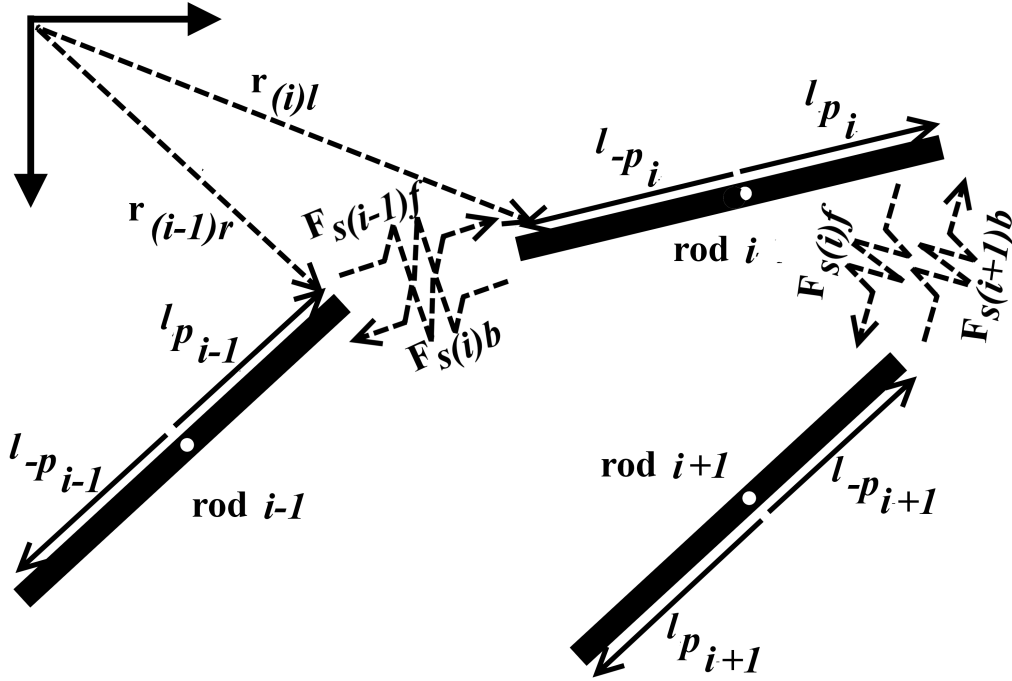


Figure 2.6: Schematic representation of rigid segments connected through elastic springs.

2.3.1 Elongation

Assume a cylinder of length l , radius r , Young's modulus E and a distance Δl to the next cylinder which has the same properties as the first. Then the elongation force F_e on both cylinders is described by eq. (2.20):

$$F_e = k_e(\Delta l), \quad (2.20)$$

where Δl is the distance between the rigid segments ends and k_e is elastic force constant. Since the force that each segment feel is proportional to Δl , it is assumed that the origin of the force is elongation of each segment by Δl (Figure 2.7), although in the current model segments have constant length this exercise is essential to express k_e through geometrical and physical properties of a segment.

Segment of length l stretched to length of $l + \Delta l$ will exhibit the following force:

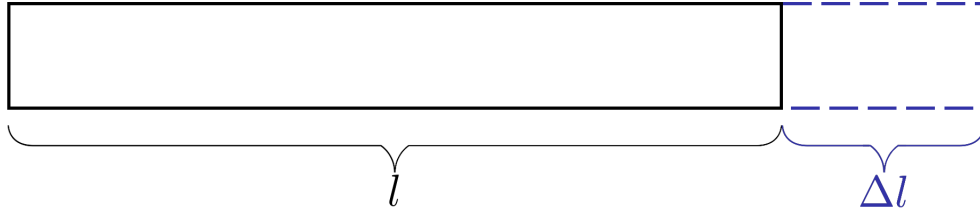


Figure 2.7: Elongation diagram.

$$F_{e1} = k_e \Delta l \quad (2.21)$$

This force would also generate a torque:

$$P_{e1} = 0.5l \times F_{e1} \quad (2.22)$$

Half of the segment taken to calculate elongation torque since the rotation happens around the center of the segment. Since from physics of rigid bodies it is known that:

$$\frac{F}{A} = E \frac{\Delta l}{l}, \quad (2.23)$$

$$F = EA \frac{\Delta l}{l}, \quad (2.24)$$

where A is the cross section area of the cylinder and E is Young's modulus. By comparing eq. (2.21) with eq. (2.24) it can be concluded that:

$$k_e = \frac{EA}{l} = \frac{\pi r^2 E}{l}, \quad (2.25)$$

Interactions like these are used by Yamamoto and Matsuoka [65] to describe interaction between spheres connected by elastic springs.

As was mentioned, the fibers with the proposed model are not extensible. Although elongation interactions are implemented to ensure fiber continuity, discontinuity can still occur. Due to the nature of elastic springs, the model form will allow fibers to

elongate (and thus become dis-continuous) under certain conditions such as, high elongation forces and low Young's modulus. Since Young's modulus is a physical property, it can not be set arbitrarily high to prevent elongation. In reality, inextensible fibers under such conditions will simply break but since breakage is not covered by the current model the fibers will appear to become longer. Hence the limit of such extension should be set as extension at break of the material. Numerically as the fibers extend, the rigid segments assembling this fiber should extend as well, but in the current model they stay the same, which results in inaccurate calculation of torque and friction coefficients hence under high elongation the model loses its accuracy.

2.3.2 Bending

The second interaction between rigid segments is resistance to bending. The bending torque is given by eq. (2.26).

$$P_b = k_b(\theta_0 - \theta), \quad (2.26)$$

where θ is the angle between two segments, θ_0 is the equilibrium angle between the two segments, which is taken as π , and k_b is bending constant. As in the case of k_e it is important to express k_b as a function of the material property and the geometry of the segments:

$$P_b = E \frac{I_A}{R}, \quad (2.27)$$

where R is radius of curvature and I_A is the area moment of inertia. From the geometry as represented in Figure 2.8:

$$\frac{\gamma}{2\pi} = \frac{l}{2\pi R}, \quad (2.28)$$

$$R = \frac{l}{\gamma}, \quad (2.29)$$

substituting eq. (2.29) into eq. (2.27)

$$P = E \frac{I_A \gamma}{l} \quad (2.30)$$

From the geometry as represented in Figure 2.8:

$$\gamma = \pi - \theta \quad (2.31)$$

and for circular cylinder with diameter d :

$$I_A = \frac{\pi d^4}{64}, \quad (2.32)$$

Substituting eqs. (2.31) and (2.32) into eq. (2.30)

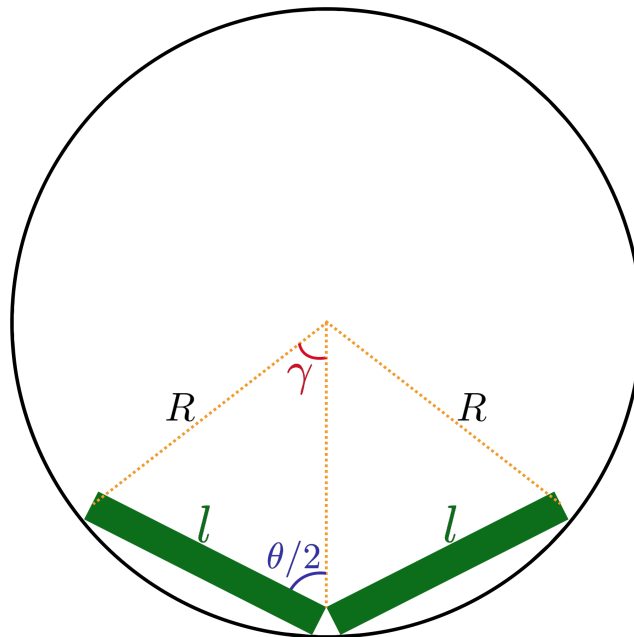


Figure 2.8: Bending diagram.

$$P_b = \frac{\pi E d^4 (\pi - \theta)}{64l} \quad (2.33)$$

By comparing eq. (2.33) with eq. (2.26):

$$k_b = \frac{\pi E d^4}{64l} \quad (2.34)$$

Schmid et. al. [79] and Yamamoto and Matsuoka [65] obtained the same expression for k_b . As seen from Figure 2.8, one of the base assumptions of this calculation is that the length of the arc with radius of curvature R is equal to $2l$, which is correct for small deformations. As the deformation of the fiber increases the model will

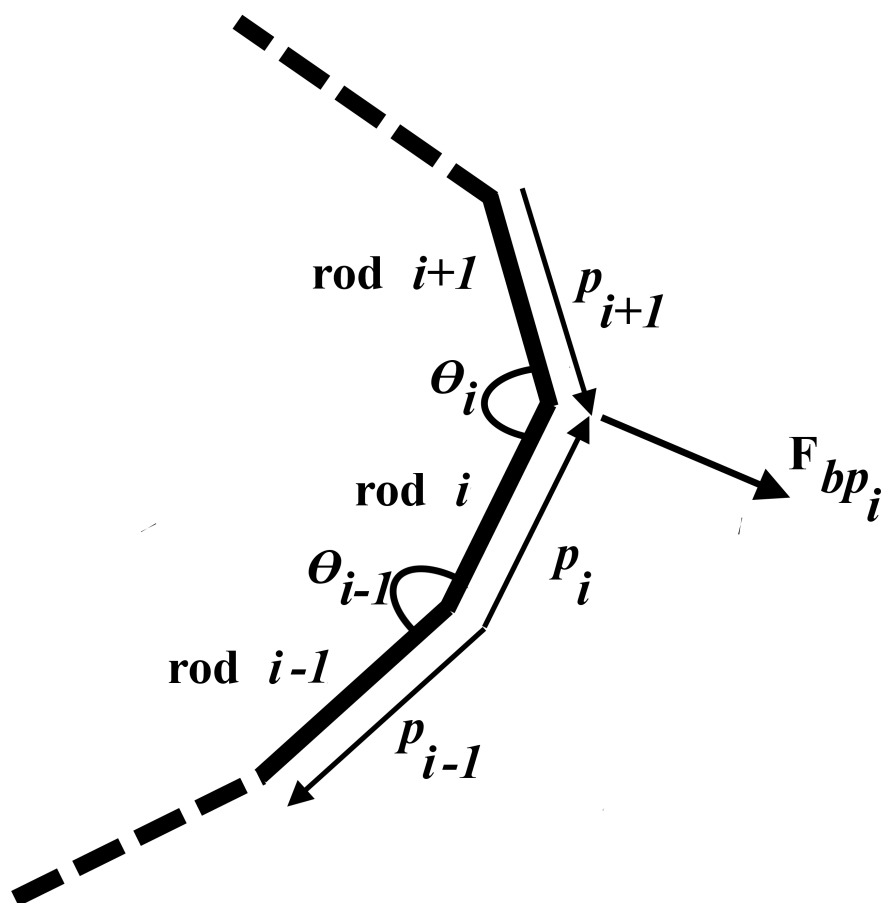


Figure 2.9: Schematic representation of bending torque with imaginary force F_{bp} .

become less accurate. As was previously shown, in order to solve eq. (2.19) the torque is decomposed into torque generated by forces from x and y directions. This is a simple task for torque which is calculated from forces (for example elongation torque eq.(2.22)) since the x and y vector components of the force are known. Since bending torque calculation path does not go through force calculation but rather a direct calculation of torque through eq. (2.26) its decomposition is more complex.

The direction of bending torque ϵ is calculated by:

$$\epsilon = \frac{p_i \times p_{i-1}}{(p_i \times p_{i-1})}, \quad (2.35)$$

where p_i and p_{i-1} are vectors representing rigid segments as represented by Figure 2.9.

In order to decompose the bending torque an imaginary force F_{bp} is employed. This force will be imaginary and will not participate in any calculations other than the decomposition calculation of the bending torque. This is done in the following manner:

- Set a unit vector ϵ to be perpendicular to a vector p_i representing a rigid segment.
- Calculate $p_i \times \epsilon$, if the result is of the same sign as the bending torque then ϵ is the direction of the force F_{bp} , else multiply ϵ by -1.
- Calculate the size of F_{bp} by:

$$F_{bp} = \frac{(P_b)}{l}$$

- The force size and direction are then ϵF_{bp}

Once the imaginary force vector is calculated the decomposition is trivial:

$$P_b^j = l \times F_{bp}^j \quad (2.36)$$

Since now there are multiple rigid segments connected to each other it can no longer be assumed that they are moving at the velocity of the fluid at their center of mass.

Linear and radial movement of rigid fibers is calculated through a force and torque balance on the fibers.

$$m \frac{dv^j}{dt} = F_h^j + F_e^j \quad (2.37)$$

$$a \frac{d\omega^j}{dt} = P_h^j - k^j \omega^j + P_e^j + P_b^j \quad (2.38)$$

Similar assumption to Jeffery [16] is made, assuming non-inertial flow, thus eliminating the derivatives in eqs. (2.37) and (2.38) reducing them to:

$$0 = P_h^j - k^j \omega^j + P_e^j + P_b^j \quad (2.39)$$

$$0 = F_h^j + F_e^j \quad (2.40)$$

In order to express the linear velocity of rigid segments from eq. (2.37), F_h^j is replaced with the drag force equation:

$$0 = \sum 6\pi r_i \mu (V^j - V_0^j) + F_e^j \quad (2.41)$$

From eqs. (2.39) and (2.41) expressions for radial velocity ω and linear velocity V are extracted:

$$\omega^j = \frac{P_h^j + P_e^j + P_b^j}{k^j} \quad (2.42)$$

$$V_0^j = \frac{\sum \mu 6\pi r_i V^j}{\sum 6\pi r_i \mu} + \frac{F_e^j}{\sum 6\pi r_i \mu} = V_{avg}^j + \frac{F_e^j}{\sum 6\pi r_i \mu} \approx V_{fluid} + \frac{F_e^j}{\sum 6\pi r_i \mu} \quad (2.43)$$

Eq. (2.43) is analytically correct for simple shear flow and other linear flows, while for non-linear flow it is an approximation for short cylinders. Practically it is hard to

calculate $\sum 6\pi r_i \mu$ where r_i is the radius of the projected spheres both from cylinder length and its cross-section since r_i is fiber diameter dependent and changes with orientation. Eqs. (2.44)-(2.45) were found to provide good results when compared to results obtained from the literature [34], [65], [79].

$$\sum 6\pi r_i^x \mu = 0.5 \cdot 6 \cdot \pi \cdot \mu (d + (l - d) \sin(\theta)) \quad (2.44)$$

$$\sum 6\pi r_i^y \mu = 0.5 \cdot 6 \cdot \pi \cdot \mu (d + (l - d) \cos(\theta)) \quad (2.45)$$

2.4 Interactions

In the proposed model, interactions are implemented through elastic collisions through the Walton and Braun model [106]. Cylinders are represented through a collection of spheres. In the next step, the distances between each two sphere's centers are calculated. Once the distance between the centers of spheres from different cylinders is less than the sphere's diameter, elastic collisions and subsequent torques are being calculated. Force and torque caused by collisions are:

$$F_c = nQ\delta, \quad (2.46)$$

$$P_c = l \times F_c, \quad (2.47)$$

where n is the unit vector connecting two centers of spheres in the direction of the sphere whose force is calculated, Q is the elastic collision constant, which is effectively a numeric penalty multiplier for overlapping of objects and δ is the overlap distance between two spheres as shown on Figure 2.10.

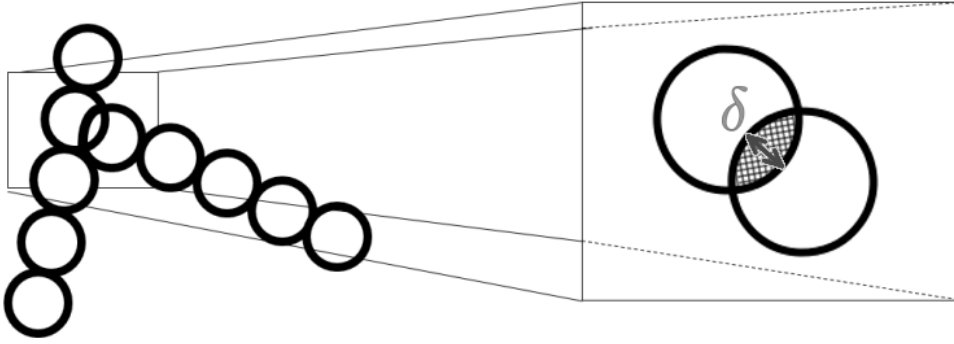


Figure 2.10: Schematic representation of elastic collision force.

Taking all of these factors into account the overall equation for force and torque balance are represented in eqs. (2.48) and (2.49)

$$0 = F_h + F_s + F_b + F_{int} \quad (2.48)$$

$$0 = P_h + P_b + P_{int} - k\omega \quad (2.49)$$

For interaction implementation the coefficient Q from eq. (2.46) is determined. As Q increased the time step is decreased hence it is needed to find the lowest coefficient Q possible. It was determined that Q could be reduced to a value of 100 kg/s^2 without affecting the quality of results.

By knowing the distance between any two spheres it is possible to introduce additional interaction models such as lubrication forces eq. (1.31).

2.5 Tolerance

Finally before running the overall model, error tolerance of the model has to be determined. In order to determine the appropriate tolerance of the ODE15s solver used to solve the described model for a simple shear flow field the following tests were performed. First the Young's modulus was set to a high value that would

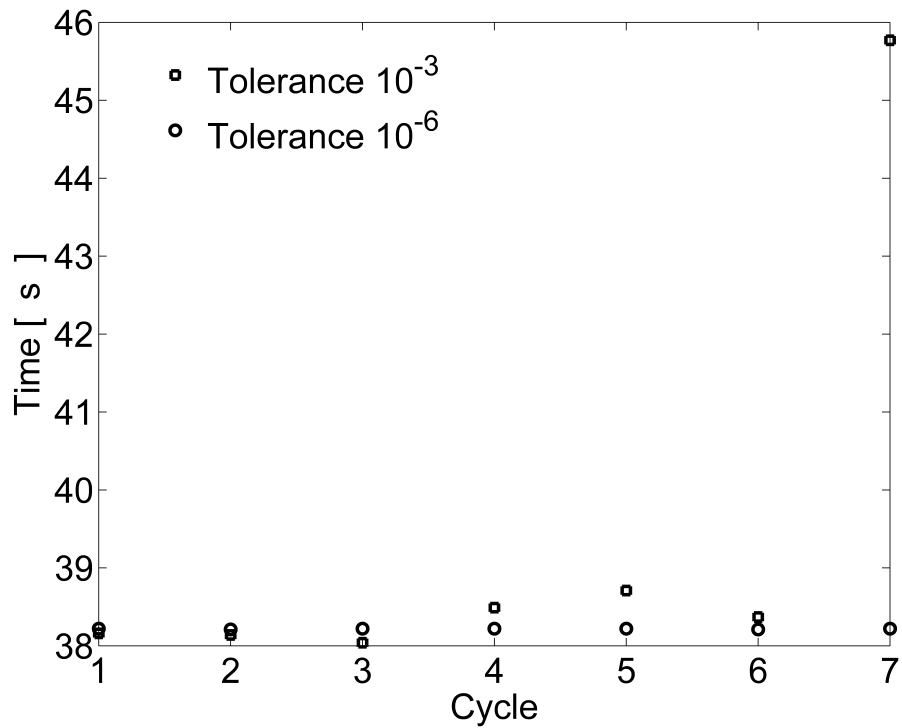


Figure 2.11: Cycle times of rigid fiber of axis ratio of 40 solved for two different tolerances.

guarantee rigid behaviour, then simulation was run and cycle time was measured for sequential cycles. This was done for different tolerance values until a tolerance that gave stable cycle time was found. Then Young's modulus was set to flexibility limit a fiber shapes were observed. In the case that the resulting fiber shapes are not symmetrical tolerance has to be further decreased. Results of one of such methods are presented in Figure 2.11. In Figure 2.11 a rigid fiber with axis ratio of 40 was simulated with multiple rotation cycles in two simulations with different tolerances. It could be seen that while for tolerance of 10^{-6} the cycle time is constant, it fluctuates for the tolerance of 10^{-3} . In order to achieve symmetric results for the flexible fiber case in the simple shear field ($\dot{\gamma} = 4s^{-1}$) the tolerance should be even further reduced to 10^{-10} .

2.6 Summary

As could be seen through Chapter 2 multiple parameters are needed to implement the model. Table 2.1-2.3 summarizes the parameter that are needed for the model.

In addition to the parameters described Table 2.1-2.3 additional parameters may be required in order to calculate the flow field, for example if the fiber is simulated in a simple shear flow, shear rate has to be provided.

Property	Symbol	Unit	Comment
Cylinder diameter	d	m	Diameter of the fiber
Cylinder length	l	m	Length of the fiber
Young's modulus	E	Pa	Young's modulus of the fiber
Viscosity	μ	$Pa \cdot s$	Viscosity of the polymeric matrix

Table 2.1: Physical properties in the system

Property	Symbol	Unit	Comment
Major axis friction coefficient	A_1	$N \cdot m \cdot s$	Calculated by fitting the results to Jeffery's model
Minor axis friction coefficient	A_2	$N \cdot m \cdot s$	Calculated by fitting the results to Jeffery's model
Elongation constant	k_s	N/m	Calculated through Young's modulus and fiber geometry
Bending constant	k_b	$N \cdot m$	Calculated through Young's modulus and fiber geometry

Table 2.2: Calculated properties in the system

Property	Symbol	Unit	Comment
Number of rigid segment	n	NA	Found by showing that larger number of segments doesn't change the results
Number of sphere in projection	B	NA	Found by showing that larger number of spheres doesn't change the results
Tolerance	ϵ	NA	Found by showing that lower tolerance doesn't change the results

Table 2.3: Model parameters in the system

Chapter 3

Simple Shear

In the current chapter the proposed model is applied and validated for the simple shear flow case. Simple shear is ideal for model application and validation for several reasons. First, simple shear flow could be regarded as 2D flow and since the proposed model is currently in a 2D form simple shear is a perfect engineering application for this model. Second, the literature contains many experimental and computational results for flexible fibers under the influence of a simple shear flow. Hence it is possible to compare the results of the proposed model to other results available in the literature.

3.1 Rotational Friction Coefficients

Note:The results of this section were obtained using Matlab2013 using ode15s solver.

By applying the proposed model to the case of fibers with $\lambda=1$, for various fiber lengths in various conditions and comparison to Jeffery's model a correlation to K_1 from eq. (2.12) was obtained. This correlation is presented in eq. (3.1):

$$K_1 = 0.25 \cdot \pi \cdot l^3 \cdot \mu, \quad (3.1)$$

where l is fiber length and μ is fluids viscosity.

The constants K_1 and K_2 from eq. (2.18) calculated by eq. (3.1) did not provide a good match between our model and Jeffery's model for finite aspect ratio cylinders. In order to calculate K_1 and K_2 constants of the rotational friction coefficients the following calibration procedure was performed in a simple shear flow environment:

- i. Length and diameter of the fiber are defined.
- ii. Length of the fiber is divided to designated number of rigid components.
- iii. Eq. (1.7) is solved for the geometry of rigid component using the equivalent axis ratio. Eq. (2.19) is solved for a rigid component. By fitting the solution of Eq. (2.19) to Eq. (1.7) rotational friction coefficients k are determined.
- iv. Young's modulus E is set to a high value. Eqs. (2.48) and (2.49) are solved for each rigid part with iterations for each step of time.
- v. Cycle time of rigid rod (high E) combined out of number of rigid components is compared to anticipated value from the solution of Jeffery's model Eq. (1.7) for equivalent axis ratio obtained from experimental data [34]. If match is not adequate, step iii is repeated. Thus in order to calculate the constants K_1 and K_2 simulation results are fitted to any two points of experimental results [34], which describe the actual cylinder axis ratio and its corresponding period of rotation for several axis ratio cylinders.
- vi. Once step v is completed, Young's modulus may be reduced so that flexible behavior could be achieved. Longer or shorter fibers could now also be constructed using rigid component obtained in step ii and friction coefficients obtained in steps iii-v.

K_1 and K_2 constants from eq. (2.18) for different geometries are summarized in Table 3.1. Results in Table 3.1 are presented for viscosity of $1000 \text{ Pa} \cdot \text{s}$, K_1 and K_2 are first order viscosity dependent. The coefficients that are presented in table 2 were calibrated to give cycle of rotation of approximately 54.8 ± 0.1 seconds for a combined rigid cylinder with axis ratio of 60.

Table 3.1: Friction coefficient parameters for several cylinder dimensions.

$l[m]$	$d[m]$	$A_1[N \cdot m \cdot s]$	$A_2[N \cdot m \cdot s]$
0.0012	0.0002	1.145E-06	1.15E-07
0.001	0.000166	6.63E-07	6.67E-08
0.001	0.0002	6.87E-07	8.49E-08
0.001	0.00025	7.12E-07	1.123E-07
0.0008	0.0002	3.65E-07	5.75E-08

3.2 Rigid Cylinder

The results of a simulation for a rigid cylinder constructed from one rigid component eq. (2.19) using the friction coefficient eq. (2.18) and its comparison to Jeffery's model eq. (1.7) are shown in Figures 3.1 and 3.2.

It could be seen from Figures 3.1 that for the case where $\lambda=1$ the model perfectly matches the solution of eq. (1.7). For the case where $\lambda \neq 1$ (Figure 3.2) the proposed model fits well to the solution of eq. (1.7) with a slight mismatch, due to representation of the cross section plane with two connected spheres at the center. All the results presented are obtained with viscosity of 1000 $Pa \cdot s$.

The model is designed for long fibers hence it has a lower bound of axis ratio at which it could be used because of the assumption on the representation of the cross section

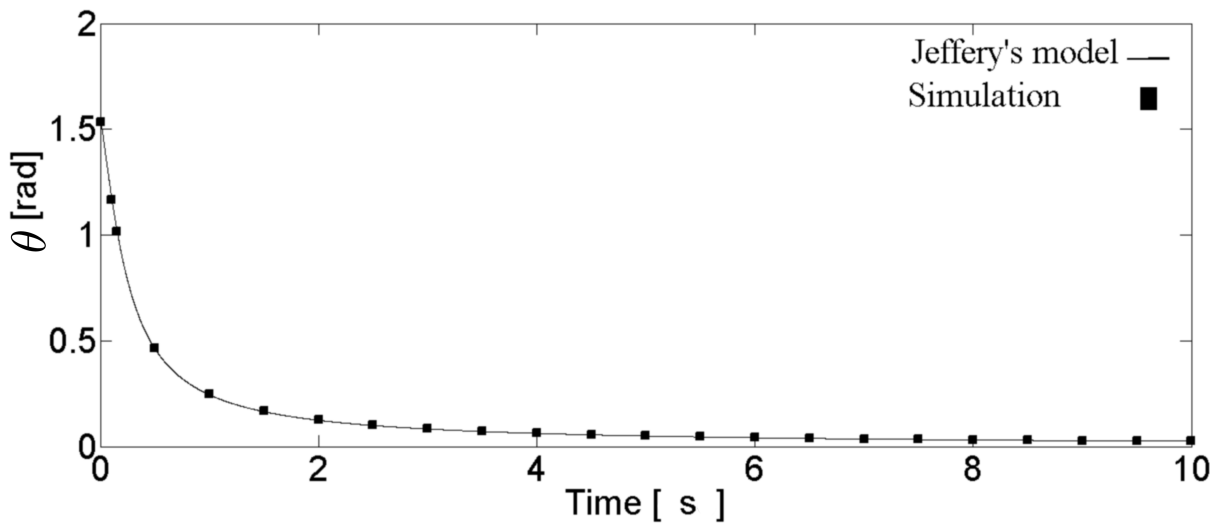


Figure 3.1: Comparison between simulation and Jeffery's model solution for the following conditions: $\frac{l}{d} = \infty$, $\dot{\gamma} = 4 \frac{1}{s}$, $l = 0.001$.

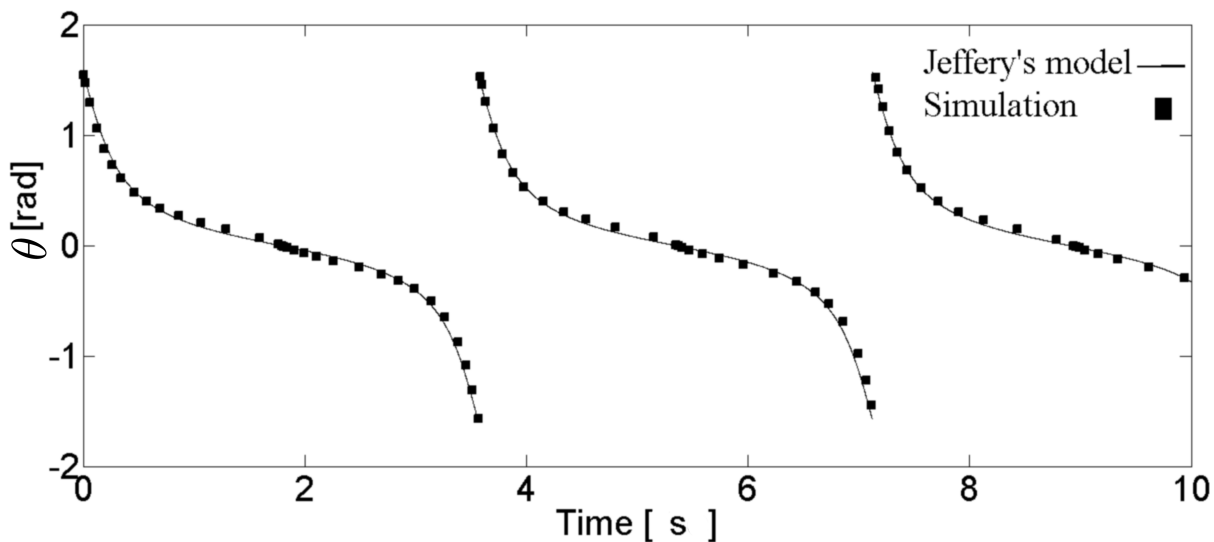


Figure 3.2: Comparison between simulation and Jeffery's model solution for the following conditions: $\frac{l}{a} = 5$ (4.3 equivalent), $\dot{\gamma} = 4 \frac{1}{s}$, $l = 0.001m$.

area. This model showed poor correlation to Jeffery's model for rigid cylinders with axis ratio below four.

Additional simulations were conducted to prove that rotational friction coefficient k from eq. (2.19) is independent of the flow field type and flow field parameters such as shear rate and only affected by orientation, geometry and viscosity. Figure 3.3 presents the comparison between the simulation and Jeffery's model eq. (1.7)

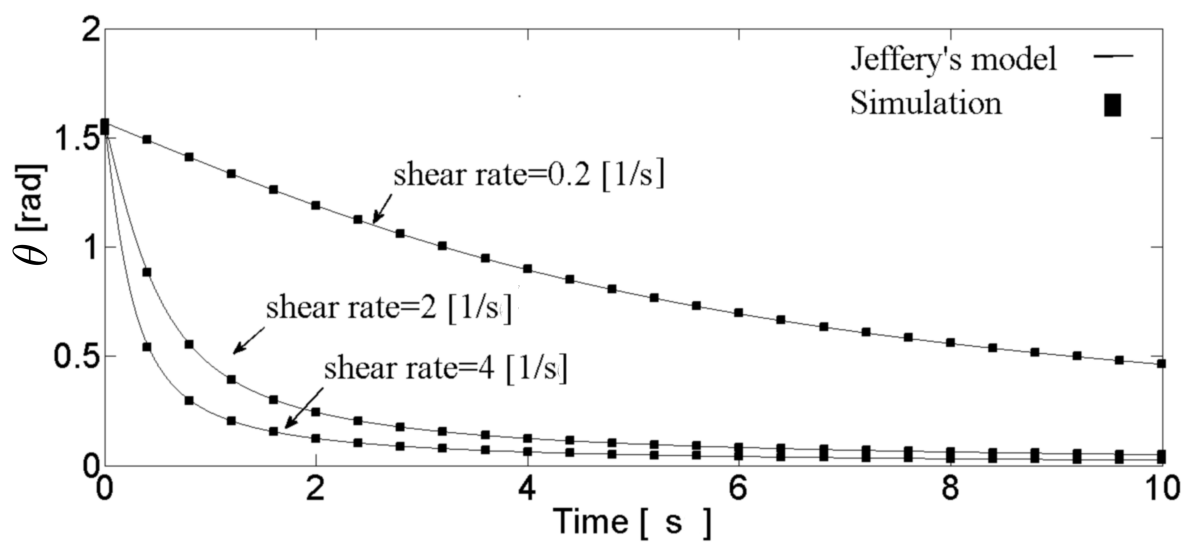


Figure 3.3: Friction coefficients as a function of shear rate.

solution for the same rod geometry (and same friction coefficients), but different flow conditions for the fiber with $\lambda=1$. Simulation results matched Jeffery's model results in all the tests. Hence it could be concluded that friction coefficients are independent of flow conditions. Since the friction coefficients are not affected by the flow conditions it is possible to use in any general flow case under the condition that it does not violate non-inertial flow assumption.

The long rigid fiber was modelled by combining several rigid cylinders (1-20 rigid cylinders). By setting a high value of Young's modulus and subsequently high k_s and k_b long rigid fiber behavior is achieved. Jeffery's model was developed for ellipsoids; however, it can be used for cylinders as long as the equivalent axis ratio of ellipsoid $A.Re$ is used to represent the axis ratio of a cylinder $A.Rc$. The results of the simulated equivalent axis ratio were compared with experimental data [34] in Figure 3.4 and were found to give a good approximation.

For a single rigid part simulation with friction coefficients from Table 3.1, cycle time and consequently equivalent axis ratio matches perfectly to cycle time obtained from Jeffery's model eq. (1.7) (Figure 3.2). The comparison between the cycle time of a fiber combined out of several rigid parts (Figure 3.4) with these coefficients shows

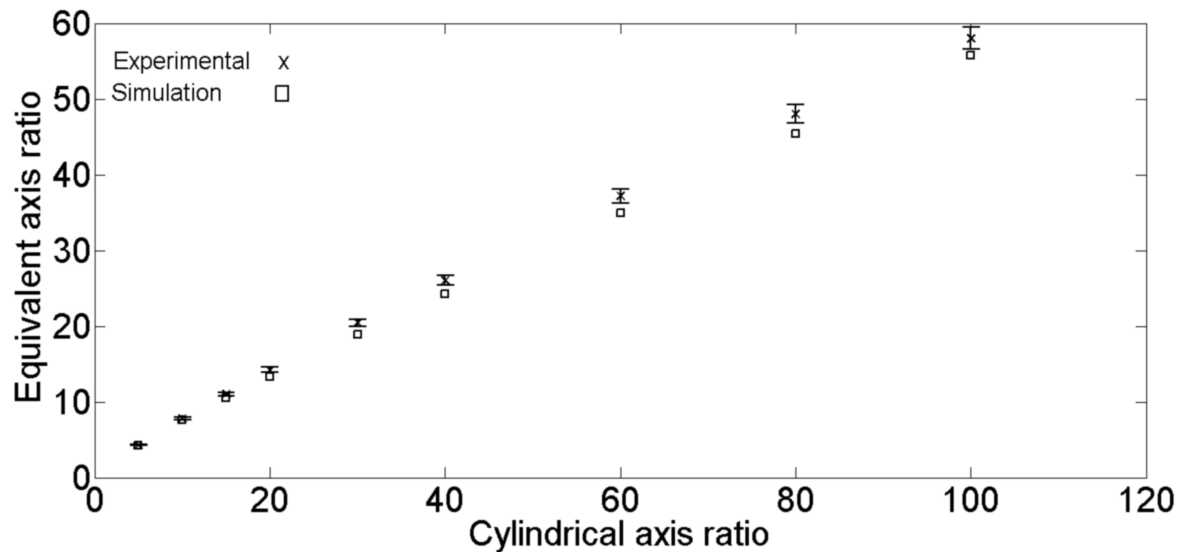


Figure 3.4: Comparison between simulation and experimental [34] periods of rotation of a rigid fiber as a function of aspect ratio.

slight deviation from the experimental value. This is because the friction coefficients are fitted to match cycle time obtained from Jeffery’s model and a simulation for a single rigid rod, while the results for fibers constructed out of several rigid segments are calculated using the friction coefficients that were obtained in Table 2.1 using the calibration with any two points from Figure 3.4.

3.3 Flexible Fiber

In the simple shear flow field, a flexible fiber with initial position perpendicular to the flow direction is expected to first rotate rigidly for $\pi/2$ until it lies horizontally then it will start to bend into a “S” form and rotate. In each cycle the “S” form will open back into horizontal line and then start to bend again. This behaviour is described both in experimental [31,63] as well as in theoretical [65,67,68,107] works. Flexible long fiber was simulated by combining cylinders (16 cylinders in Figure 3.5) with cylinder axis ratio of five (5) and varying Young’s modulus. These simulations were conducted with a shear rate of $4s^{-1}$. Note that the snapshots of fiber shapes in Figure 3.5 are not given at equal time intervals between fiber shapes as well as that the time intervals are different between shapes from different Young’s modulus cases.

The results match well to previous work. One can also notice that the cycle time is increasing as the fiber becomes more rigid as described in the literature [65]. In order to measure the critical Young’s modulus value after which the fiber will start to bend. A $\Delta\theta$ parameter was introduced, according to eq. (3.2), and graphically shown in Figure 3.6.

$$\Delta\theta = \theta_1 - \theta_n, \tag{3.2}$$

where θ_1 is the orientation of the central rigid part and θ_n is the orientation of the rigid part from the end of the fiber.

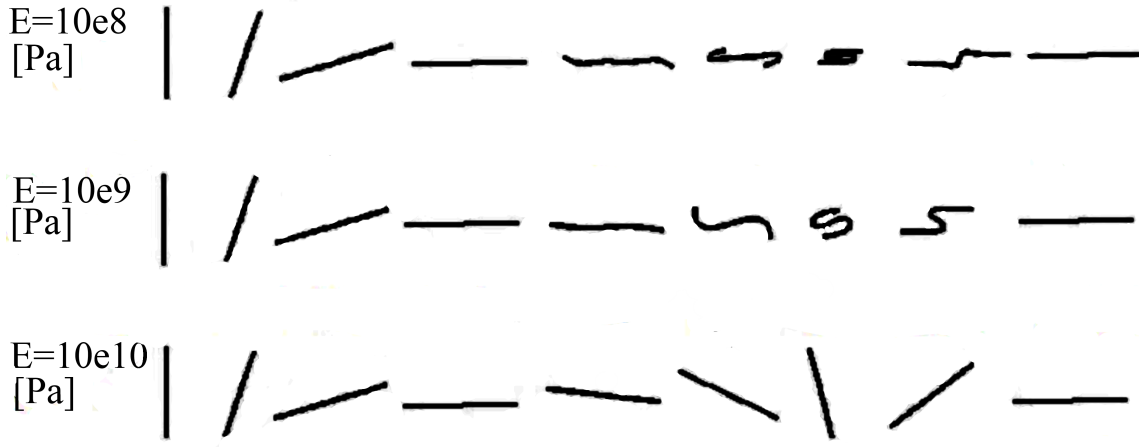


Figure 3.5: Flexible fiber transition states through rotation in a simple shear flow $\dot{\gamma} = 4\frac{1}{s}$. The flow is from left to right.

As it could be seen from Figures 3.7 $\Delta\theta$ is decreased to approximately $-\pi$ which could be also confirmed by Figure 3.5. Figure 3.8 presents $\Delta\theta$ for the rigid case in Figure 3.5. In this case it was expected to get $\Delta\theta = 0$ for all time steps since the fiber is rigid. The results, however, show some level of flexibility which is due the nature of the model and numerical error. Due to this it is needed to set a threshold for $\Delta\theta$ beneath which the fiber will be considered rigid. From visual observation of the results this threshold was set to 0.02 ± 0.005 radian. Note that the x axis on Figures 3.7 and 3.8 are time step increment and not actual time with the time step size through the simulation is changing as the solver is picking the maximum size step that would still maintain a stable solution.

Flexible fibers with various $A.Rc$ were constructed out of cylinders with $A.Rc$ of 5 and various Young's modulus values were simulated. A critical Young's modulus values, at which bending begins, was obtained. These values were compared with theoretical values obtained from eq. (3.3) [31]:

$$\frac{\mu\dot{\gamma}}{E_b} = \frac{\ln(2A.Rc) - 1.75}{2A.Rc^4}, \quad (3.3)$$

where $A.Rc$ is major axis length divided by minor axis length or in our case just

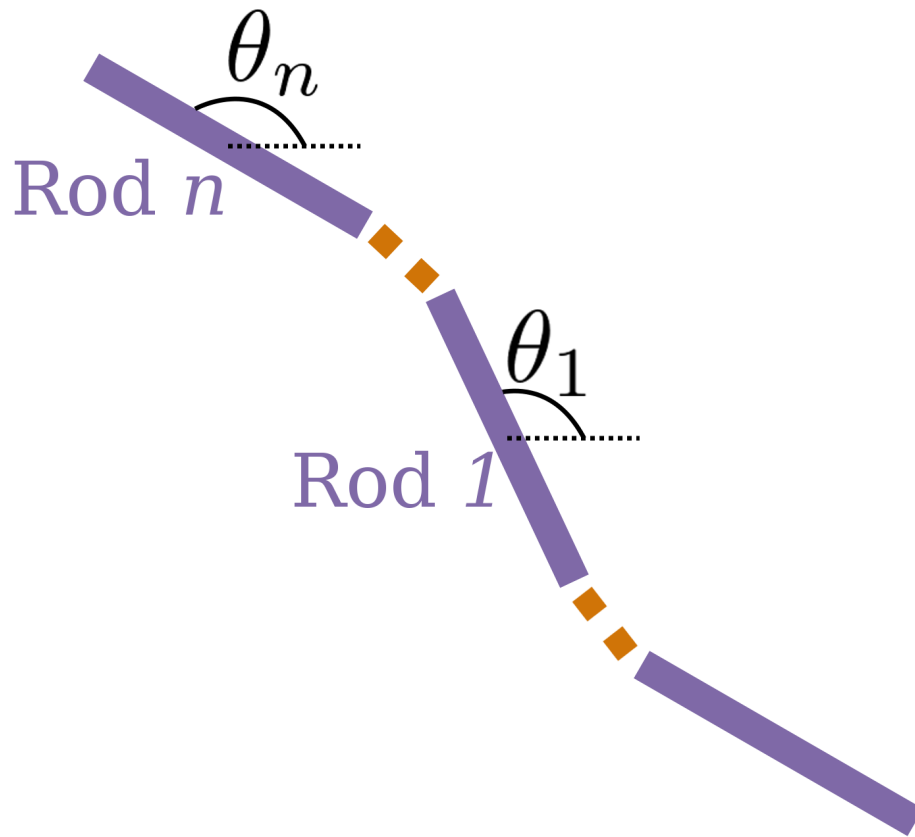


Figure 3.6: Graphical representation of bending parameter.

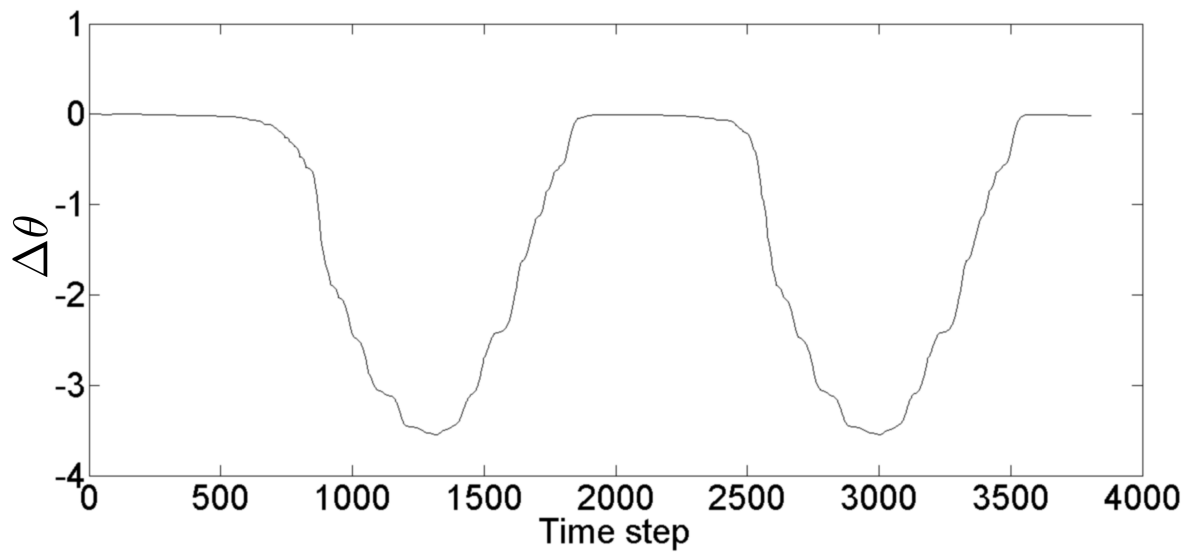


Figure 3.7: $\Delta\theta$ calculations for the $E = 10^9 Pa$ case from Figure 3.5.

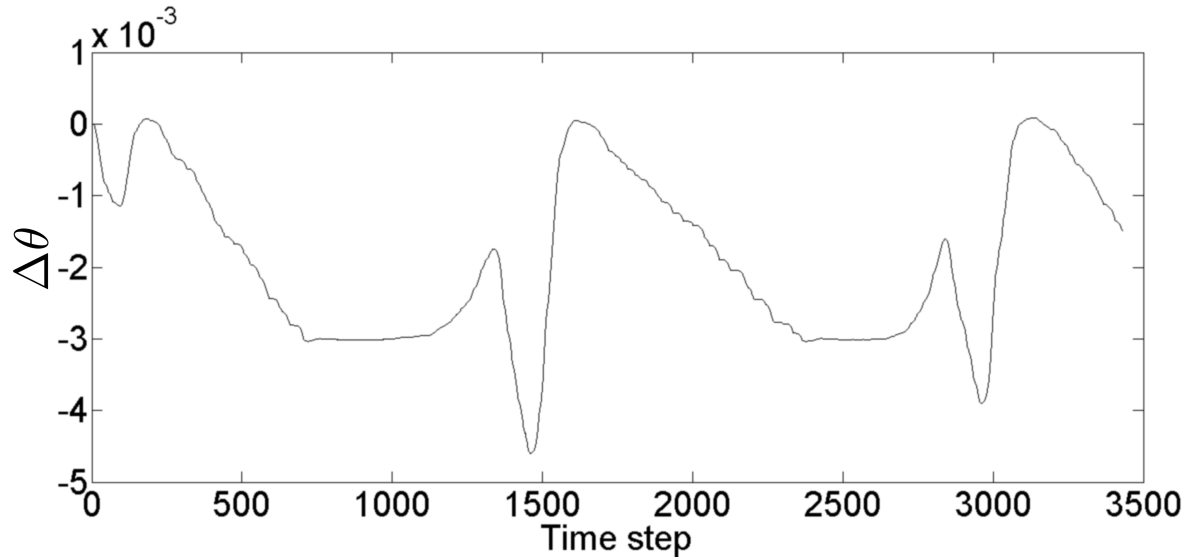


Figure 3.8: $\Delta\theta$ calculations for the $E = 10^{10} Pa$ case from Figure 3.5.

l/d of the fiber, E_b is bending modulus, which is approximately twice the value of Young's modulus E , μ is matrix viscosity and $\dot{\gamma}$ is shear rate [108]. The simulation results match theoretical results closely if equivalent axis ratio is used to calculate the theoretical value in eq. (3.3).

In order to investigate the effect of number of segments representing a flexible fiber on the results, a fiber of 12 mm length and 0.2 mm diameter was divided into segments of axis ratio 6,5 and 4. The resulting fibers were composed of 10, 12 and 15 segments respectively. In addition, fiber length of 24 mm and 0.2 mm diameter was divided into segments of the same axis ratio as previous, which resulted in fibers composed of 20,24 and 30 parts. These fibers were simulated with various values of Young's modulus ($10^8 - 10^9 Pa$). Fibers combined of segments with smaller axis ratio produced smoother shapes. This result depended on the axis ratio of the components, but not on the number of components. The differences between fibers composed from axis ratio segments decreased as Young's modulus increased. This behaviour could be observed in Figures 3.10 and 3.11. Figure 3.11 shows that although fibers composed out of axis ratio elements of $l/d = 4$ and $l/d = 6$ give very similar results at higher Young's modulus a fiber composed out of elements with Young's modulus of $l/d = 5$ gives a very different result, we believe that this is a result of numerical error.

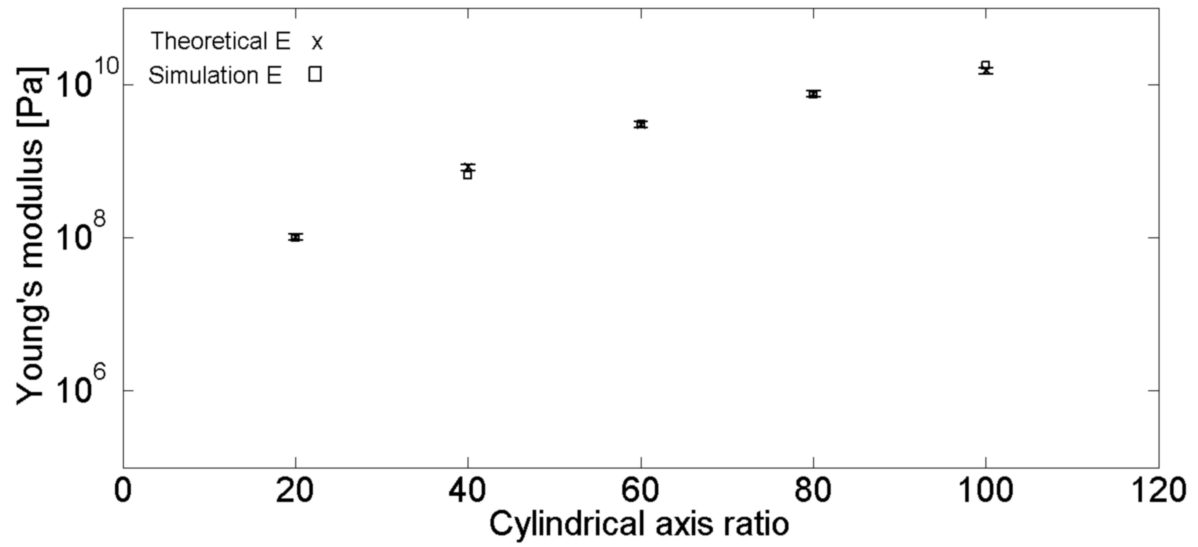


Figure 3.9: Comparison between theoretical [31] and simulated values for critical Young modulus values for buckling.

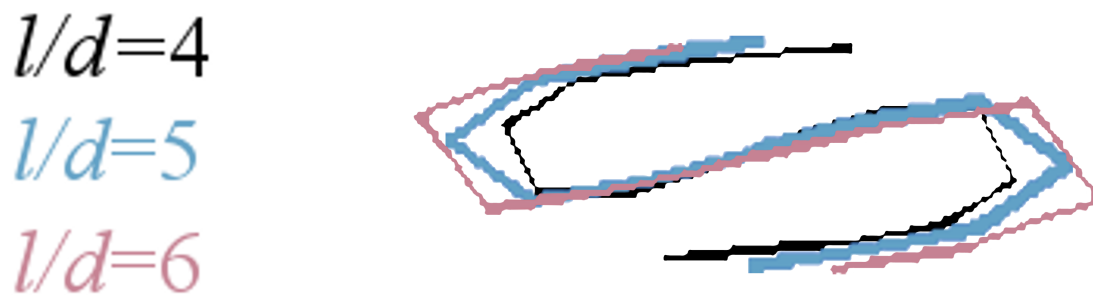


Figure 3.10: 12 mm fiber made out of rigid parts with axis ratio of 4,5 and 6 with Young's modulus of $10^8 Pa$ at shear rate of $4s^{-1}$.

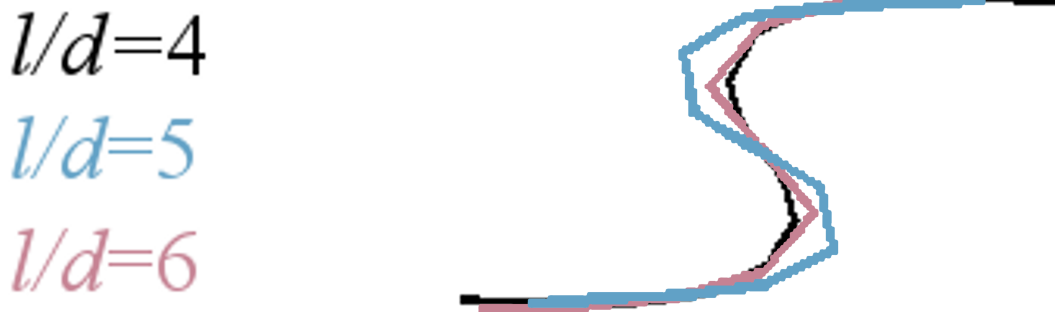


Figure 3.11: 12 mm fiber made out of rigid parts with axis ratio of 4,5 and 6 with Young's modulus of $10^9 Pa$ at shear rate of $4s^{-1}$.

3.4 Calculation time

Table 3.2 summarizes the time taken to simulate various fibers in the period of 100 s under a shear rate of $4s^{-1}$. The simulations were done on a computer with eight inter Xeon 2.4 GHz processors. Although the qualitative results could be interpreted the quantitative results in this table can change due to code optimisation or fiber initial position (position on the y axis). The initial position in simple shear flow does not change the calculation results (since the calculation is always symmetric to the center of the fiber). Calculation time will change, since the higher the fiber is located on the y axis the higher its linear velocity which will result in higher calculation time. For a single segment fiber, fiber with lower length to diameter ratio takes more simulation time since it has to make more rotation periods in a given time. It could be seen that increasing the number of segments increases the simulation time. Increasing Young's modulus also increases the simulation time dramatically. As Young's modulus increases the fiber becomes more stiff, for the same Young's modulus shorter fiber will be more stiff than longer fiber hence for the case where both fibers could already be treated as rigid a shorter fiber would take longer time to simulate.

axis ratio of rigid component	Number of components	Young's modulus [Pa]	Number of simulation steps	Simulation time [s]
4	1	-	5105	152
5	1	-	4530	132
6	1	-	4202	126
5	12	10^7	6245	1683
5	12	10^9	4417	3022
5	12	10^{11}	47061	86136
5	16	10^7	6559	2264
5	16	10^9	5087	4701
5	16	10^{11}	29634	72500

Table 3.2: Number of simulation steps and simulation time for various fibers simulations (initial position of fiber's center of mass was at [0.8, 0.8])

Chapter 4

Squeeze Flow

In order to study fiber orientation in a compression molding flow, it is important to find a reliable compression molding solver. In order to simplify the calculations, compression molding flow is approximated by a rheometric squeeze flow.

In the present chapter, dynamics of a rigid fiber in a rheometric squeeze flow will be studied as well as long flexible fiber orientation and deformation will be solved in two systems Table 4.1 of rheometric squeeze flow using the solution by Gupta [102]. The first system (System A) results are shown in Figure 4.1-Figure 4.16 and it is for the case of $c = a_0 \ll l_f$, where a_0 is the initial distance between the center of the mold and the plate, c is half the plate length and l_f is fiber's length, in this system the size of the fiber is significantly smaller than the size of the compression axis. Second system (System B) results are shown in Figure 4.17-Figure 4.20 and it is for the case of $c > a_0 > l_f$ in this system the size of the fiber is comparable to the size of the compression axis. The parameters chosen for both systems are presented in Table 4.1.

The solution by Gupta [102] does not make simplifying assumptions, such as neglecting the time derivatives and assuming $\frac{\partial v_x}{\partial x} \ll \frac{\partial v_x}{\partial y}$. Hence it is possible to compare a real case system where these assumptions are true (system B) to the extreme case (system A) where these assumption no longer hold and see the full effect of rheometric squeeze flow on a long flexible fiber. Such a comparison allows study of all the

effects in the system. In addition both systems have to be large enough to neglect wall effects as they are not included in the model. According to eqs. (1.48), (1.49), (1.50) the velocity of the fluid in the y direction is proportional to $1/a$ while the velocity in the x direction is independent of a . Hence by reducing the gap between the plates in system B compared to system A but leaving the length of the plates the same in both systems equal dimensionless velocity between two systems is achieved. Therefore a fiber starting at the same dimensionless coordinates $(x/c, y/a)$ in both systems, at time t would be found in the same dimensionless coordinates in both systems thus allowing a comparison.

Flexible fiber orientation in a squeeze flow field was obtained using Gupta [102] solution for a rheometric squeeze flow system which is described in Figure 1.10 for system A. According to Gupta [102] analytical solution to rheometric squeeze flow problem exists for the case where the distance between the system's horizontal center line and the upper wall could be represented through eq. (1.47). Upper plate velocity (for system A) as a function of time is shown in Figure 4.1 and its location (for system A) as a function of time is shown in Figure 4.2. Velocity values as a function of time were obtained by calculating a derivative of eq. (1.47) with respect to time, the resulting expression is given in eq. (4.1).

$$V_w = 0.5M (a_o^2 + Mt)^{-0.5} \quad (4.1)$$

Gupta's rheometric squeeze flow is given by eqs. (1.49) and (1.50). The solution for the upper left rectangle marked in Figure 1.10 is represented in Figure 4.3.

Shear rate, $\dot{\gamma}$, which is effectively the scalar value of the deformation tensor D can

Table 4.1: System's A and B parameters.

Parameters	System A	System B
a_0/c	1	0.1
c m	1	1
R	0.05	0.0005
μ Pa·s	1000	1000
ρ kg/m ³	1000	1000

be calculated for a general flow through eq. (4.2) [109,110]

$$\dot{\gamma} = \sqrt{2\bar{D} : \bar{D}} \quad (4.2)$$

The proposed model [111] was run on MATLAB 2014a Using Linux system machines provided by SHARCNET. The differential equations were solved using ode23tb solver. The tolerance for all the simulations was set to 10^{-10} .

The vorticity tensor is calculated for v_x and v_y separately in order to evaluate which direction of rotation will be preferred by flow from each direction.

$$\sigma_y = 0.5 \cdot \begin{pmatrix} 0 & 0 \\ 0 & \frac{dv_y}{dy} - \frac{dv_y}{dy} \end{pmatrix} = 0, \quad (4.3)$$

$$\sigma_x = 0.5 \cdot \begin{pmatrix} 0 & \frac{dv_x}{dy} \\ -\frac{dv_x}{dy} & 0 \end{pmatrix}. \quad (4.4)$$

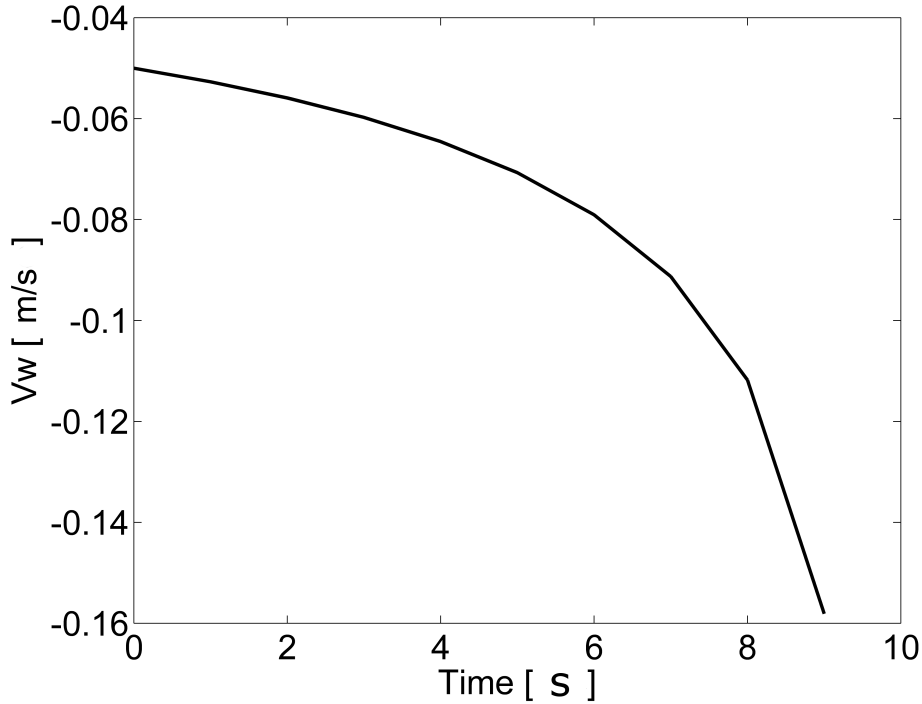


Figure 4.1: Upper plate velocity as a function of time.

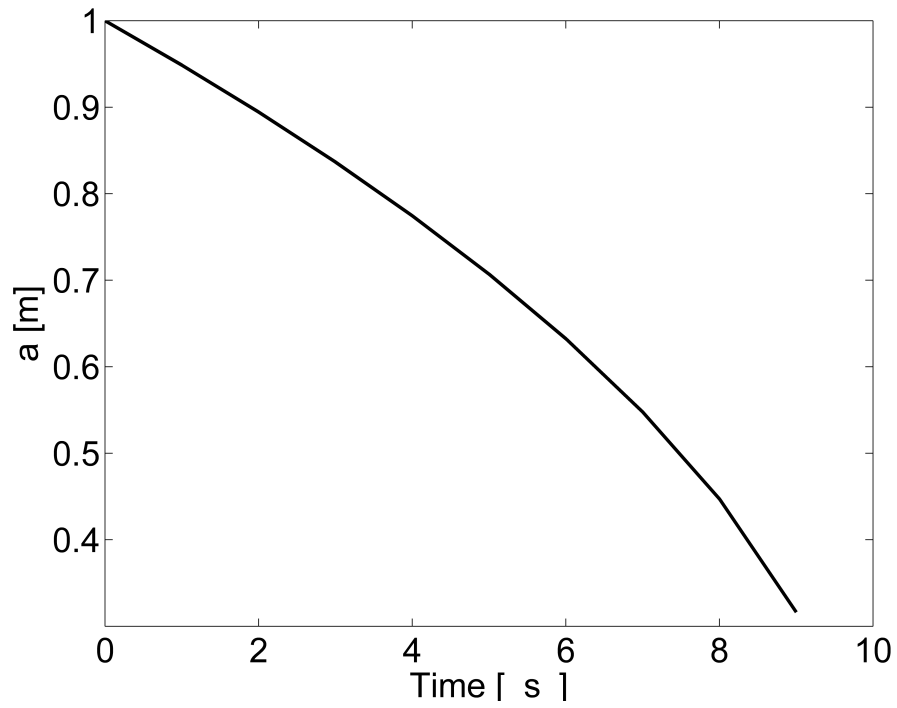


Figure 4.2: Upper plate location as a function of time.

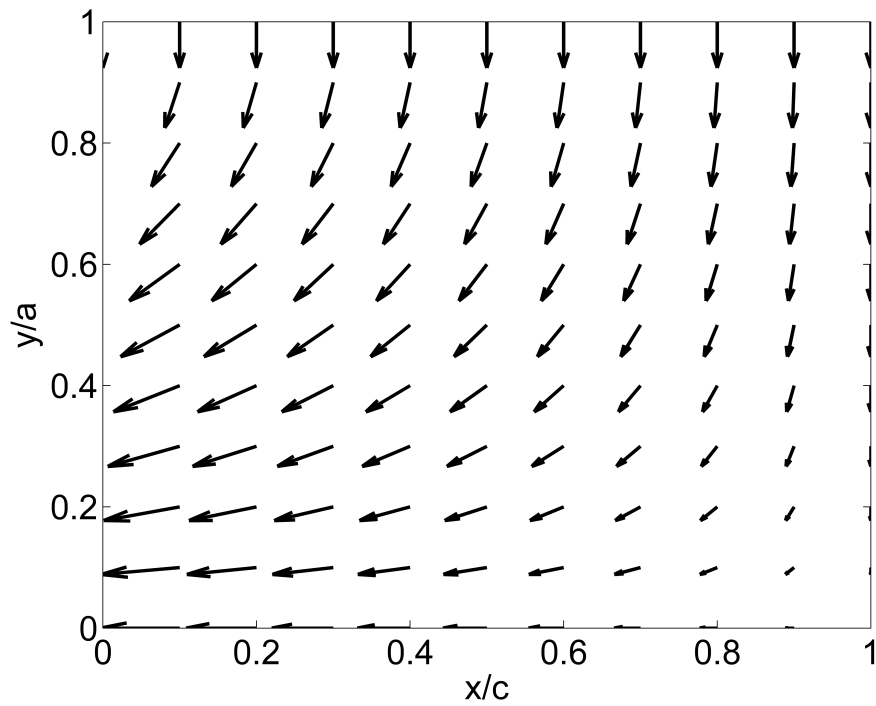


Figure 4.3: Solution of a squeeze flow system (for system A).

It can be seen from eq. (4.3) and (4.4) that the vorticity tensor for v_y is zero and thus it will not generate rotation and hence the velocity from y direction will contribute to orientation only by forcing the rod into an equilibrium position, which is horizontal (vertical position is an unstable equilibrium position), dv_x/dy is negative in this quarter of the solution and thus vorticity tensor for v_x will generate negative radial velocity.

4.1 Rigid Fiber

Squeeze flow presented in Figure 4.3 was investigated with respect to Jeffery's model [16]. Rigid fiber orientation depends on the fiber's initial position and axis ratio (A.R). Figure 4.4 shows that as the ratio of length to diameter of the fiber decreases, its angular velocity (at least initially) decreases. This is due to the fact that according to initial vertical position the length of the fiber is forced into rotation by the x component of the velocity, v_x , but on the other hand slowed by y component of the velocity, v_y acting on the cross section of the fiber, since the cross section of the fiber is in an equilibrium position with respect to v_y . Figure 4.5 shows that the trajectory of orientation will depend on the initial position of the fiber.

Solution of Jeffery's model in a squeeze flow field presented in Figure 4.3 was compared with the solution of the proposed model. For $\lambda = 1, 4.6$, the model perfectly matches the solution of Jeffery's model. These results are additional proof that rotational friction coefficients previously obtained in simple shear flow are independent of flow conditions. In addition these results validate the proposed model for a squeeze flow case. For $\lambda \neq 1$, Figure 4.7, the proposed model fits well to the solution of Jeffery's model with slight mismatch (maximum of 5% at some points), this is due to several base assumptions of the model: the effects of cylinder length and its diameter on hydrodynamic torque are decoupled and the effect of cylinder diameter on the hydrodynamic torque is represented through two connected spheres located at the center of the cylinder and perpendicular to its length [111].

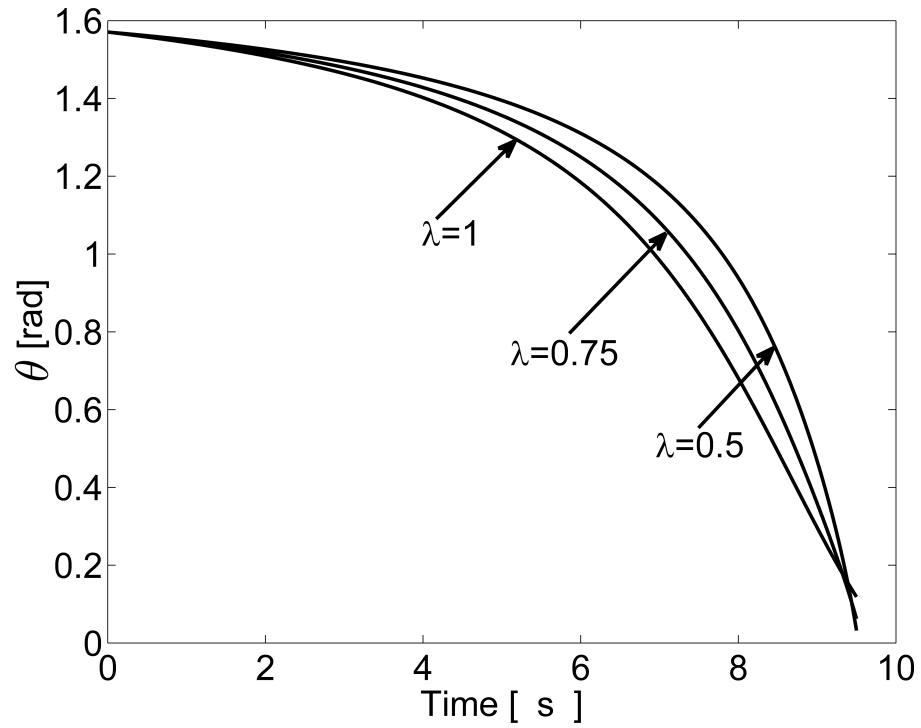


Figure 4.4: Solution of Jeffery's model for a fiber of different axis ratio, λ , under squeeze flow. Fiber initial coordinates are $(x_o, y_o) = (0.8, 0.8)$.

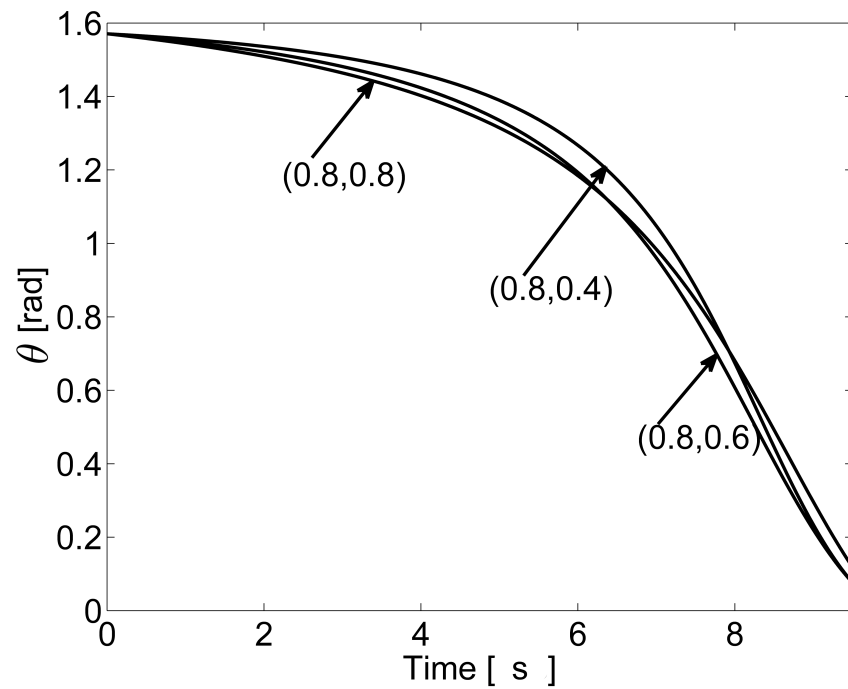


Figure 4.5: Solution of Jeffery's model for a fiber at different initial coordinates for $\lambda = 1$.

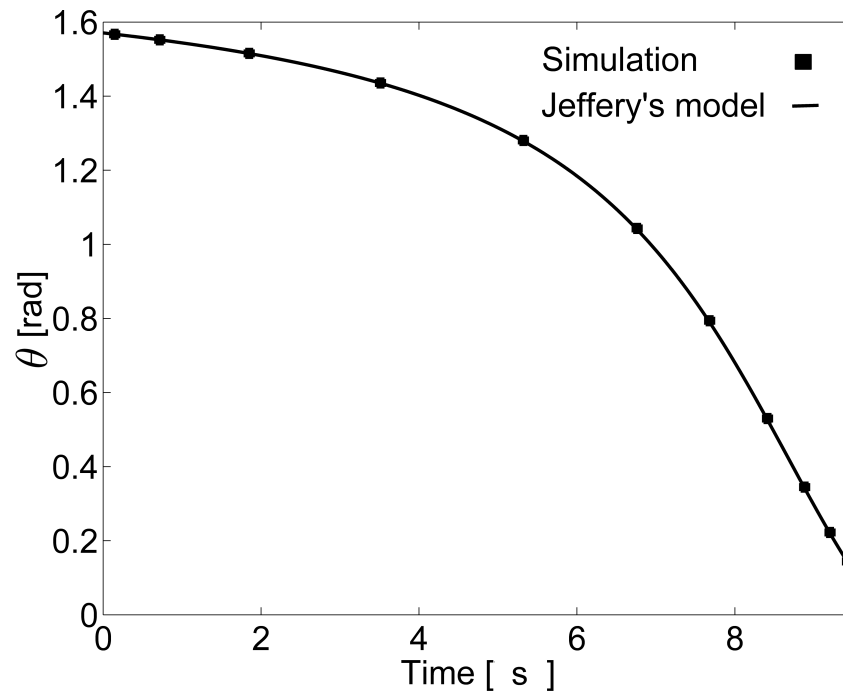


Figure 4.6: Comparison between simulation and Jeffery's model solution for: $\frac{l}{a} = \infty$, $l = 1mm$.

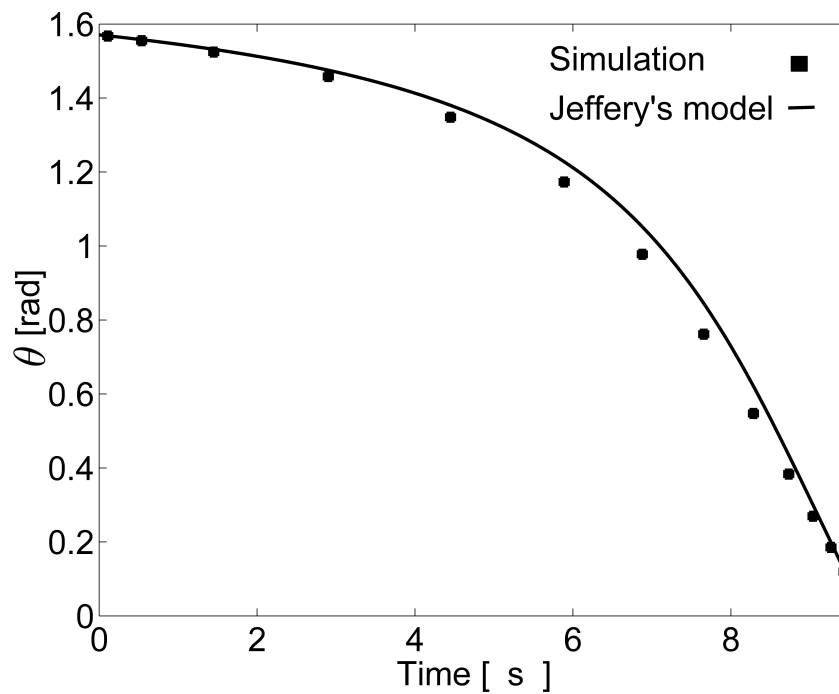


Figure 4.7: Comparison between simulation and Jeffery's model solution for: $\frac{l}{a} = 5$, $l = 1mm$.

4.2 Flexible Fiber

Fiber orientation and deformation in squeeze flow for three values of Young's modulus $10^7, 10^8$ and $10^9 Pa$ were simulated for systems A and B. Fiber length was set to $16mm$, combined from 16 segments with each rigid segment having an axis ratio of 5. Fiber was placed in vertical position ($\theta_o = 0.5\pi$) with its center mass at different initial positions: $(x/c, y/a_0) = (0.8, 0.8), (0.8, 0.4), (0.8, 0)$ one more initial position was tested for each system $(x/c, y/a_0) = (0.8, 0.003)$ for system A and $(x/c, y/a_0) = (0.8, 0.03)$ for system B. Where the line $(1, y)$ represents the vertical mid-line of the mold, the line $(x, 1)$ represents the upper wall of the mold and the line $(x, 0)$ represents the horizontal center of the mold. Note that the last position dimensionless coordinates differ from each other but the absolute coordinates are the same $(x, y) = (0.8, 0.003)$. As previously mentioned systems A and B are selected in such a manner that at time t , fiber will be located at the same dimensionless position $(x/c, y/a)$. Figures 4.8 presents the path that fiber's center of mass from Figures 4.9-4.15 (system A) and Figures 4.17-4.20 (system B) takes. Each point in Figure 4.8 represents the position of the center mass of the fiber at the following times: 0, 2.37, 5.54, 8.13 and 8.8 seconds. Snapshots of fiber shapes were also taken at these times and plotted in order to see the evolution of fiber orientation and deformation in this process, and these results are shown in Figures 4.9-4.15 (system A) and Figures 4.17-4.20 (system B).

System A

Figure 4.9 and Figure 4.10 show that when the fiber is placed above the $(x, 0)$ line it will orient itself in the direction of the elongation flow which exists in the center between two plates. If the fiber is not rigid enough the fiber will go through a transition stage in which it will get distorted before it will get straightened and lie horizontally. As the fiber is placed closer to the $(x, 0)$ line (Figure 4.10) the Young's modulus that was previously sufficient to keep the fiber straight is no longer sufficient, due to the fact that shear rate is increasing with the decreasing distance

to the middle.

Phelps et. al. [112] investigated fiber breakage in LFT materials prepared by injection molding and found that it was due to bending and elongation. In their work they developed a fiber breakage prediction model and compared experimental and computational fiber distribution lengths. It could be seen from Figure 4.9 C that once the fiber is close to the horizontal position its segments start to separate. This happens due to velocity gradient in the x direction, the elongation is induced due to the fact that front segments are faster than the back segments. Since current simulation does not include breakage, for a small enough Young's modulus the fiber will simply stretch although in reality if the fiber is brittle it will break, such results could also be observed in Figure 4.9 - Figure 4.20.

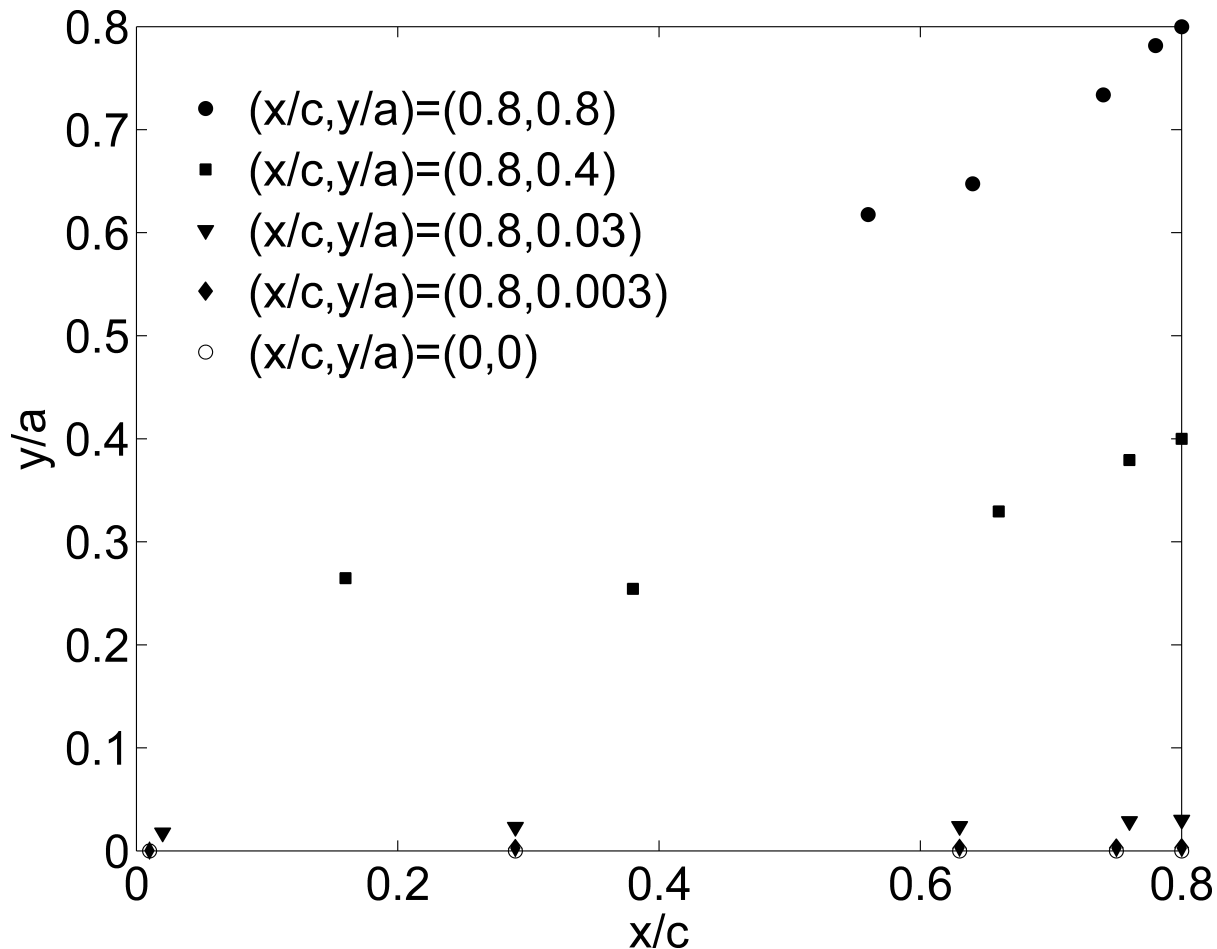


Figure 4.8: Path of fiber's center mass from Figures 4.9-4.20.

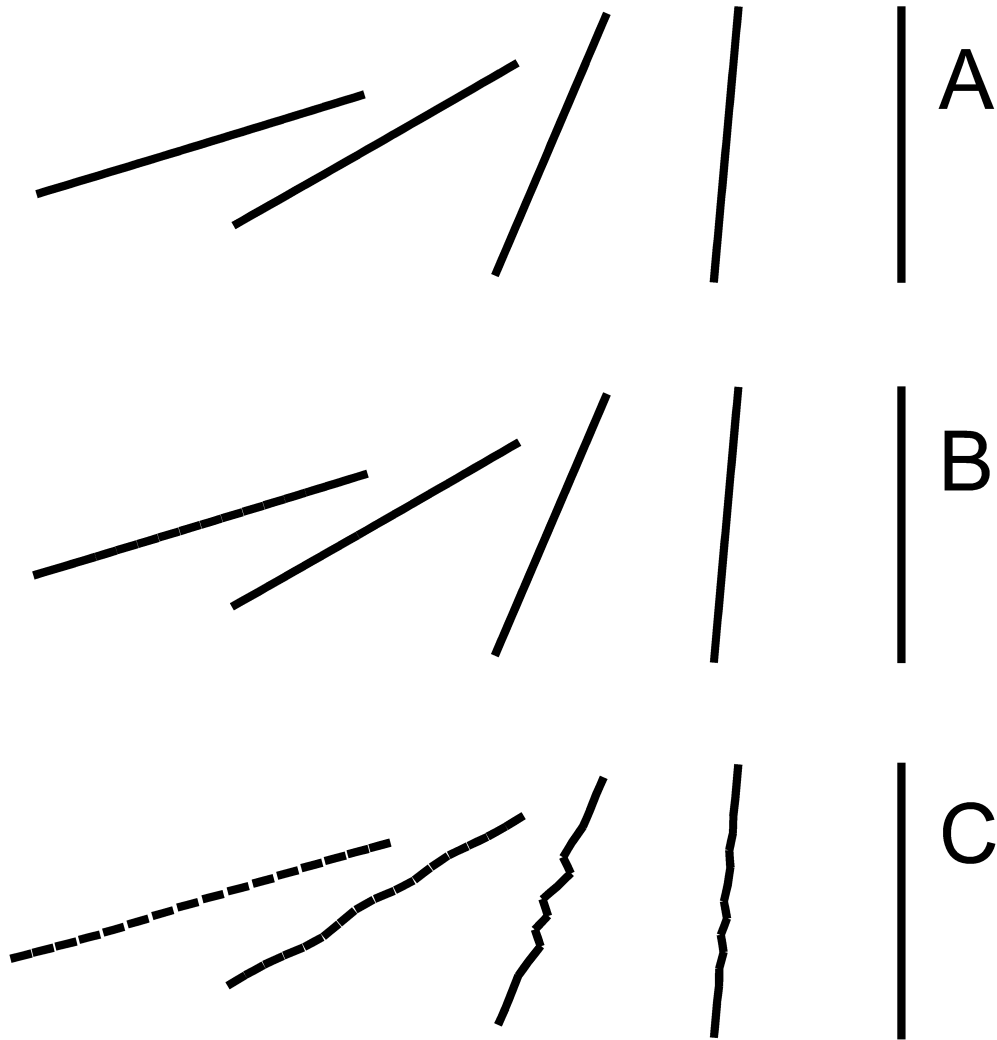


Figure 4.9: Fiber orientation and deformation in squeeze flow for three values of Young's modulus $A.10^9 Pa$, $B.10^8 Pa$ and $C.10^7 Pa$ for fiber placed at the initial position of $(x/c, y/a_0) = (0.8, 0.8)$ using coordinates of Figure 1.10. The fiber is presented at times: 0, 2.37, 5.54, 8.13 and 8.8 s.

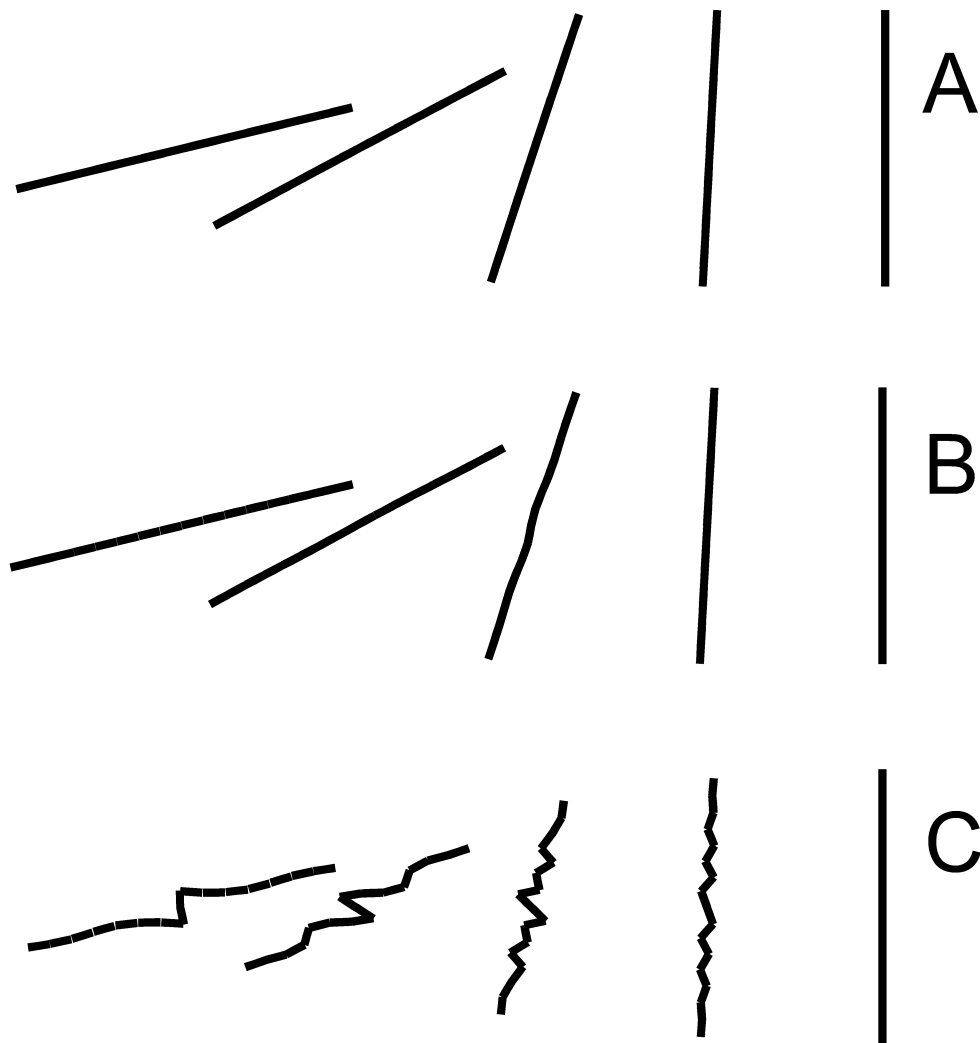


Figure 4.10: Fiber orientation and deformation in squeeze flow for three values of Young's modulus $A.10^9 Pa$, $B.10^8 Pa$ and $C.10^7 Pa$ for fiber placed at the initial position of $(x/c, y/a_0) = (0.8, 0.4)$ using coordinates of Figure 1.10. The fiber is presented at times: 0, 2.37, 5.54, 8.13 and 8.8 s.

It could also be noted that during fiber orientation in Figure 4.9 -4.15 very sharp angles between rigid segments could be observed. These effects do not necessarily suggest buckling and could simply be visual effects due to the nature of the model. In the proposed model flexible fiber continuity is achieved by connecting several rigid segments together with elastic springs. This method achieves fiber continuity but does not provide continuity in the derivative of the shape hence the obtained shapes are not always smooth. In some cases these effects could be mitigated by reducing the axis ratio of the constructed rigid segments. The proposed model is limited to rigid segments with axis ratio of 4 and above. Attempting to solve these cases with 20 segments with axis ratio of 4 did not change the results much and the sharp angles remained.

These results are not limited to low Young's modulus values. In a simple shear flow case fiber bending is governed by Weissenberg number (We) shown in eq. 4.5.

$$We = \frac{\mu\dot{\gamma}}{E} \quad (4.5)$$

Similarly in squeeze flow the same results could be obtained with higher Young's modulus values providing that the value of viscosity is increased by the same proportion, although unlike in simple shear flow case in squeeze flow kinematic viscosity has to remain the same in both cases since according the eq. (4.1) the flow field in rheometric squeeze flow will depend on kinematic viscosity unlike simple shear flow field which depends only on the shear rate. The relationship between viscosity and Young's modulus could be easily seen through model eq. (2.42). The numerator term P_h^j is first order viscosity dependent while the other two numerator terms P_e^j and P_b^j are first order Young's modulus dependent, the only denominator term k^j is first order viscosity dependent. Hence it could be seen that increasing both Young's modulus and viscosity by the same proportion will not influence the result. The analysis for the shear rate in squeeze flow is much more complicated since it changes in time and space. In addition, unlike in the simple shear flow case, the shear rate in squeeze flow is dictated by two velocity components hence the bending should

also be dependent on at least two parameters. This suggests that unlike in simple shear flow, bending in squeeze flow can not be analysed by We number, which depends only on one flow parameter the shear rate. The scalar value of shear rate in a rheometric squeeze flow is decreasing as the distance from horizontal center of the system is increased. Hence the shear rate that acts on the fiber in Figure 4.9 is lower than in the case solved in Figure 4.10. It could be seen that larger shear rate causes the fiber to exhibit less rigidity in Figure 4.10 than in Figure 4.9. The values of the shear rate could be seen from Figures 4.11-4.13.

In Figure 4.14 A and B relatively small angles could be observed between segments, such a high bending can cause breakage in brittle materials. Similar results could be seen also in Figures 4.15, 4.16, 4.19 and 4.20. As mentioned previously, breakage is not included in the current model, and thus no breakage occurs in the simulation and the fiber continues to deform.

In order to incorporate buckling breakage into the model a critical angle θ_c should be set. When the angle between two adjacent rigid segments goes below θ_c the fiber will break at the connection between the segments. A similar approach was used by Lee [113] with an experimental value of θ_c .

In another investigation the fiber was placed with its center mass at $(x, 0)$ line these results are presented at Figure 4.14. In this case the fiber will bend into an accordion

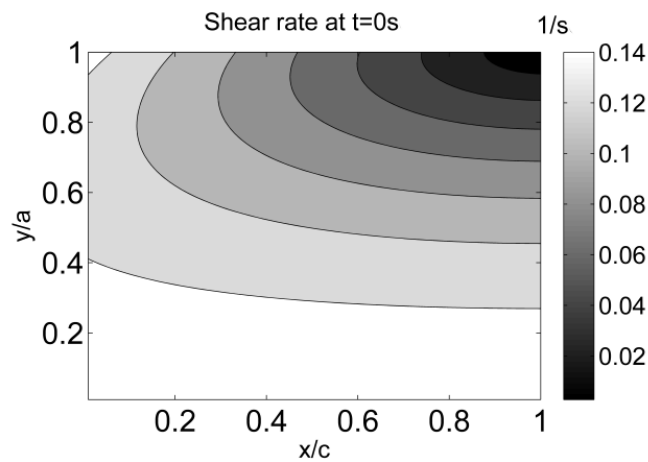
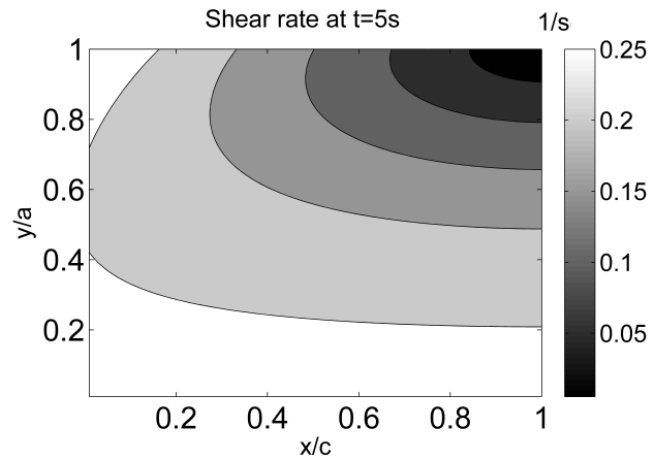
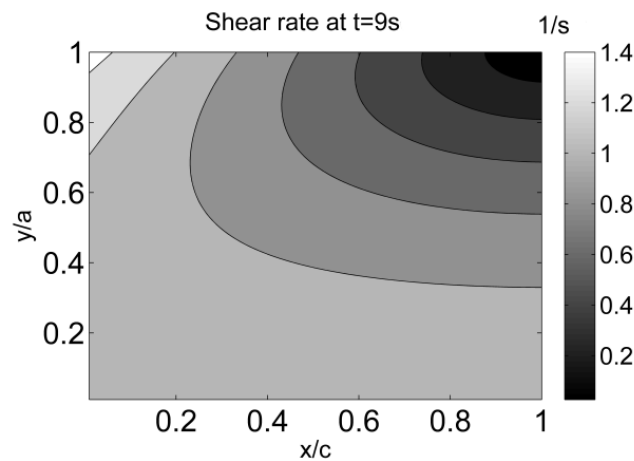


Figure 4.11: Shear rate in system A at time $t = 0$.

Figure 4.12: Shear rate in system A at time $t = 5$.Figure 4.13: Shear rate in system A at time $t = 9$.

shape form. It could be seen that the fiber is symmetrically bent in this case.

A fiber was also placed asymmetrically to the $(x,0)$ line meaning that the fiber would still cut through the $(x,0)$ line but the center mass of the fiber will be at $(x/c, y/a_0) = (0.8, 0.003)$. Figure 4.15 shows that a very flexible fiber with Young's modulus of $10^7 Pa$ acts very similarly to the fiber that was placed with its center mass at $(x/c, y/a_0) = (0.8, 0)$ in Figure 4.14. A fiber with intermediate and low flexibility (Young's modulus of $10^8 Pa$ and $10^9 Pa$) starts to bend asymmetrically (unlike Figure 4.14A-B, Figure 4.15A-B is not perfectly symmetrical), which results in a different shape from the one in Figure 4.14. This becomes more evident as Young's modulus is increased.

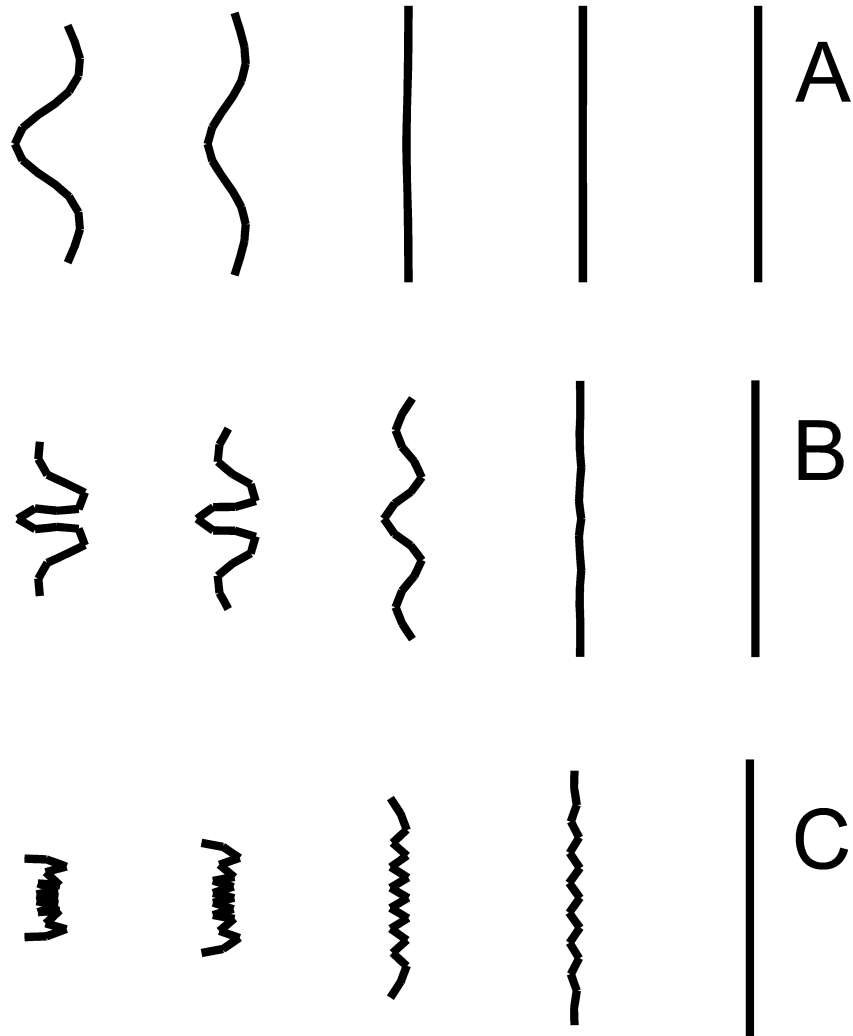


Figure 4.14: Fiber orientation and deformation in squeeze flow for three values of Young's modulus $A.10^9 Pa$, $B.10^8 Pa$ and $C.10^7 Pa$ for fiber placed at the initial position of $(x/c, y/a_0) = (0.8, 0)$ using coordinates of Figure 1.10. The fiber is presented at times: 0, 2.37, 5.54, 8.13 and 8.8 s.

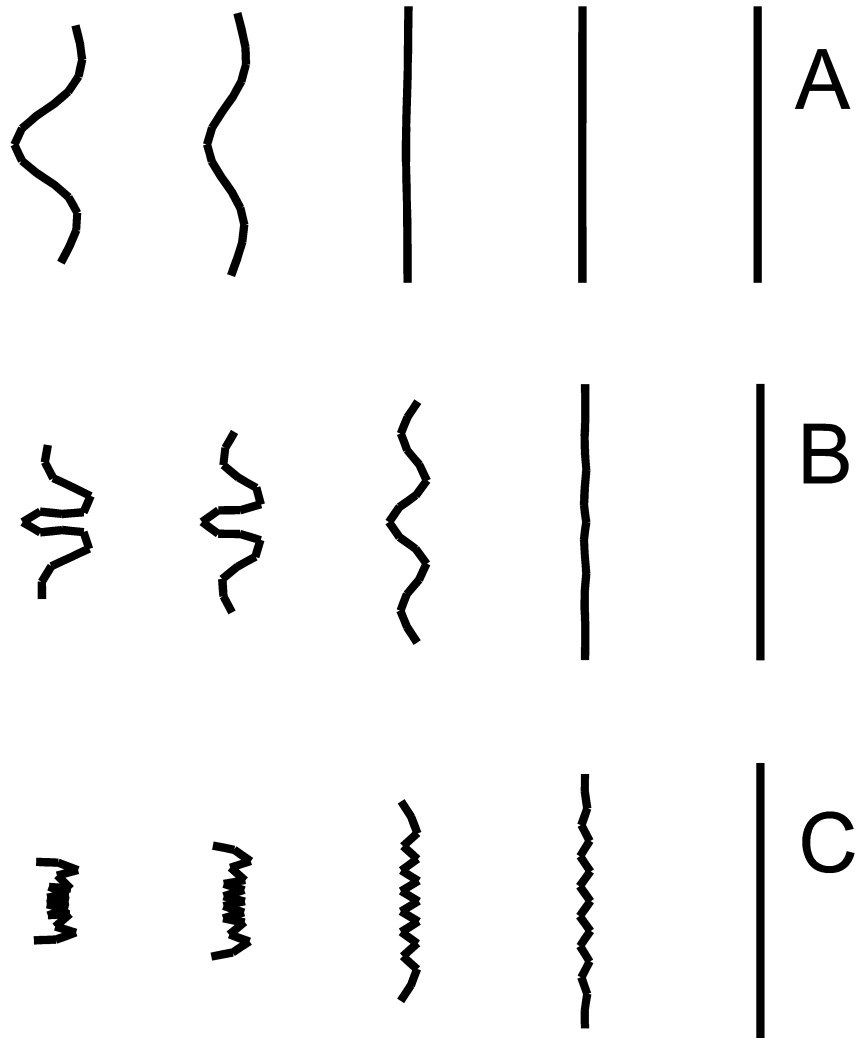


Figure 4.15: Fiber orientation and deformation in squeeze flow for three values of Young's modulus $A.10^9 Pa$, $B.10^8 Pa$ and $C.10^7 Pa$ for fiber that was placed at the initial position of $(x/c, y/a_0) = (0.8, 0.003)$ using coordinates of Figure 1.10. The fiber is presented at times: 0, 2.37, 5.54, 8.13 and 8.8 s.

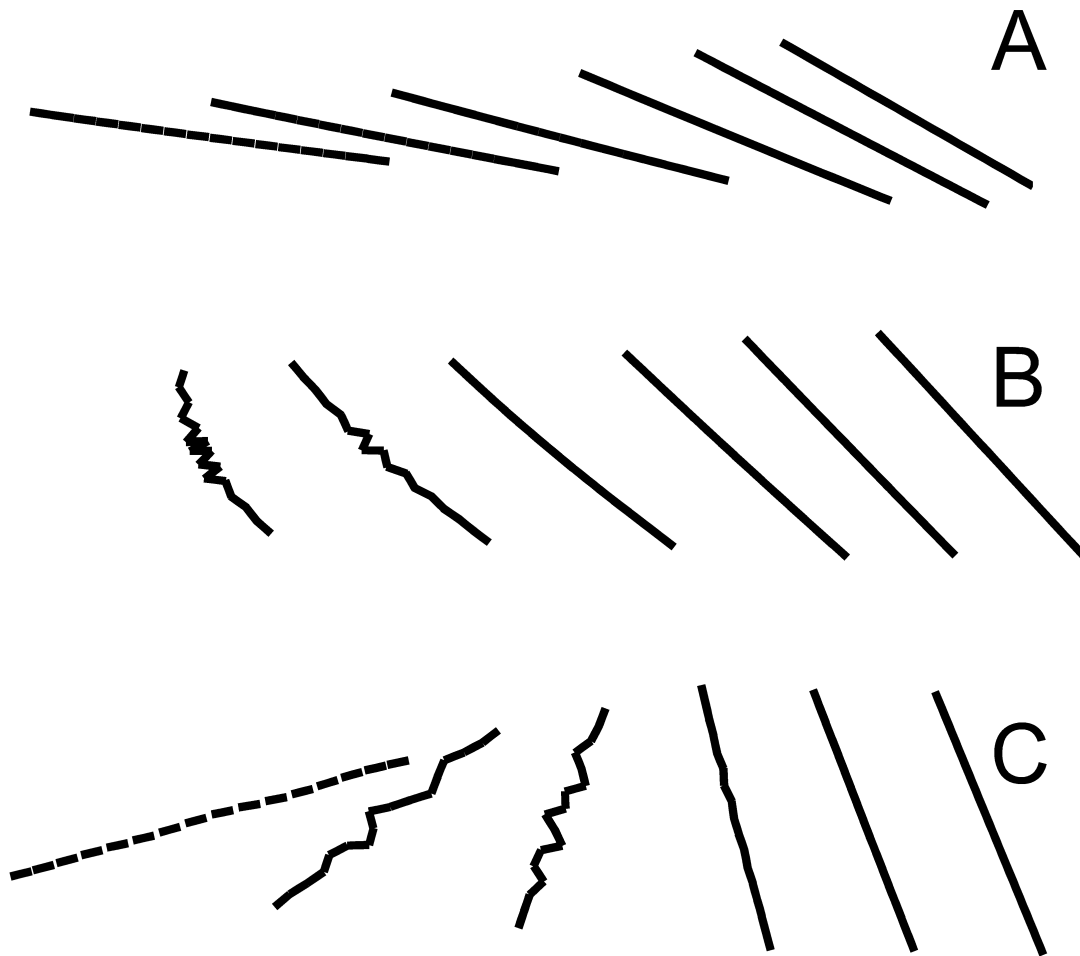


Figure 4.16: Fiber orientation and deformation in squeeze flow for Young's modulus of $10^7 Pa$. The fiber is placed with center mass at $(x/c, y/a_0) = (0.8, 0.8)$ at three different initial orientations: *A*. -0.2π , *B*. -0.3π , *C*. -0.4π . The fiber is presented at times: 0, 2.37, 5.54, 8.13, 8.8 and 9.2 s.

A fiber with Young's modulus of $10^7 Pa$ was placed with its center of mass at $(x/c, y/a_0) = (0.8, 0.8)$ at various orientations relative to the x axis: $A. -0.2\pi, B. -0.3\pi, C. -0.4\pi$. The results are presented in Figure 4.16. In these cases the angular velocity generated by velocity from x direction is competing with angular velocity generated by the velocity from y direction. Since the vorticity tensor of y velocity is zero (eq. (4.3)) it generates velocity only through deformation tensor, pushing the fiber to the fastest track to the horizontal position (which is equilibrium position for v_y). As a result, the fiber which is highly oriented in the direction against the angular velocity generated by v_x (close to horizontal position, case A) will get oriented in the opposite direction to the fiber which is much less initially oriented in this direction (close to vertical position, case C), in other words case A will exhibit positive radial velocity while case C will show negative radial velocity. In case B, which has the initial orientation between case A and C, the fiber will be severely deformed by the two rival velocities. These results are presented in Figure 4.16. It was found that fiber's linear velocity does not depend on its original orientation or Young's modulus hence all the three cases described in Figure 4.16 move in the same path which could be observed on Figure 4.8 $(x/c, y/a_0) = (0.8, 0.8)$ case.

System B

Figures 4.17-4.20 present results of a study of the influence of Young's modulus and initial location on fiber deformation for the case where system dimensions are comparable to fiber length.

Figure 4.17 shows, that the fiber with initial position near the upper moving wall shown in Figure 1.10 $((x/c, y/a_0) = (0.8, 0.8))$ will simply orient itself in the direction of elongational flow, which exists at the horizontal middle line $(x, 0)$. As the Young's modulus decreases the fiber will still remain straight, but rigid segments will start to separate as the Young's modulus magnitude is not enough to keep the rigid parts together.

As the fiber is placed closer to the horizontal mid-line $(x, 0)$ of the system in Figure

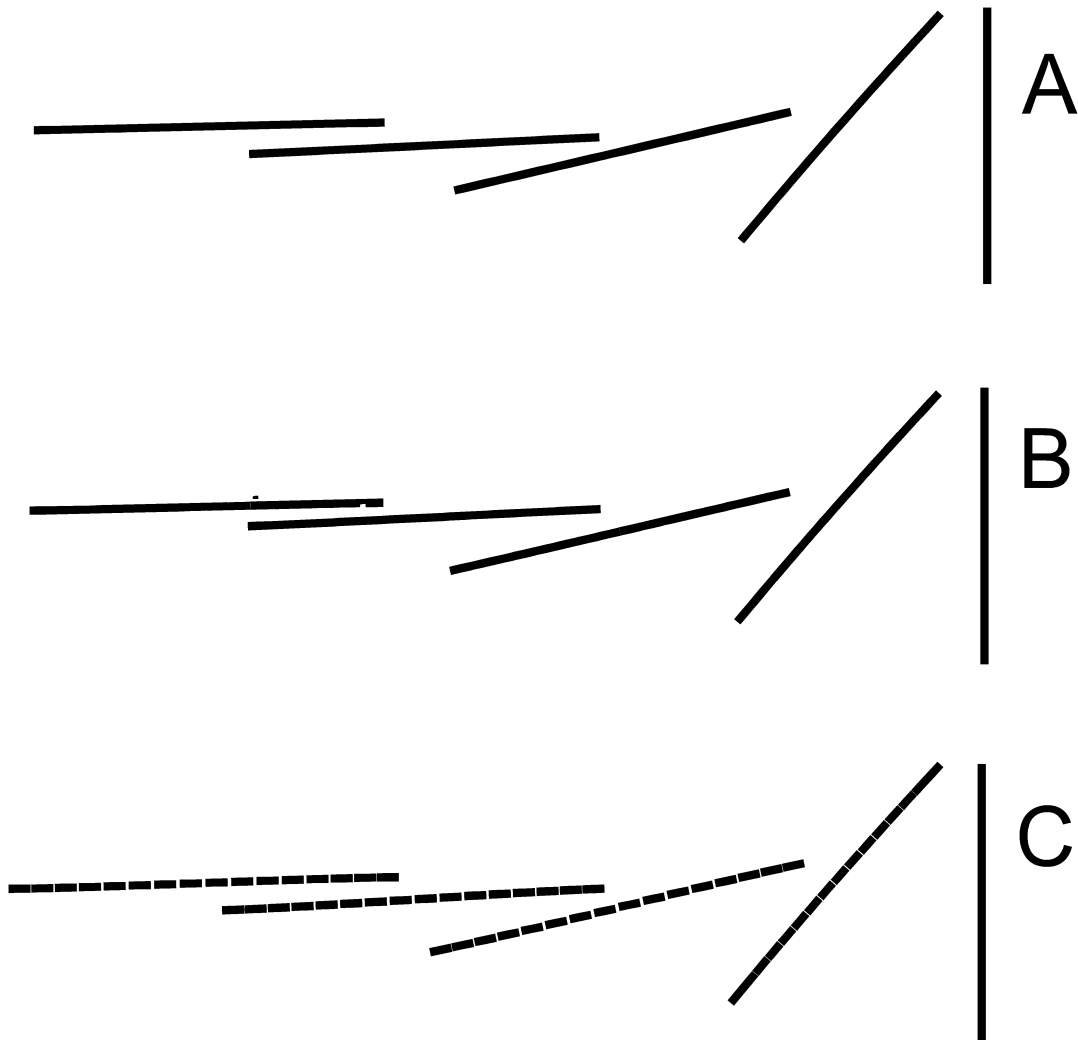


Figure 4.17: Fiber orientation and deformation in squeeze flow for three values of Young's modulus $A.10^9 Pa$, $B.10^8 Pa$ and $C.10^7 Pa$ for fiber placed at the initial position of $(x/c, y/a_0) = (0.8, 0.8)$. The fiber is presented at times: 0, 2.37, 5.54, 8.13 and 8.8 s.

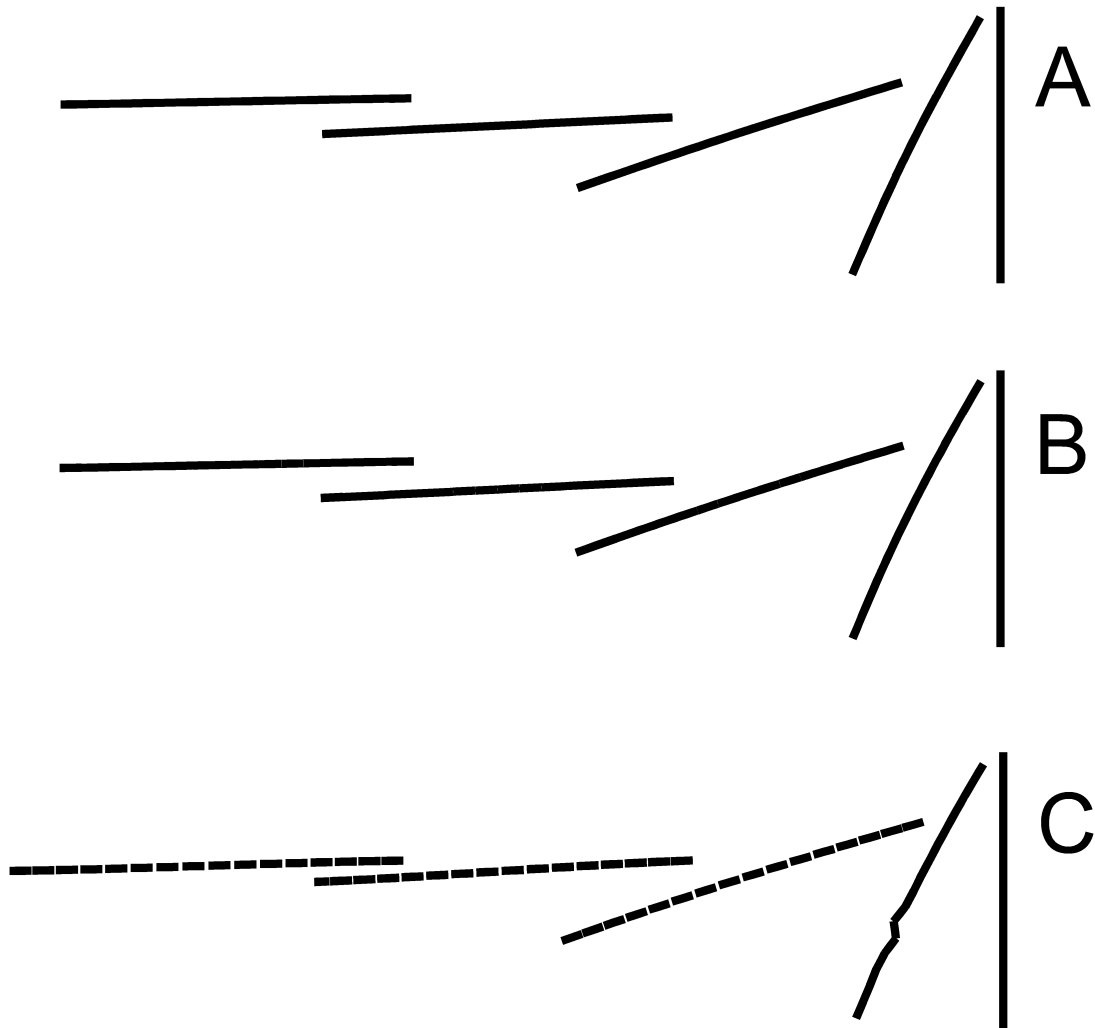


Figure 4.18: Fiber orientation and deformation in squeeze flow for three values of Young's modulus $A.10^9 Pa$, $B.10^8 Pa$ and $C.10^7 Pa$ for fiber placed at the initial position of $(x/c, y/a_0) = (0.8, 0.4)$. The fiber is presented at times: 0, 2.37, 5.54, 8.13 and 8.8 s.

1.10 ($(x/c, y/a_0) = (0.8, 0.4)$), the fiber will bend for lower values of Young's modulus (Figure 4.18C compared with Figure 4.17C) as it progresses in the horizontal direction until at some point it will be straightened and stretched. For higher values of Young's modulus the fiber will just orient itself in the direction of the elongation flow in horizontal mid-line $(x, 0)$ while for smaller Young's modulus the fiber will start to bend, as shown in Figure 4.18. As was mentioned previously the snapshots of fiber deformation progression are all taken at the same times namely: 0, 2.37, 5.54, 8.13 and 8.8 s hence it allows to compare speed of orientation between cases. It could be noted that the orientation in the cases presented in Figure 4.17 and Figure 4.18 are more rapid than the orientation observed in Figure 4.9 and Figure 4.10.

Fiber placed at the horizontal mid-line of Figure 1.10 ($(x/c, y/a_0) = (0.8, 0)$) will get squeezed symmetrically (Figure 4.19), and the resulting shapes will differ from the shapes that were obtained in Figure 4.14 by having less potential places for buckling.

A fiber can be placed in a manner such that the horizontal mid-line $(x, 0)$ goes through it, but does not cut it symmetrically, with its center of mass at $(x/c, y/a_0) = (0.8, 0.03)$. The reason for choosing a different dimensionless position from the one discussed in system A is that the absolute position $(x, y) = (0.8, 0.003)$, which is the same in both systems, is much more important in this case. If the same dimensionless position would be chosen for this case the horizontal center would cut too close to the center of the fiber. In this case the fiber will be squeezed asymmetrically (Figure 4.20). The asymmetry in this case is much more evident than in the case with larger system (Figure 4.15), and there are less potential places for buckling.

Influence of wall velocity was investigated in Figure 4.21. Case presented in Figure 4.9C was investigated for system A but with $R=0.1$ (eq. (4.1)) which increased the wall velocity by more than two (ratio of velocities changes with time). Due to different velocities, fibers from 4.21 and 4.9C will not be in the same location at the same time, however, it is easy to prove that the change in the R parameter (which affects the plate velocity) will not change the path of the fiber hence the comparison will be made on the basis of space meaning the shapes of the fiber on Figure 4.21

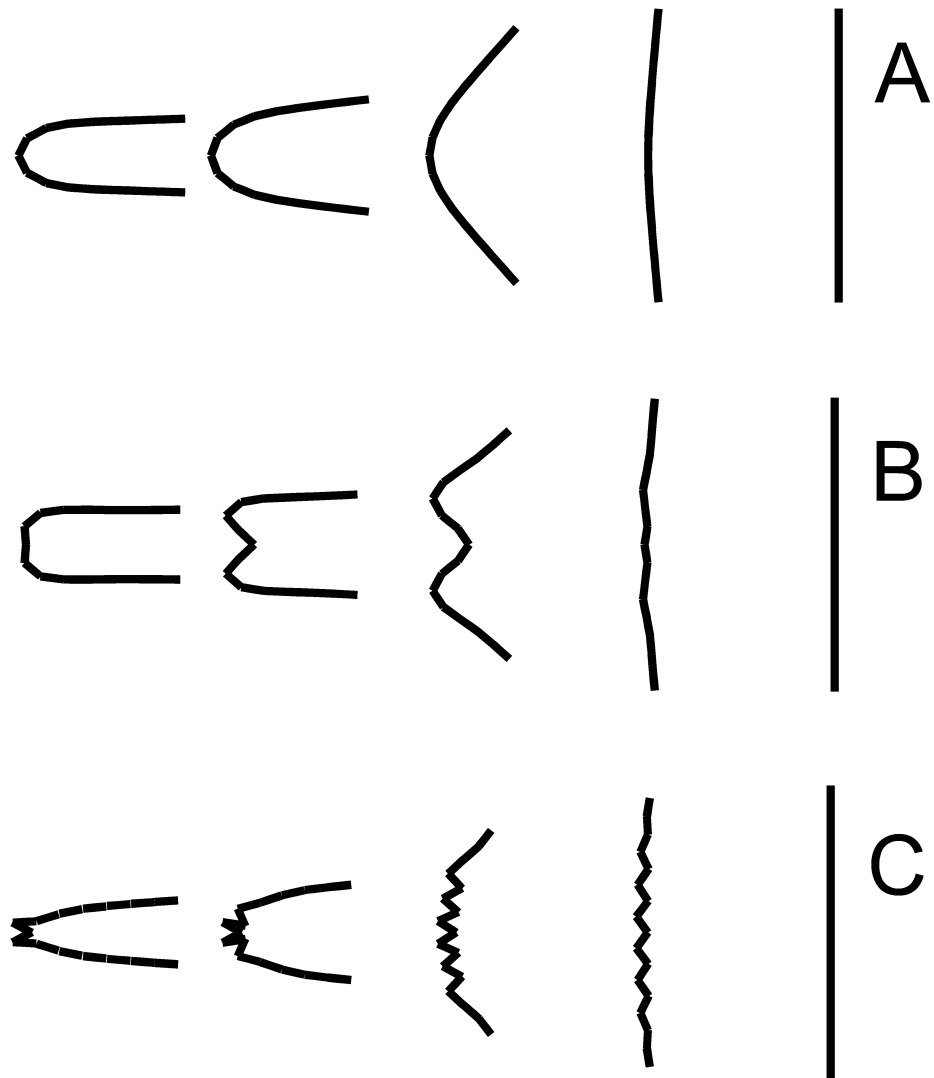


Figure 4.19: Fiber orientation and deformation in squeeze flow for three values of Young's modulus $A.10^9 Pa$, $B.10^8 Pa$ and $C.10^7 Pa$ for fiber placed at the initial position of $(x/c, y/a_0) = (0.8, 0)$. The fiber is presented at times: 0, 2.37, 5.54, 8.13 and 8.8 s.

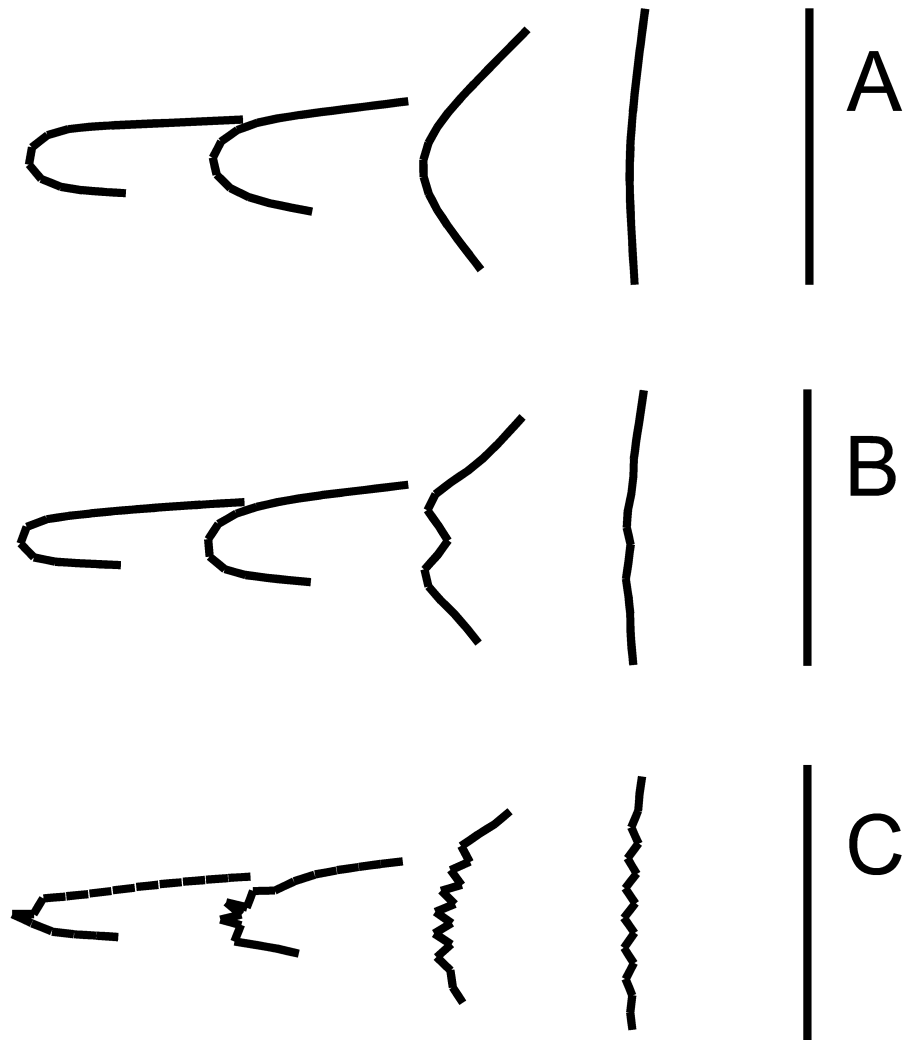


Figure 4.20: Fiber orientation and deformation in squeeze flow for three values of Young's modulus $A.10^9 Pa$, $B.10^8 Pa$ and $C.10^7 Pa$ for fiber placed at the initial position of $(x/c, y/a_0) = (0.8, 0.03)$. The fiber is presented at times: 0, 2.37, 5.54, 8.13 and 8.8 s.

still correspond to locations described on Figure 4.8 with the difference that now the fiber gets to this location at times 0, 1.13, 2.75, 4.07, 4.34 s. By comparing Figure 4.21 with Figure 4.9C it could be seen that the deformation of the fiber is increased slightly by increasing the wall velocity.

It is desired to have long straight fibers in long fiber thermoplastic part in a compression process [15], [114]. By studying and comparing results from system A and B, several operational parameters could be observed, which would contribute to the desired result. It could be seen that in both systems fibers, which were initially located higher in the system end up in a straight form and have less potential buckling possibilities during the flow. Both systems A and B are designed in a way that all the velocities and velocity derivatives in space are the same for both systems at a dimensionless coordinate $(x/c, y/a)$ except for two: v_y , which is an order of magnitude lower, in system B; however, since the dimensions of system B are also one order of magnitude lower, the path of the fiber along the dimensionless coordinate $(x/c, y/a)$ will be the same in both systems. Since the different plate velocity (a) in the system will not change the path of the fiber and fiber orientation and deformation is affected by the relative velocity along the rigid segments and between their centers of mass, which are the same for both systems, it is expected that different v_y will not cause any dif-

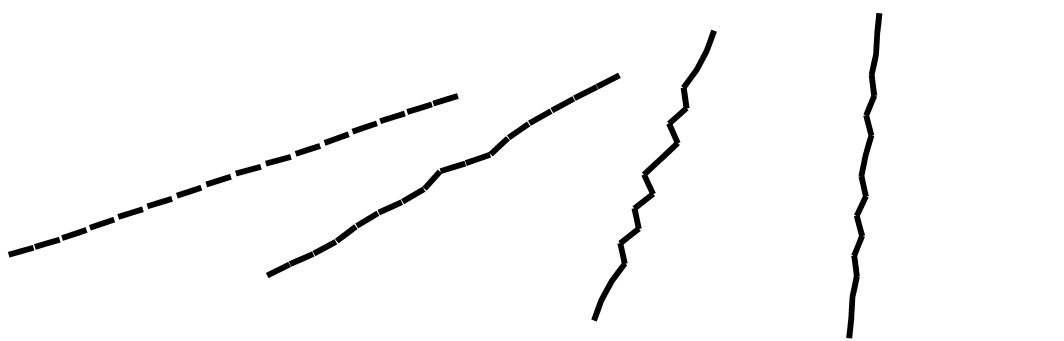


Figure 4.21: Fiber orientation and deformation in squeeze flow for three Young's modulus $10^7 Pa$ placed at initial position $(x/c, y/a) = (0.8, 0.8)$ in system A, with flow parameter $R = 0.1$. The fiber is shown at time: 0, 1.13, 2.75, 4.07, 4.34 s.

ference in the deformation shapes between two systems. The other parameter that is different between two systems is $\frac{\partial v_x}{\partial y}$ which is one order of magnitude greater in system B. This parameter appears to be crucial to fiber orientation and deformation as it is evident from eq. 4.4. It could be seen by comparing the results from system A and B that the fibers placed in system B are always smoother with less buckling possibilities and achieve steady state orientation faster than fibers placed in system A at the same dimensionless coordinate $(x/c, y/a)$. Thus, it can be concluded that larger $\frac{\partial v_x}{\partial y}$ in a system would result in smoother and longer fibers (since they will not break) and more orientation in the final product. The effect of seeing non-smooth systems is not limited to large systems, as a smaller system would provide similar results under the condition that higher axis ratio fiber would be used. According to We number we would expect that increasing the shear rate would increase the bending of the fiber. Shear rate in system B is approximately order of magnitude higher than in system A, however, the fibers in system B seem more rigid than in system A. Nevertheless when shear rate was increased due to the increase in wall velocity the fiber showed slightly more bending, hence the effect of shear rate in squeeze flow on bending can not be explained by simple We number. It was observed for both systems that unless the fiber cuts the horizontal center line of the system at some point of time and providing it has enough time it will always end up in a steady state orientation which is parallel to the plates.

Chapter 5

Interactions

Interactions between fibers are implemented through elastic collisions between fibers. This is done by representing cylinders through collection of spheres. The method is described in detail in Chapter 2.

5.1 Rigid Cylinders

Interactions between two rigid cylinders in a simple shear flow were studied using the algorithm described in Chapter 2. Two rigid cylinders of $1mm$ length with axis ratio of 5 are placed at simple shear flow with shear rate of $4s^{-1}$, the initial distance between centres is set to $0.0006m$ along the x axis. The results as shown in Figure 5.1. Figure 5.1 describes a cycle of cylinder interactions divided into four stages:

Stage A. In Figure 5.1, the cylinders are first approaching each other through rotation (centers of cylinders remain at the same distance but the head of black cylinder is approaching the tail of the blue cylinder). Once the cylinders are touching they can no longer rotate as they can not pass through each other.

Stage B. At this point the cylinders start to interact with each other in the y axis direction (the black cylinder is pushed up while the blue cylinder is pushed

down). As the center of the black cylinder gets higher compared to the blue cylinder, the linear velocity of the black cylinder increases compared to the velocity of the blue cylinder (in simple shear velocity increases with the coordinate).

Stage C. The black cylinder, which is now travelling faster than the blue cylinder, is now passing across the blue cylinder from above while both cylinders continue to rotate together. Eventually the cylinders switch places and the cylinder that was originally in the back moves to the front.

Stage D. Due to the fact that the black cylinder is slightly higher than the blue cylinder it is moving faster, which results in separation.

Several literature sources [24, 72, 73] agree with steps A-C although the experiments were made with spheres and not with cylinders. For stage D, however, literature suggests that after the rotation the cylinder's center mass should be at the same distance as it was in the initial conditions thus the system has returned to its initial state. The reason for the results discrepancy between the literature and our simulation is the absence of attractive force, i.e lubrication force. Several publications show that the lubrication force, which is a major factor in spheres interactions, is only important in cylinders interactions in the two dimensional simulation case [68, 77].

Mason and Manley [24] showed that the period of rotation T is influenced by interactions. In their experiments they showed that the period of rotation increase due to presence of other cylinders. It was impossible to obtain quantitative results regarding the dependence of rotation time from initial fiber distance and length. Rigid fibers of $0.2mm$ diameter and various lengths were places to simple shear flow simulation with shear rate of $4s^{-1}$ at different distances from each other. Figure 5.2 presents the results in dimensionless form of rotation time (rotation time with interactions divided by rotation time without interactions) change as a function of initial distance between cylinders. Figure 5.2 shows that as the initial distance between the cylinders is increased (in the range that still allows interactions) the rotation time increases. This is due to the fact that the farther the cylinders are apart initially the longer

is the distance they need to slide across each other (stage C). During stage C the cylinders are slowing each other's rotation; hence the longer this stage, the longer overall rotation becomes. Although all the three axis ratio cylinders fall on the same line of dimensionless rotation time dependence with dimensionless distance between fibers, stagnant areas could be seen on the plot, where rotation time remains constant while the distance is increasing. This area has lengths of approximately one sphere diameter, which is an indication of numerical error resulting from representation of a cylinder by a collection of spheres. In the rotation time calculation only half rotation time is taken into account. During the first half of rotation only repulsion forces are active and they are taken into account through elastic collision forces, while for the second period of rotation attraction forces that are not represented in a simulation would come into effect. Since both halves of rotation period should take the same time it is possible to include only the first half and simply to multiply it by two.

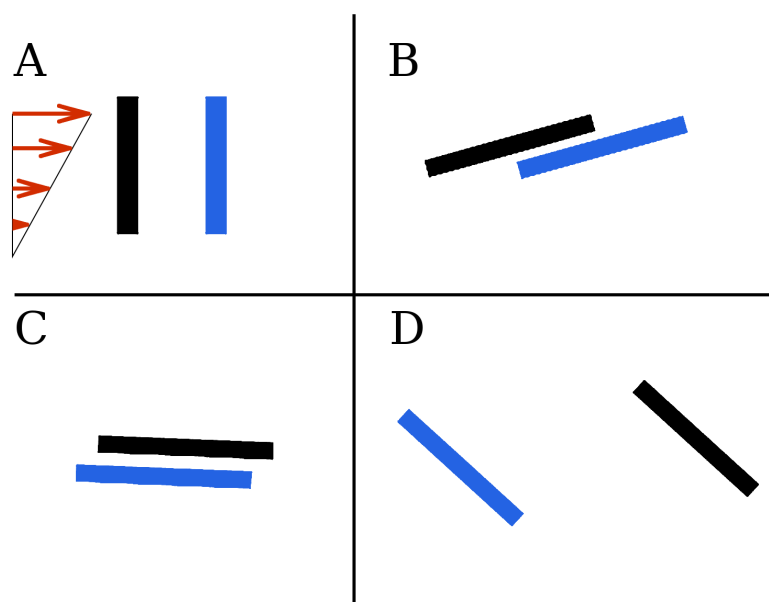


Figure 5.1: Interactions between rigid cylinders at shear rate of $\dot{\gamma} = 4 \frac{1}{s}$.

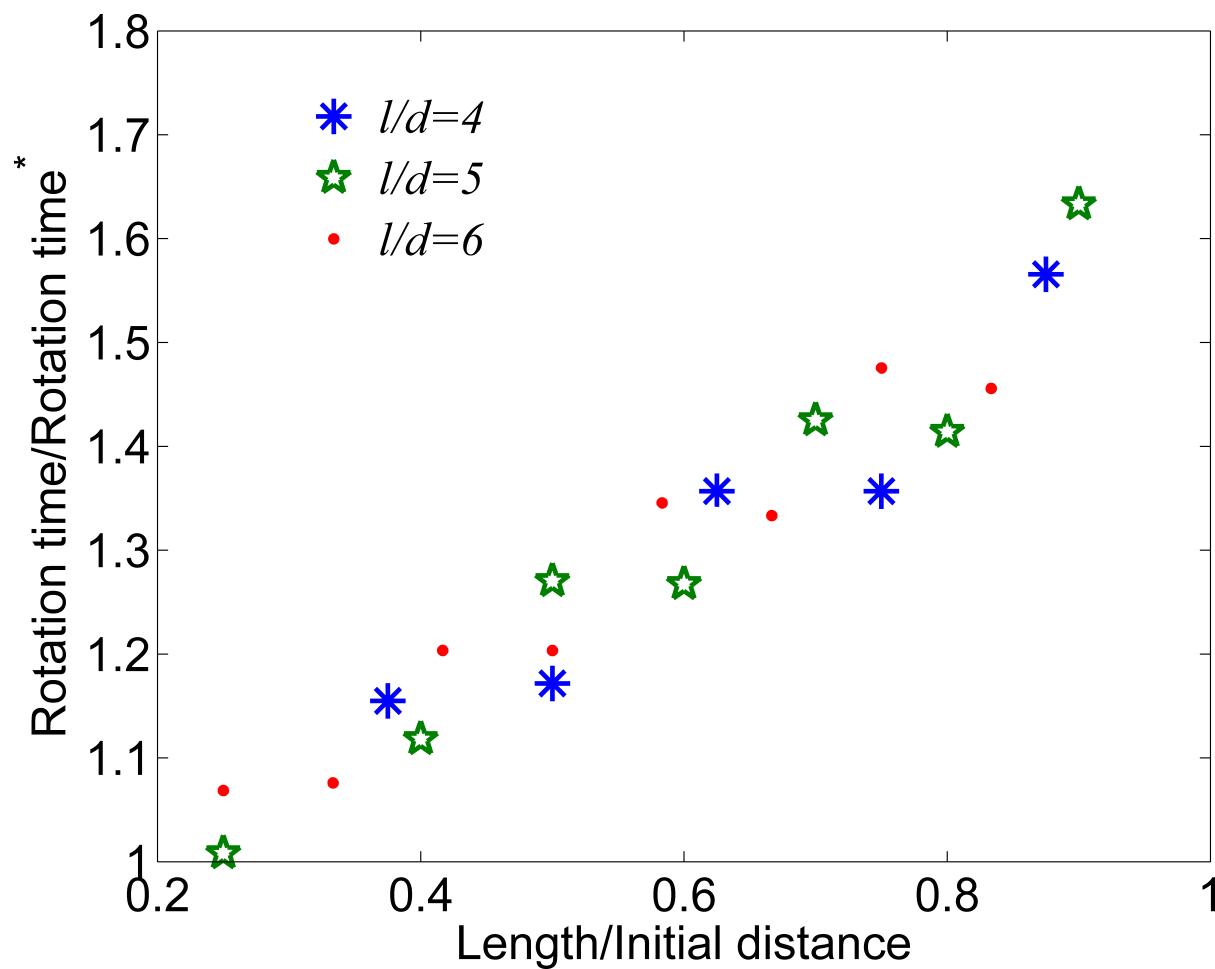


Figure 5.2: Normalised rotation time with dependence to ratio of length of cylinders to initial distance between cylinders centers of mass.

5.2 Flexible Fibers

5.2.1 Simple Shear Flow

Two flexible fibers with length of $8mm$, diameter of $0.2mm$ and Young's modulus of $10^8 Pa$ were placed in a simple planar shear flow with shear rate of $4s^{-1}$ viscosity of $1000Pa \cdot s$ at distance of $4mm$ from each other, Figure 5.3 shows the results of this simulation. Interactions between flexible fibers were studied in both simple shear and squeeze flow cases, these results are presented in Figures 5.3-5.5. For the simple shear flow flexible fibers will first try to rotate rigidly into horizontal position just as a single flexible fiber in Figure 3.5. Due to rotation, the back end of the front fiber and the front of the fiber in the back will start to interact. Just as in the case of rigid cylinders the fibers will slide across each other pushing the back fiber slightly up and the front fiber slightly down. As the fibers slide across each other the combined structure of both flexible fibers starts to bend as if a single fiber was bending. Eventually the fibers separate and finish the rotation as antisymmetric version of each other. Due to the lack of lubrication forces just as in the rigid fiber case flexible fibers are simulated only for the first half of rotation period.

5.2.2 Squeeze Flow

Interactions between flexible fibers in squeeze flow were studied with respect to system A defined in Chapter 4. It is difficult to induce interactions in a squeeze flow due to existence of flow velocity gradient in all directions which results in fibers separating from each other. Hence in order to observe interactions at least one fiber has to be fixed in at least one of the directions. This could be done by placing one of the fibers in the horizontal middle of the system thus fixing it in the y direction. In Figure 5.4 two fibers with length of $10mm$, diameter of $0.2mm$ and Young's modulus of $10^8 Pa$ start in perpendicular position to each other. The first fiber is placed in horizontal position in the center of vertical axis $(0.8,0)$ while the second fiber is placed in a vertical position slightly above the first fiber $(0.798,0.0051)$. The hori-

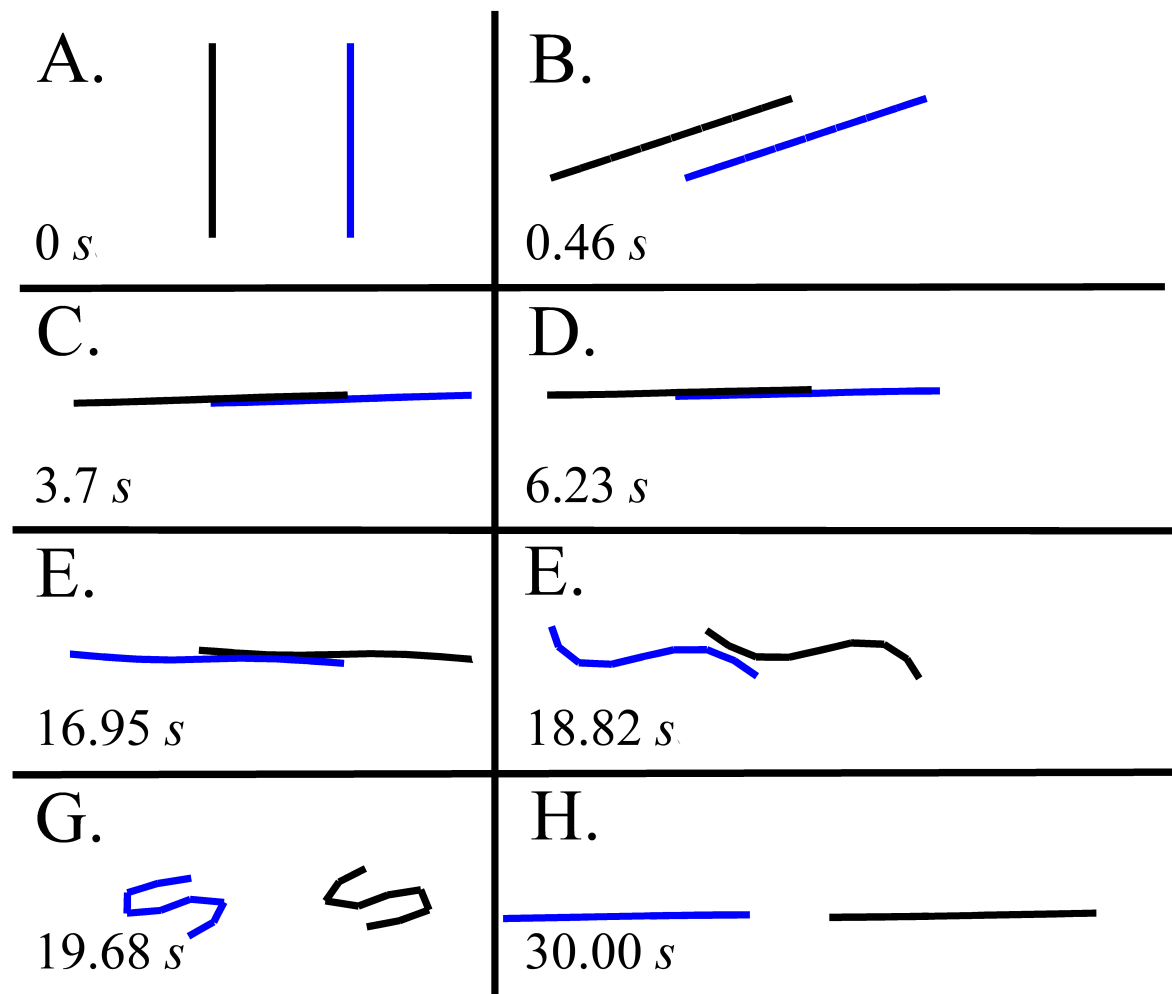


Figure 5.3: Interactions between 8mm flexible fibers placed in initial distance of 4mm in a simple shear flow ($4s^{-1}$) at viscosity of $1000Pa \cdot s$.

zontal fiber is pushed by the flow field from above and below which keeps it straight and allows velocity only in the vertical direction. Since the horizontal fiber is kept straight by the flow field it affectively acts as a wall toward the vertical line. The vertical fiber is hence compressed and bends against the horizontal fiber. In another simulation the same two fibers are placed in a different position. In Figure 5.5 one of the fibers start at the position where the first fiber is placed in a vertical position in the horizontal center line in the system $(0.8,0)$ and the second fiber is pressed to him at angle of $5/6\pi$ and placed at $(0.801,0.007)$. Due to the flow, the first fiber is allowed to move only in the horizontal direction where it is being compressed by the flow. The second fiber is moved by the flow toward the horizontal center of the system, which results in even farther compression of the first fiber. The both squeeze flow interaction cases were chosen in a way that would allow qualitative prediction of the results before running the simulation, so that the results could be evaluated. In both cases the fibers behaved as was expected from them. Lubrication forces are not important in the rheometric flow case due to low contact area compared to a simple shear flow case, which is due to the initial position of the fibers and since they are being separated by the flow.

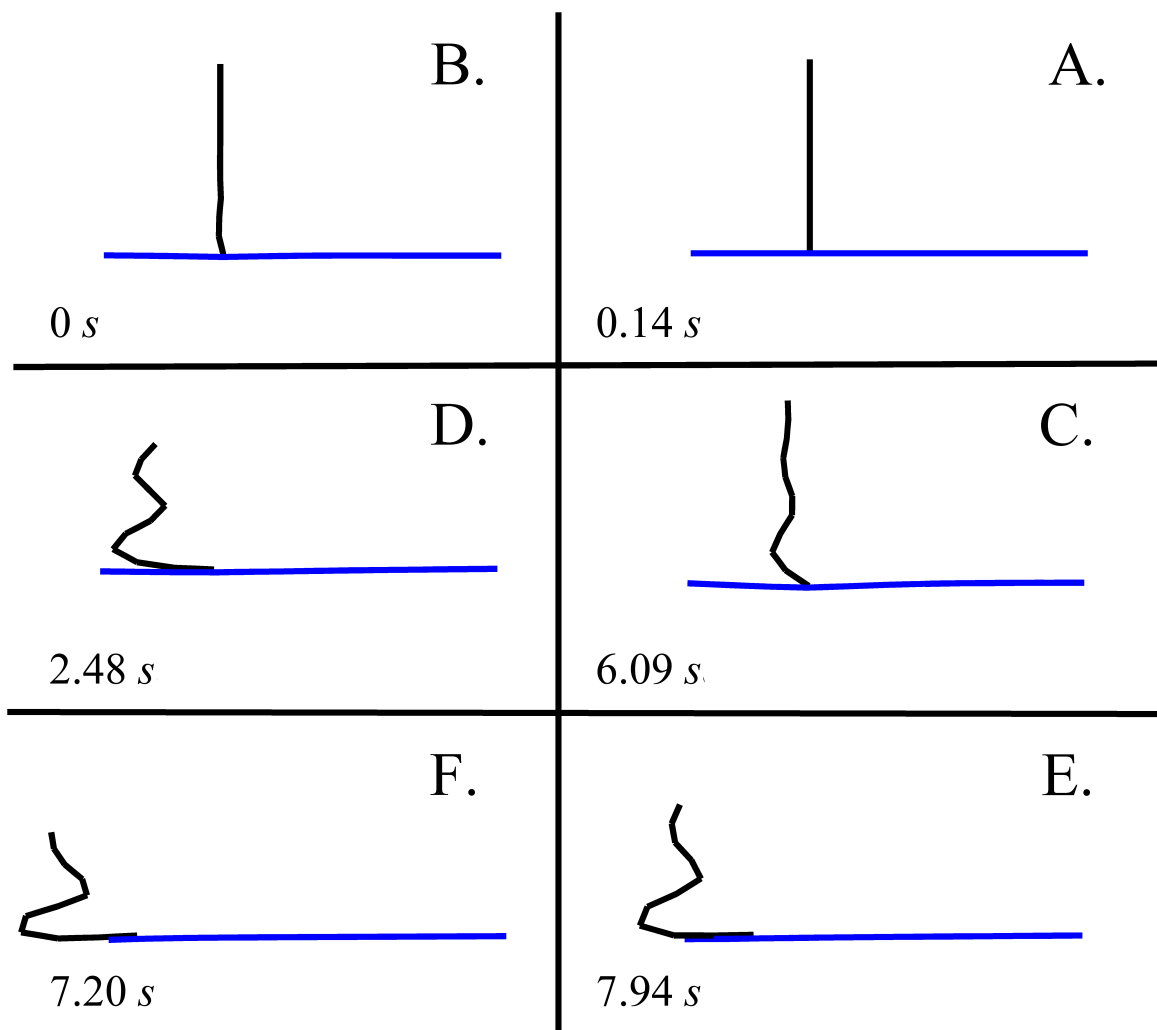


Figure 5.4: Interactions between two flexible fibers in squeeze flow where the fibers start perpendicular position to each other.

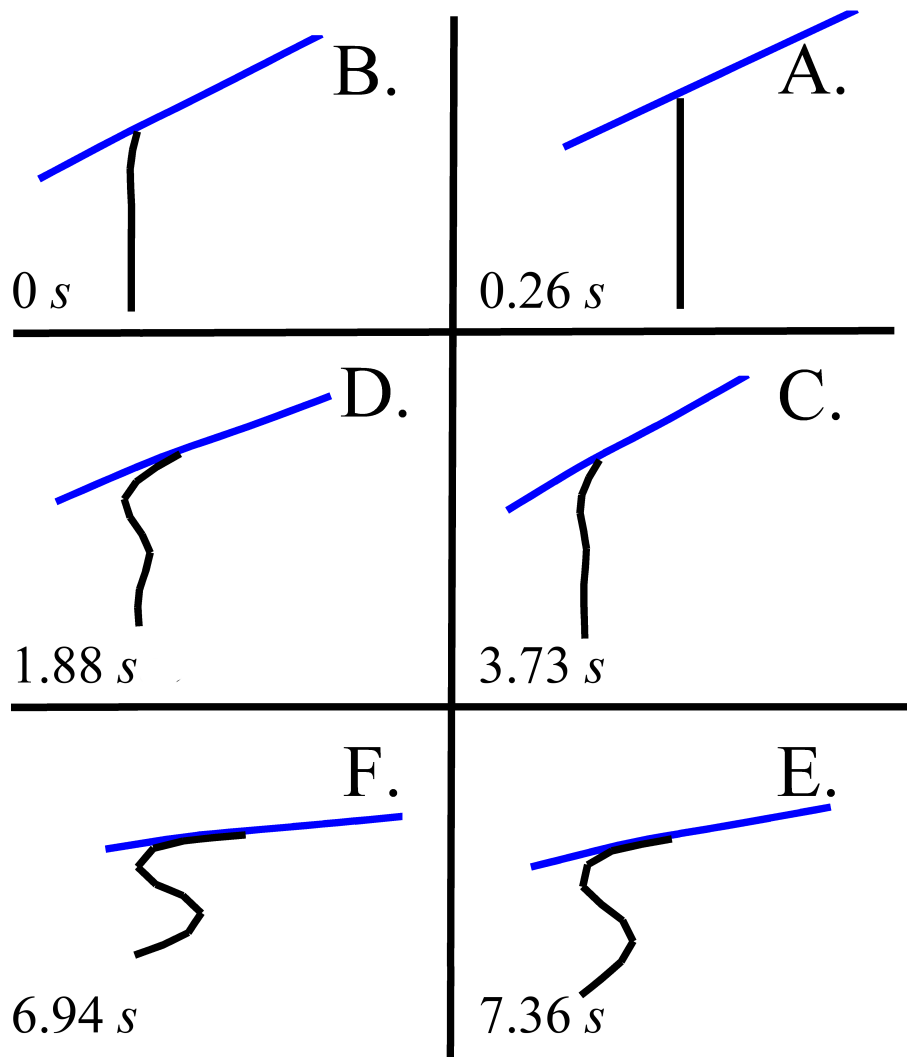


Figure 5.5: Interactions between two flexible fibers in squeeze flow where the fibers start at an angle of $5/6\pi$ angle to each other.

Chapter 6

Conclusions

A two dimensional long flexible fiber model was developed. This model employs unique torque calculation mechanism presented in Figure 2.5 and rotational friction coefficients for cylinders eq. (2.18) both of which were developed specifically for this model. A formula for infinite axis ratio cylinder friction coefficient eq. (3.1) was obtained. Friction coefficients values for finite axis ratio cylinders were obtained for several geometry values by fitting (Table 3.1). This new model should be able to simulate fibers of any length as in its development no length limiting assumptions were used.

The new developed model was tested in two flow cases: simple shear flow and rheometric squeeze flow.

6.1 Simple Shear Flow

The model was applied for a simple shear flow and compared to known literature results. The comparison showed that proposed fiber model matches well to experimental results and theory found in the literature (Figures 3.4, 3.5 and 3.9). Since the model is designed in a general form and it was shown that friction coefficients are independent of flow conditions (Figure 3.3) it could be applied for a rheometric squeeze flow case.

6.2 Rheometric Squeeze Flow

Rigid segments simulated in rheometric squeeze flow were compared to results obtained by Jeffery's model. The results for infinite axis ratio match perfectly to Jeffery's results (Figure 4.6) and the results for finite axis ratio matches well (Figure 4.7). The author believes that this results validate the model for rheometric squeeze flow, as no other simulation or experimental references were found.

The comparison between different systems allowed to find some rules of thumb in compression molding operation. The fibers should have high Young's modulus, the fibers should be located as far as possible from the horizontal center of the mold, the compression charge should be as thin as possible and the viscosity of the matrix should be as low as possible.

The effects of elongational and compression of a long flexible fiber were observed in the solution of the rheometric squeeze flow system. Although the current model does not permit fiber breakage it could be added into the model thus allowing to predict fiber breakage providing that material parameters of the fibers would be provided.

6.3 Interactions

Elastic collision interactions were implemented in the proposed model and simulations of fibers were conducted in simple shear and rheometric squeeze flows. Rotation time dependence on initial fiber distance was studied in simple shear flow and it was found that in its dimensionless form the results are independent of fibers axis ratio. In a simulation of flexible fibers in a squeeze flow where one of the fibers was placed horizontally middle of the system, the fiber in the horizontal middle behaved like a wall as the flow acts symmetrically on the fiber in the vertical direction. This interaction model can be used for initial study and understanding of interactions between long flexible fibers. These interactions could then be integrated into a Folgar-Tucker [18] type of interactions for concentrated suspensions.

6.4 Future Work

The results presented in this thesis were obtained using Matlab. In several implementations: squeeze flow and interaction implementation, numerical error was observed under certain conditions. This error was overcome in squeeze flow by changing the ODE solver from ODE15s used for simple shear to ODE23tb used in squeeze flow. The authors, however, could not find the solution to numerical error during interactions calculations under certain conditions. Hence it is important to transform the code into higher programming level language such as C++ or Fortran where there are more available ODE solvers.

Current model has to be expanded into three dimensional model. In order for that to be done rotational friction coefficient has to be expanded to account for the third dimension and a twisting interaction between rigid segments has to be added similarly to Yamamoto and Matsuoka [65].

Once the model is expanded into third dimension, concentrated fiber systems could be solved. The main idea could be easily explained using the Jeffery's model solution of a simple shear flow system that could be observed on Figure 1.6. As could be seen no matter what is the initial orientation of the fiber it will simply continue to rotate in a predefined manner, hence if the orientation for one fiber is solved it is not necessary to solve the orientation for other fibers provided that their initial orientation is given. Although simple shear is easy example since flow pattern and its derivatives are the same everywhere in the system, the same logic although in a more complex manner could be applied to harder flow patterns.

The proposed idea will work in the following way: a fragment of concentrated system with fibers should be calculated. Overall orientation tensor of rigid segments composing the fibers in that fragment could then be calculated as well. Orientation tensor everywhere else in the system can then be calculated by applying a mask that takes into consideration flow progression and different fiber initial orientation. In addition systems rheology could also be updated with respect to changing orientation. This idea can work only for the case that initial orientation everywhere in the

system is known. The reason this is such case is that the compressed polymer/fibers charge is prepared via twin screw extruder with patterned screws which means that the fibers in the charge are also patterned and could be expressed by a mathematical function.

Finally it is important to validate the model. Some preliminary validation work was made for this thesis and it is presented in Appendix A. More work should be done in this direction which would involve the use of different fluid media, different fibers and different flow conditions. In additions experiments with high concentration of fibers should also be conducted to study interaction.

Bibliography

- [1] C. Soanes and S. Hawker, *Compact Oxford English Dictionary of Current English*. New York: Oxford University Press, 3 ed., 2008.
- [2] G. Staab, *Laminar Composites*. Boston: Butterworth-Heinemann, 1 ed., 1999.
- [3] A. DiBenedetto, “Evaluation of fiber surface treatments in composite materials,” *Pure and applied chemistry*, vol. 57, no. 11, pp. 1659–1665, 1985.
- [4] F. L. Matthews and R. D. Rawlings, *Composite materials: engineering and science*. London: Chapman and Hall, 1 ed., 1994.
- [5] J. Thomason and M. Vlug, “Influence of fibre length and concentration on the properties of glass fibre-reinforced polypropylene: 1. tensile and flexural modulus,” *Composites Part A: Applied science and manufacturing*, vol. 27, no. 6, pp. 477–484, 1996.
- [6] J. Thomason and W. Groenewoud, “The influence of fibre length and concentration on the properties of glass fibre reinforced polypropylene: 2. thermal properties,” *Composites Part A: Applied Science and Manufacturing*, vol. 27, no. 7, pp. 555–565, 1996.
- [7] J. Thomason, M. Vlug, G. Schipper, and H. Krikor, “Influence of fibre length and concentration on the properties of glass fibre-reinforced polypropylene: Part 3. strength and strain at failure,” *Composites Part A: Applied Science and Manufacturing*, vol. 27, no. 11, pp. 1075–1084, 1996.
- [8] J. Thomason and M. Vlug, “Influence of fibre length and concentration on the properties of glass fibre-reinforced polypropylene: 4. impact properties,”

- Composites Part A: Applied Science and Manufacturing*, vol. 28, no. 3, pp. 277–288, 1997.
- [9] J. Thomason, “The influence of fibre length and concentration on the properties of glass fibre reinforced polypropylene: 5. injection moulded long and short fibre pp,” *Composites Part A: Applied Science and Manufacturing*, vol. 33, no. 12, pp. 1641–1652, 2002.
- [10] F. Truckenmüller and H.-G. Fritz, “Injection molding of long fiber-reinforced thermoplastics: A comparison of extruded and pultruded materials with direct addition of roving strands,” *Polymer Engineering & Science*, vol. 31, no. 18, pp. 1316–1329, 1991.
- [11] F. Henning, H. Ernst, and R. Brüssel, “Lfts for automotive applications,” *Reinforced plastics*, vol. 49, no. 2, pp. 24–33, 2005.
- [12] L. Carlsson, “Thermoplastic composite materials,” *Elsevier Science Publishers BV, Sara Burgerhartstraat 25, P. O. Box 211, 1000 AE Amsterdam, The Netherlands*, 1991.
- [13] M. Schemme, “Lft–development status and perspectives,” *Reinforced Plastics*, vol. 52, no. 1, pp. 32–39, 2008.
- [14] H. Hsiao and I. Daniel, “Elastic properties of composites with fiber waviness,” *Composites Part A: Applied Science and Manufacturing*, vol. 27, no. 10, pp. 931–941, 1996.
- [15] K. Ortman, D. Baird, P. Wapperom, and A. Aning, “Prediction of fiber orientation in the injection molding of long fiber suspensions,” *Polymer Composites*, vol. 33, no. 8, pp. 1360–1367, 2012.
- [16] G. B. Jeffery, “The motion of ellipsoidal particles immersed in a viscous fluid,” in *Proceedings of the Royal Society of London A: Mathematical, Physical and Engineering Sciences*, vol. 102, pp. 161–179, The Royal Society, 1922.
- [17] G. Youngren and A. Acrivos, “Stokes flow past a particle of arbitrary shape: a numerical method of solution,” *Journal of fluid Mechanics*, vol. 69, no. 02, pp. 377–403, 1975.

- [18] F. Folgar and C. L. Tucker III, "Orientation behavior of fibers in concentrated suspensions," *Journal of Reinforced Plastics and Composites*, vol. 3, no. 2, pp. 98–119, 1984.
- [19] M. C. Altan and L. Tang, "Orientation tensors in simple flows of dilute suspensions of non-brownian rigid ellipsoids, comparison of analytical and approximate solutions," *Rheologica acta*, vol. 32, no. 3, pp. 227–244, 1993.
- [20] G. Gauthier, P. Gondret, and M. Rabaud, "Motions of anisotropic particles: application to visualization of three-dimensional flows," *Physics of Fluids*, vol. 10, no. 9, pp. 2147–2154, 1998.
- [21] E. Cueto, R. Monge, F. Chinesta, A. Poitou, I. Alfaro, and M. R. Mackley, "Rheological modeling and forming process simulation of CNT nanocomposites," *International journal of material forming*, vol. 3, no. 2, pp. 1327–1338, 2010.
- [22] G. Taylor, "The motion of ellipsoidal particles in a viscous fluid," *Proceedings of the Royal Society of London. Series A, Containing Papers of a Mathematical and Physical Character*, vol. 103, no. 720, pp. 58–61, 1923.
- [23] B. Trevelyan and S. Mason, "Particle motions in sheared suspensions. i. rotations," *Journal of Colloid Science*, vol. 6, no. 4, pp. 354–367, 1951.
- [24] S. Mason and R. S. J. Manley, "Particle motions in sheared suspensions: orientations and interactions of rigid rods," in *Proceedings of the Royal Society of London A: Mathematical, Physical and Engineering Sciences*, vol. 238, pp. 117–131, The Royal Society, 1956.
- [25] E. Anczurowski and S. Mason, "Particle motions in sheared suspensions. xxiv. rotation of rigid spheroids and cylinders," *Transactions of The Society of Rheology*, vol. 12, no. 2, pp. 209–215, 1968.
- [26] E. Anczurowski, R. Cox, and S. Mason, "The kinetics of flowing dispersions: Iv. transient orientations of cylinders," *Journal of Colloid and Interface Science*, vol. 23, no. 4, pp. 547–562, 1967.

- [27] E. Anczurowski and S. Mason, "The kinetics of flowing dispersions: Iii. equilibrium orientations of rods and discs (experimental)," *Journal of Colloid and Interface Science*, vol. 23, no. 4, pp. 533–546, 1967.
- [28] H. Brenner, "The stokes resistance of an arbitrary particleii: an extension," *Chemical Engineering Science*, vol. 19, no. 9, pp. 599–629, 1964.
- [29] F. P. Bretherton, "The motion of rigid particles in a shear flow at low reynolds number," *Journal of Fluid Mechanics*, vol. 14, no. 02, pp. 284–304, 1962.
- [30] H. Brenner, "The stokes resistance of an arbitrary particleiii: shear fields," *Chemical Engineering Science*, vol. 19, no. 9, pp. 631–651, 1964.
- [31] O. Forgacs and S. Mason, "Particle motions in sheared suspensions: Ix. spin and deformation of threadlike particles," *Journal of colloid science*, vol. 14, no. 5, pp. 457–472, 1959.
- [32] O. Forgacs and S. Mason, "Particle motions in sheared suspensions: X. orbits of flexible threadlike particles," *Journal of Colloid Science*, vol. 14, no. 5, pp. 473–491, 1959.
- [33] W. Bartok and S. Mason, "Particle motions in sheared suspensions: V. rigid rods and collision doublets of spheres," *Journal of Colloid Science*, vol. 12, no. 3, pp. 243–262, 1957.
- [34] H. Goldsmith, S. Mason, and F. Eirich, "Rheology, vol. 4," *New York: Academic Press*, p. 85, 1967.
- [35] R. Cox, "The motion of long slender bodies in a viscous fluid part 1. general theory," *Journal of Fluid mechanics*, vol. 44, no. 04, pp. 791–810, 1970.
- [36] R. Cox, "The motion of long slender bodies in a viscous fluid. part 2. shear flow," *Journal of Fluid Mechanics*, vol. 45, no. 04, pp. 625–657, 1971.
- [37] J. Harris and J. Pittman, "Equivalent ellipsoidal axis ratios of slender rod-like particles," *Journal of Colloid and Interface Science*, vol. 50, no. 2, pp. 280–282, 1975.

- [38] D. Zhang, D. E. Smith, D. A. Jack, and S. Montgomery-Smith, “Numerical evaluation of single fiber motion for short-fiber-reinforced composite materials processing,” *Journal of Manufacturing Science and Engineering*, vol. 133, no. 5, p. 051002, 2011.
- [39] E. Abisset-Chavanne, F. Chinesta, J. Ferec, G. Ausias, and R. Keunings, “On the multiscale description of dilute suspensions of non-brownian rigid clusters composed of rods,” *Journal of Non-Newtonian Fluid Mechanics*, vol. 222, pp. 34–44, 2015.
- [40] H.-S. Dou, B. C. Khoo, N. Phan-Thien, K. S. Yeo, and R. Zheng, “Simulations of fibre orientation in dilute suspensions with front moving in the filling process of a rectangular channel using level-set method,” *Rheologica acta*, vol. 46, no. 4, pp. 427–447, 2007.
- [41] M. Doi, “Rotational relaxation time of rigid rod-like macromolecule in concentrated solution,” *Journal de Physique*, vol. 36, no. 7-8, pp. 607–611, 1975.
- [42] S. M. Dinh and R. C. Armstrong, “A rheological equation of state for semiconcentrated fiber suspensions,” *Journal of Rheology*, vol. 28, no. 3, pp. 207–227, 1984.
- [43] M. Doi and S. Edwards, “Dynamics of rod-like macromolecules in concentrated solution. part 1,” *Journal of the Chemical Society, Faraday Transactions 2: Molecular and Chemical Physics*, vol. 74, pp. 560–570, 1978.
- [44] M. Doi and S. F. Edwards, “Dynamics of rod-like macromolecules in concentrated solution. part 2,” *Journal of the Chemical Society, Faraday Transactions 2: Molecular and Chemical Physics*, vol. 74, pp. 918–932, 1978.
- [45] S. G. Advani and C. L. Tucker III, “The use of tensors to describe and predict fiber orientation in short fiber composites,” *Journal of Rheology*, vol. 31, no. 8, pp. 751–784, 1987.
- [46] E. Hinch and L. Leal, “Constitutive equations in suspension mechanics. part 2. approximate forms for a suspension of rigid particles affected by brownian rotations,” *Journal of Fluid Mechanics*, vol. 76, no. 01, pp. 187–208, 1976.

- [47] G. G. Lipscomb, M. M. Denn, D. Hur, and D. V. Boger, “The flow of fiber suspensions in complex geometries,” *Journal of Non-Newtonian Fluid Mechanics*, vol. 26, no. 3, pp. 297–325, 1988.
- [48] S. G. Advani and C. L. Tucker III, “Closure approximations for three-dimensional structure tensors,” *Journal of Rheology*, vol. 34, no. 3, pp. 367–386, 1990.
- [49] J. S. Cintra Jr and C. L. Tucker III, “Orthotropic closure approximations for flow-induced fiber orientation,” *Journal of Rheology*, vol. 39, no. 6, pp. 1095–1122, 1995.
- [50] R. S. Bay, *Fiber orientation in injection-molded composites: A comparison of theory and experiment*. PhD thesis, University of Illinois at Urbana-Champaign, 1991.
- [51] N. Phan-Thien, X.-J. Fan, R. Tanner, and R. Zheng, “Folgar–tucker constant for a fibre suspension in a newtonian fluid,” *Journal of Non-Newtonian Fluid Mechanics*, vol. 103, no. 2, pp. 251–260, 2002.
- [52] J. Férec, G. Ausias, M. Heuzey, and P. Carreau, “Modeling fiber interactions in semiconcentrated fiber suspensions,” *Journal of Rheology*, vol. 53, no. 1, pp. 49–72, 2009.
- [53] R. S. Bay and C. L. Tucker III, “Fiber orientation in simple injection moldings. part i: Theory and numerical methods,” *Polymer composites*, vol. 13, no. 4, pp. 317–331, 1992.
- [54] B. E. Verweyst and C. L. Tucker III, “Fiber suspensions in complex geometries: flow/orientation coupling,” *The Canadian Journal of Chemical Engineering*, vol. 80, no. 6, pp. 1093–1106, 2002.
- [55] D. J. Lee, M. W. Kim, S. Y. Kim, S. H. Lee, J. R. Youn, *et al.*, “Three dimensional flow simulation and structural analysis on stiffness of fiber reinforced anisotropic parts,” *Korea-Australia Rheology Journal*, vol. 22, no. 2, pp. 95–103, 2010.

- [56] H. M. Huynh, “Improved fiber orientation predictions for injection-molded composites,” Master’s thesis, University of Illinois at Urbana-Champaign, 2001.
- [57] M. Sepehr, G. Ausias, and P. J. Carreau, “Rheological properties of short fiber filled polypropylene in transient shear flow,” *Journal of Non-Newtonian Fluid Mechanics*, vol. 123, no. 1, pp. 19–32, 2004.
- [58] M. Sepehr, P. J. Carreau, M. Moan, and G. Ausias, “Rheological properties of short fiber model suspensions,” *Journal of Rheology*, vol. 48, no. 5, pp. 1023–1048, 2004.
- [59] M. Sepehr, P. J. Carreau, M. Grmela, G. Ausias, and P. Lafleur, “Comparison of rheological properties of fiber suspensions with model predictions,” *Journal of polymer engineering*, vol. 24, no. 6, pp. 579–610, 2004.
- [60] B. N. Nguyen, S. K. Bapanapalli, J. D. Holbery, M. T. Smith, V. Kunc, B. J. Frame, J. H. Phelps, and C. L. Tucker III, “Fiber length and orientation in long-fiber injection-molded thermoplasticspart i: Modeling of microstructure and elastic properties,” *Journal of composite materials*, vol. 42, no. 10, pp. 1003–1029, 2008.
- [61] J. Wang, J. F. O’Gara, and C. L. Tucker III, “An objective model for slow orientation kinetics in concentrated fiber suspensions: Theory and rheological evidence,” *Journal of Rheology*, vol. 52, no. 5, pp. 1179–1200, 2008.
- [62] J. H. Phelps and C. L. Tucker III, “An anisotropic rotary diffusion model for fiber orientation in short-and long-fiber thermoplastics,” *Journal of Non-Newtonian Fluid Mechanics*, vol. 156, no. 3, pp. 165–176, 2009.
- [63] A. Arlov, O. Forgacs, and S. Mason, “Particle motions in sheared suspensions iv. general behaviour of wood pulp fibres,” *Svensk Papperstidn*, vol. 61, no. 3, pp. 61–67, 1958.
- [64] E. Hinch, “The distortion of a flexible inextensible thread in a shearing flow,” *Journal of Fluid Mechanics*, vol. 74, no. 02, pp. 317–333, 1976.

- [65] S. Yamamoto and T. Matsuoka, "A method for dynamic simulation of rigid and flexible fibers in a flow field," *The Journal of chemical physics*, vol. 98, no. 1, pp. 644–650, 1993.
- [66] C. Joung, N. Phan-Thien, and X. Fan, "Direct simulation of flexible fibers," *Journal of non-newtonian fluid mechanics*, vol. 99, no. 1, pp. 1–36, 2001.
- [67] P. Skjetne, R. F. Ross, and D. J. Klingenberg, "Simulation of single fiber dynamics," *The Journal of chemical physics*, vol. 107, no. 6, pp. 2108–2121, 1997.
- [68] R. F. Ross and D. J. Klingenberg, "Dynamic simulation of flexible fibers composed of linked rigid bodies," *The Journal of chemical physics*, vol. 106, no. 7, pp. 2949–2960, 1997.
- [69] S. Kim and S. J. Karrila, *Microhydrodynamics: principles and selected applications*. Courier Corporation, 2013.
- [70] U. Strautins and A. Latz, "Flow-driven orientation dynamics of semiflexible fiber systems," *Rheologica Acta*, vol. 46, no. 8, pp. 1057–1064, 2007.
- [71] K. Ortman, D. Baird, P. Wapperom, and A. Whittington, "Using startup of steady shear flow in a sliding plate rheometer to determine material parameters for the purpose of predicting long fiber orientation," *Journal of Rheology*, vol. 56, no. 4, pp. 955–981, 2012.
- [72] R. S. J. Manley and S. Mason, "Particle motions in sheared suspensions. ii. collisions of uniform spheres," *Journal of colloid science*, vol. 7, no. 4, pp. 354–369, 1952.
- [73] R. S. J. Manley and S. Mason, "Particle motions in sheared suspensions iii.: Further observations on collisions of spheres," *Canadian Journal of Chemistry*, vol. 33, no. 5, pp. 763–773, 1955.
- [74] S. Yamamoto and T. Matsuoka, "Dynamic simulation of microstructure and rheology of fiber suspensions," *Polymer Engineering & Science*, vol. 36, no. 19, pp. 2396–2403, 1996.

- [75] A. J. Ladd, "Sedimentation of homogeneous suspensions of non-brownian spheres," *Physics of Fluids*, vol. 9, no. 3, pp. 491–499, 1997.
- [76] W. Russel, E. Hinch, L. Leal, and G. Tieffenbruck, "Rods falling near a vertical wall," *Journal of Fluid Mechanics*, vol. 83, no. 02, pp. 273–287, 1977.
- [77] R. Sundararajakumar and D. L. Koch, "Structure and properties of sheared fiber suspensions with mechanical contacts," *Journal of Non-Newtonian Fluid Mechanics*, vol. 73, no. 3, pp. 205–239, 1997.
- [78] O. G. Harlen, R. Sundararajakumar, and D. L. Koch, "Numerical simulations of a sphere settling through a suspension of neutrally buoyant fibres," *Journal of Fluid Mechanics*, vol. 388, pp. 355–388, 1999.
- [79] C. F. Schmid, L. H. Switzer, and D. J. Klingenberg, "Simulations of fiber flocculation: Effects of fiber properties and interfiber friction," *Journal of Rheology*, vol. 44, no. 4, pp. 781–809, 2000.
- [80] W. il Lee and G. S. Springer, "The motion of slender particles in shear flow," *Journal of Reinforced Plastics and Composites*, vol. 1, no. 4, pp. 279–296, 1982.
- [81] M. Berins, *Plastics engineering handbook of the society of the plastics industry*. Springer Science & Business Media, 1991.
- [82] C. Macosko and R. Larson, "Rheology: Principles, measurements, and applications," *VCH, New York*, 1994.
- [83] E. Mitsoulis, "Flows of viscoplastic materials: models and computations," *Rheology reviews*, vol. 135178, 2007.
- [84] G. L. Hand, "A theory of anisotropic fluids," *Journal of Fluid Mechanics*, vol. 13, no. 01, pp. 33–46, 1962.
- [85] N. Phan-Thien and A. Graham, "A new constitutive model for fibre suspensions: flow past a sphere," *Rheologica acta*, vol. 30, no. 1, pp. 44–57, 1991.
- [86] R. J. Crowson, A. J. Scott, and D. W. Saunders, "Rheology of short glass fiber-reinforced thermoplastics and its application to injection molding. iii. use

- of a high shear rate capillary rheometer in the injection molding shear rate range,” *Polymer Engineering & Science*, vol. 21, no. 12, pp. 748–754, 1981.
- [87] G. Ausias, J.-F. Agassant, M. Vincent, P. Lafleur, P.-A. Lavoie, and P. Carreau, “Rheology of short glass fiber reinforced polypropylene,” *Journal of Rheology*, vol. 36, no. 4, pp. 525–542, 1992.
- [88] S. Chatraei, C. Macosko, and H. Winter, “Lubricated squeezing flow: a new biaxial extensional rheometer,” *Journal of Rheology*, vol. 25, no. 4, pp. 433–443, 1981.
- [89] D. Kalyon, H. Tang, and B. Karuv, “Squeeze flow rheometry for rheological characterization of energetic formulations,” *Journal of Energetic Materials*, vol. 24, no. 3, pp. 195–212, 2006.
- [90] G. Dienes and H. Klemm, “Theory and application of the parallel plate plastometer,” *Journal of Applied Physics*, vol. 17, no. 6, pp. 458–471, 1946.
- [91] T. A. Osswald and C. L. Tucker III, “A boundary element simulation of compression mold filling,” *Polymer Engineering & Science*, vol. 28, no. 7, pp. 413–420, 1988.
- [92] R. Silva-Nieto, B. Fisher, and A. Birley, “Predicting mold flow for unsaturated polyester resin sheet molding compounds,” *Polymer composites*, vol. 1, no. 1, pp. 14–23, 1980.
- [93] M. Barone and D. Caulk, “A model for the flow of a chopped fiber reinforced polymer compound in compression molding,” *Journal of applied mechanics*, vol. 53, no. 2, pp. 361–371, 1986.
- [94] H. Mavridis, G. Bruce, G. Vancso, G. Weatherly, and J. Vlachopoulos, “Deformation patterns in the compression of polypropylene disks: experiments and simulation,” *Journal of Rheology*, vol. 36, no. 1, pp. 27–43, 1992.
- [95] A. Lawal and D. M. Kalyon, “Squeezing flow of viscoplastic fluids subject to wall slip,” *Polymer Engineering & Science*, vol. 38, no. 11, pp. 1793–1804, 1998.

- [96] M. Adams, B. Edmondson, D. Caughey, and R. Yahya, “An experimental and theoretical study of the squeeze-film deformation and flow of elastoplastic fluids,” *Journal of Non-Newtonian Fluid Mechanics*, vol. 51, no. 1, pp. 61–78, 1994.
- [97] W. Zhang, N. Silvi, and J. Vlachopoulos, “Modelling and experiments of squeezing flow of polymer melts,” *International Polymer Processing*, vol. 10, no. 2, pp. 155–164, 1995.
- [98] C. Hieber and S. Shen, “A finite-element/finite-difference simulation of the injection-molding filling process,” *Journal of Non-Newtonian Fluid Mechanics*, vol. 7, no. 1, pp. 1–32, 1980.
- [99] C.-C. Lee, F. Folgar, and C. Tucker III, “Simulation of compression molding for fiber-reinforced thermosetting polymers,” *Journal of engineering for industry*, vol. 106, no. 2, pp. 114–125, 1984.
- [100] U. Yilmazer and D. M. Kalyon, “Slip effects in capillary and parallel disk torsional flows of highly filled suspensions,” *Journal of Rheology*, vol. 33, no. 8, pp. 1197–1212, 1989.
- [101] J. Thorpe and W. Shaw, “Developments in theoretical and applied mechanics,” 1967.
- [102] P. Gupta and A. Gupta, “Squeezing flow between parallel plates,” *Wear*, vol. 45, no. 2, pp. 177–185, 1977.
- [103] P. S. Hubbard, “Rotational brownian motion,” *Physical Review A*, vol. 6, no. 6, p. 2421, 1972.
- [104] S. Shrestha, S. Tiwari, A. Klar, and S. Hardt, “Numerical simulation of a moving rigid body in a rarefied gas,” *Journal of Computational Physics*, vol. 292, pp. 239–252, 2015.
- [105] P. R. Lang and Y. Liu, “Soft matter at aqueous interfaces,” 2015.

- [106] O. R. Walton and R. L. Braun, “Viscosity, granular-temperature, and stress calculations for shearing assemblies of inelastic, frictional disks,” *Journal of Rheology*, vol. 30, no. 5, pp. 949–980, 1986.
- [107] G. Wang, W. Yu, and C. Zhou, “Optimization of the rod chain model to simulate the motions of a long flexible fiber in simple shear flows,” *European Journal of Mechanics-B/Fluids*, vol. 25, no. 3, pp. 337–347, 2006.
- [108] L. H. Switzer, *Simulating systems of flexible fibers*. University of Wisconsin–Madison, 2002.
- [109] F. Folgar and C. L. Tucker III, “Orientation behavior of fibers in concentrated suspensions,” *Journal of Reinforced Plastics and Composites*, vol. 3, no. 2, pp. 98–119, 1984.
- [110] J. S. Cintra Jr and C. L. Tucker III, “Orthotropic closure approximations for flow-induced fiber orientation,” *Journal of Rheology*, vol. 39, no. 6, pp. 1095–1122, 1995.
- [111] G. Meirson and A. N. Hrymak, “Two-dimensional long-flexible fiber simulation in simple shear flow,” *Polymer Composites*, 2015.
- [112] J. H. Phelps, A. I. A. El-Rahman, V. Kunc, and C. L. Tucker III, “A model for fiber length attrition in injection-molded long-fiber composites,” *Composites Part A: Applied Science and Manufacturing*, vol. 51, pp. 11–21, 2013.
- [113] C. F. Lee, “Thermal breakage of a semiflexible polymer: breakage profile and rate,” *Journal of Physics: Condensed Matter*, vol. 27, no. 27, p. 275101, 2015.
- [114] H. Hsiao and I. Daniel, “Elastic properties of composites with fiber waviness,” *Composites Part A: Applied Science and Manufacturing*, vol. 27, no. 10, pp. 931–941, 1996.
- [115] A. Ali, D. de’Ath, D. Gibson, J. Parkin, Z. Alam, G. Ward, and D. I. Wilson, “Development of a ‘millimanipulation’ device to study the removal of soft solid fouling layers from solid substrates and its application to cooked lard deposits,” *Food and Bioproducts Processing*, vol. 93, pp. 256–268, 2015.

- [116] J. C. Duarte, W. P. Schellart, and A. R. Cruden, “Rheology of petrolatum–paraffin oil mixtures: Applications to analogue modelling of geological processes,” *Journal of Structural Geology*, vol. 63, pp. 1–11, 2014.
- [117] R. B. Bird, R. Armstrong, and O. Hassager, *Dynamics of polymeric liquids. Vol. 1: Fluid mechanics*. John Wiley and Sons Inc., New York, NY, 1987.
- [118] S. Haward, A. Jaishankar, M. Oliveira, M. Alves, and G. McKinley, “Extensional flow of hyaluronic acid solutions in an optimized microfluidic cross-slot devicea),” *Biomicrofluidics*, vol. 7, no. 4, p. 044108, 2013.

Appendix A

Squeeze Flow Fiber Orientation

Experimental

Several experiments were conducted in order to validate the model. Petroleum jelly was chosen as a matrix for the experiments due to it being highly viscous and relatively transparent. Petroleum jelly (Vaseline trademark) rheology was tested using TA instruments AR2000ex rheometer. The test showed a power law behaviour. Similar results could be found in the literature [115,116]. The experiment was conducted under the following conditions: 25mm plates with 0.5mm gap at 22°C. Results in log-log plot are presented in Figure A.1. Eq. (A.1) represents power law viscosity material:

$$\mu = K\dot{\gamma}^{n-1} \quad (\text{A.1})$$

Figure A.1 shows that equation from type of eq. (A.1) could fit the data very well with power law parameters obtained: $K = 81Pa \cdot s^{0.77}$, $n = 0.23$.

Although the petroleum jelly rheology obtained in this research in general is similar to results obtained in the literature it differs slightly. In [115] sanded plates are used to measure petroleum jelly viscosity and the constants they found were: $K = 190Pa \cdot s^{0.78}$, $n = 0.22$

Polyester sewing thread of approximately 0.2mm thickness was chosen as a fiber.

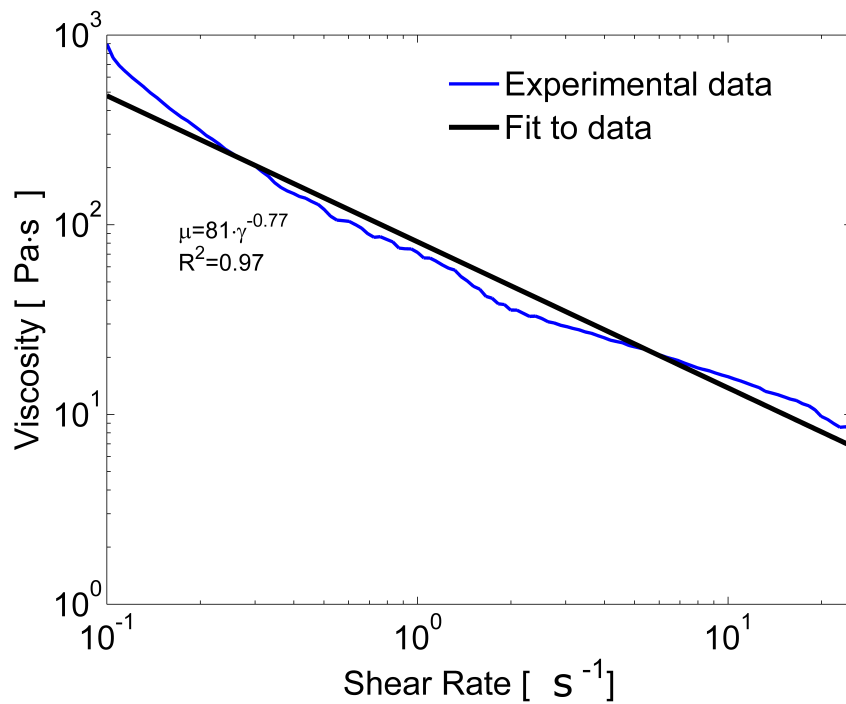


Figure A.1: Rheology results of petroleum jelly at 22°C.

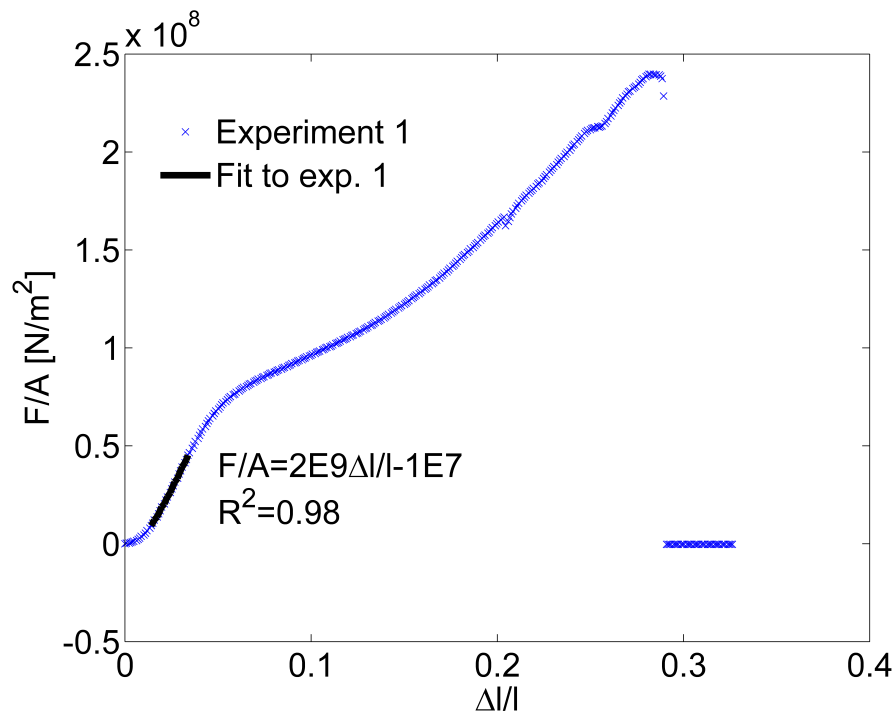


Figure A.2: Fiber Young's modulus measurement.

Young's modulus was measured using MARK-10 ESH301L motorized test stand with MARK-10 series force gauge model MS-10 (5kg capacity) as a load cell. The tests were conducted under the extension rate of 10mm/min. The results of these experiments could be observed in Figure A.2. As it could be seen from Figure A.2 the thread was pulled until it was torn at approximately 0.3 relative elongation. A linear fit was then made to the elastic deformation region and Young's modulus was extracted from the slope, which was found to be $2 \cdot 10^9 Pa$ which corresponds to data found online.

Mold for sample formation was a two end open cylinder with 9cm diameter and 3cm height which was made from poly(methyl methacrylate). The bottom part of the mold was closed with a petri dish large enough to block one of the exits from the cylinder mold. Half of the mold was then filled with petroleum jelly all the way up. A 1.6cm fiber was then placed in a vertical position on the diameter line 2cm away from the center. The fiber was placed as symmetrically as possible toward the horizontal line. Once the fiber was in place the other half of the mold was also closed with petroleum jelly, a petri dish just small enough to pass through the mold (in fact dishes from the same set with one a bit smaller than the other where used for the top and the bottom of the mold) was used to push the petroleum jelly pack out of the mold. Thus we received open edges petroleum jelly puck with a vertical polyester fiber inside placed between two rigid petri dishes. This puck was then pressed at a constant speed of 3mm/s (analogical for two walls moving toward each other at 1.5mm/s). These experiments were conducted using MTS press with MTS 25 ton load cell which was controlled by MTS 458.20 MictoConsole. The results of such experiments are shown in Figure A.3.

Experiments conducted with petroleum jelly confirmed that the flow in cylindrical coordinates in radial direction could be approximated to a two dimensional flow. In all the results the entire fiber could always be found on the rz plane. In addition it could be seen that the resulting shape resembles previously obtained simulation results for fibers that were initially placed at the horizontal center of the system.



Figure A.3: Visualization experiment, resulting fiber shape at 3.3s.

Radial power law squeeze flow solution was obtained from the literature [117, 118] and it is presented in eqs. (A.2)-A.3 this solution is for the quarter system presented in Figure 1 although the horizontal center of the system in this case is at $r = 0$.

$$V_r = \frac{r}{a} \left(\frac{2n+1}{2n+2} \left(1 - \left(\frac{z}{a} \right)^{1+1/n} \right) \right) (-V_w) \quad (\text{A.2})$$

$$V_z = \frac{2n+1}{n+1} \left(\frac{n}{2n+1} \right) \left(\left(\frac{z}{a} \right)^{2+1/n} - \frac{z}{a} \right) (-V_w) \quad (\text{A.3})$$

In order to solve the model for the power law case several modifications had to be made. From Chapter 3.1 it is known that the rotational friction coefficients depend linearly on viscosity hence the values in Table 3.1 were divided by $1000 Pa \cdot s$ (the viscosity at which they were obtained) and multiplied by the power law viscosity expression, shear rate for which is calculated at the center of each rigid segment using eq. 4.2. Linear friction coefficient as well as the calculation of torque were also modified. A simulation of long flexible fiber in a power law fluid was conducted. A system with gap of 3 cm (distance between two walls) was defined and the fiber made out of 16 segments of 1 mm each was placed in the horizontal mid-line at a distance

of 2 cm from the center along the x axis. The velocity of the plates was set as 1.5 mm/s. Young's modulus of the fiber was set as $2 \cdot 10^9 \text{ Pa} \cdot \text{s}$. The simulation was run twice, first for the viscosity parameters measured by the authors and second for the viscosity found in the literature [115]. The resulting snapshots of fiber shapes at 0, 3.3, 4, 5 s.

By comparing simulation results from Figures A.4 and A.5 to experimental results from Figure A.3 it could be seen that qualitatively the results match well. Quantitatively the experimental results match better to simulation results obtained with the viscosity from the literature. As was previously mentioned it was extremely difficult to place the fiber exactly in the mid-line and exactly straight at $\pi/2$ position. In addition it could be seen that at 4s of simulation time the fiber is already much more bent while the difference in compression between the two is only 2mm. Such a high precision is very hard to control during the experiment, which could be an additional reason for the mismatch. The linear movement in simulation and experimental results was approximately the same which resulted in fiber moving approximately 0.5cm in the 3.3s of the experiment. It could also be seen from simulation results



Figure A.4: Long flexible fiber simulation in power law fluid, experimental viscosity.



Figure A.5: Long flexible fiber simulation in power law fluid, literature viscosity.

that the simulation is highly dependent on the viscosity.

Eqs. (A.2)-(A.3) are obtained using Hele-Shaw assumptions which essentially make it a Hele-Shaw type solver. It could be seen that the results in Figure A.4 and A.5 resemble results from Figure 4.19A, further increase in viscosity will lead to results similar to Figure 4.19B.

Curriculum Vitae

Name: Gleb Meirson

Post-Secondary Education and Degrees: Technion
Haifa, Israel
2003-2010 (M.Sc. and B.Sc.)

University of Western Ontario
London, ON
2012 - 2016 Ph.D.

Honours and Awards: Trillium scholarship (OTS)
University of Western Ontario, 2012-2015

Related Work Experience: Teaching Assistant
The University of Western Ontario
2012 - 2016

Oplon Pure Science
Chemical Engineer
2010 - 2011

LUDAN group
Process Engineer
2010 - 2010

Publications:

G. Meirson, A.N. Hrymak, Two Dimensional Long-Flexible Fiber Simulation in Simple Shear Flow, Polymer Composites, **accepted**(2015)

G. Meirson, A.N. Hrymak, Two Dimensional Long-Flexible Fiber Simulation in Squeeze Flow, Polymer Composites, **submitted**(2015)